Synthesis and in situ Characterization of Nanostructured and Amorphous Metallic Films

by

Rohit Sarkar

A Dissertation Presented in Partial Fulfillment
of the Requirements for the Degree
Doctor of Philosophy

Approved April 2017 by the
Graduate Supervisory Committee:

Jagannathan Rajagopalan, Chair
Karl Sieradzki
Pedro Peralta
Peter Crozier

ARIZONA STATE UNIVERSITY

May 2017

ABSTRACT

Nanocrystalline (nc) thin films exhibit a wide range of enhanced mechanical properties compared to their coarse-grained counterparts. Furthermore, the mechanical behavior and microstructure of nc films is intimately related. Thus, precise control of the size, aspect ratio and spatial distribution of grains can enable the synthesis of thin films with exceptional mechanical properties. However, conventional bottom-up techniques for synthesizing thin films are incapable of achieving the microstructural control required to explicitly tune their properties. This dissertation focuses on developing a novel technique to synthesize metallic alloy thin films with precisely controlled microstructures and subsequently characterizing their mechanical properties using in situ transmission electron microscopy (TEM). Control over the grain size and distribution was achieved by controlling the recrystallization process of amorphous films by the use of thin crystalline seed layers. The novel technique was used to manipulate the microstructure of structural (TiAl) and functional (NiTi) thin films thereby exhibiting its capability and versatility. Following the synthesis of thin films with tailored microstructures, in situ TEM techniques were employed to probe their mechanical properties. Firstly, a novel technique was developed to measure local atomic level elastic strains in metallic glass thin films during in situ TEM straining. This technique was used to detect structural changes and anelastic deformation in metallic glass thin films. Finally, as the electron beam (e-beam) in TEMs is known to cause radiation damage to specimen, systematic experiments were carried out to quantify the effect of the e-beam on the stress-strain response of nc metals. Experiments conducted on Al and Au films revealed that the e-beam enhances dislocation activity leading to stress relaxation.

ACKNOWLEDGMENTS

In the words of the great Isaac Newton, “If I have seen further, it is by standing on the shoulders of giants”. The giants in my life are all the people that have empowered me to reach this stage in my career. Firstly, I would like acknowledge the sacrifice that my family members have had to make over the years to ensure that I succeed in all my endeavors. I am forever indebted to my adviser Dr. Jagannathan Rajagopalan who took me under his wing and guided me in every step of the way in my research. I would also like to thank my committee members Dr. Pedro Peralta, Dr. Karl Sieradzki and Dr. Peter Crozier for taking their time to evaluate my work and for their invaluable inputs towards my dissertation. I am also grateful to Dr. Christian Rentenberger at the University of Vienna for taking the time to teach me the nuances of in situ experimentation. I would also like to thank my all my collaborators, especially Christian Ebner and Dr. Sudhanshu Shekhar Singh for their contributions to my thesis and the new dimensions that they added to my work. I would like to thank my lab mates Ehsan, Tim, Cole, Andrea, Abhinav, Suhas, Rohit Berlia and Paul for all the support and help that I received from them over the years. I am also very grateful to Dr. Carl Mayer for his expert advice and help throughout my research work. I would like to gratefully acknowledge the use of central research facilities at the Arizona State University, specifically, the LeRoy Erying Center for Solid State Science and the Center for Solid State Electronics Research. My research would not have been possible without the support of National Science Foundation research grants that our lab received and I am indebted to the funding agency for the financial support. Lastly, I would like to thank all my friends who have made this journey pleasant and enriched my life through their company and support.

TABLE OF CONTENTS

Page

CHAPTER Page

LIST OF TABLES

Table Page

LIST OF FIGURES

Figure Page

Figure Page

CHAPTER 1

INTRODUCTION

The motivation behind this thesis is the synthesis of nanocrystalline (nc) alloys with precisely tailored microstructures and the subsequent analysis of their mechanical behavior using in situ transmission electron microscopy (TEM) techniques. Nanocrystalline metals and alloys (Figure 1) have a mean grain size of less than 100 nm and are characterized by a larger volume fraction of grain boundaries compared to coarse-grained materials. As a result, nc materials exhibit a wide range of enhanced mechanical and tribological properties and have been actively explored for potential structural applications. In addition, at these small grain sizes, the mechanical properties of materials are extremely sensitive to the geometry, size and spatial distribution of grains. Furthermore, it has been shown that nc metals having a specific distribution of grain sizes can exhibit unique properties like recovery of inelastic strain. Thus, the ability to tailor the microstructure of nc alloys would allow us to meticulously engineer the mechanical behavior of these materials.

In this thesis, a novel technique has been used to tailor the microstructures of sputter-deposited TiAl and TiNi thin films. This was accomplished by using intermediate crystalline seed layers that alter the crystallization kinetics of these materials that are amorphous in the as-deposited state. The seeds were found to aid crystallization, with seeded films crystallizing faster than non-seeded films for the same annealing temperature. Furthermore, the final microstructure of the seeded films was in the

nanocrystalline regime up to a temperature of 750^{o}C, whereas the unseeded films underwent rapid recrystallization to form large microcrystalline grains. Moreover, cross-sectional TEM analysis revealed that the grain height scaled with the seed spacing along the thickness of the film. Thus, this technique enabled control of the grain diameter, height and spatial distribution. The technique was used to synthesize intermetallic films with gradient structures that could potentially have a unique combination of enhanced strength and ductility. Additionally, the seed element was also found to influence the phase composition in NiTi thin films, with a Cr seed stabilizing austenitic nc grains.

Having synthesized nc thin films with tailored microstructures, studying their mechanical behavior in situ was critical to understanding the deformation mechanisms that dictate their mechanical behavior. With this in mind, in-situ TEM straining was used to study the mechanical behavior of NiTi thin films synthesized using the seed mediated crystallization technique. NiTi films were studied because they exhibit unique mechanical properties like shape memory behavior and pseudoelasticity. If stable nanocrystalline grains can be obtained in these materials, it could lead to the enhancement of strength and inelastic strain recovery. The TEM can be a vital tool to study the deformation mechanisms and microstructural evolution in such nc metals. The ability to track changes in the microstructure through high resolution imaging combined with the capability to measure crystal rotations and lattice strain using diffraction makes the TEM indispensable in the research of nc materials. In-situ experiments carried out in the TEM give us the unique capability to study the behavior of nc materials in real-time while applying a mechanical or thermal stimulus. In-situ TEM straining of the NiTi films

with tailored microstructures revealed an extremely high stress for martensite phase transformation in these materials. Plastic deformation in the austenite grains was also uncovered during the tests.

As the films with tailored microstructures were amorphous in the as deposited state, there was a need to study the atomic scale behavior of amorphous films as well. Metallic glasses, which are amorphous metal alloys, exhibit excellent tensile strength and corrosion resistance. However, these materials are brittle and fail by the localization of deformation in shear bands. Moreover, these materials are known to undergo atomic level rearrangements when subjected to loading. Thus, micro strain characterization at the atomic scale can give us valuable information about the behavior of nanoscale metallic glasses. Although techniques exist to measure lattice strains in crystalline materials using the TEM, the lattice strain in amorphous thins films have not been measured in situ. A novel technique was employed to measure micro strains in metallic glass thin films by tracking geometric changes in the selected area diffraction (SAD) patterns during in-situ straining. Using this method, structural rearrangements induced by straining and the presence of anelastic deformation were detected.

Finally, as in situ TEM straining was extensively used in this dissertation to study the mechanical behavior of nanoscale metals, it was important to uncover the artifacts that were induced in the experiments by the TEM electron beam (e-beam). While it is well known that the TEM electron beam can trigger changes in the mechanical behavior of the materials being probed, systematic investigations have not been performed to

determine the e-beam effect on the in-situ deformation response of nc materials. To address this issue, methodical experiments were performed to study the effect of the e-beam on the deformation response of nc Al and Au thin films. The experiments revealed that the e-beam enhances dislocation activity in these materials leading to a relaxation in stress. The e-beam was also found to cause anomalous necking along the width of the specimen. These effects of the e-beam were found to be more pronounced at lower accelerating voltages. Inelastic scattering processes that led to the depinning of dislocations pinned at grain boundaries was found to be the major driver behind these anamolous effects. The experiments suggested that using higher accelerating voltages while maintaining lower beam intensities could help minimize e-beam induced artifacts.

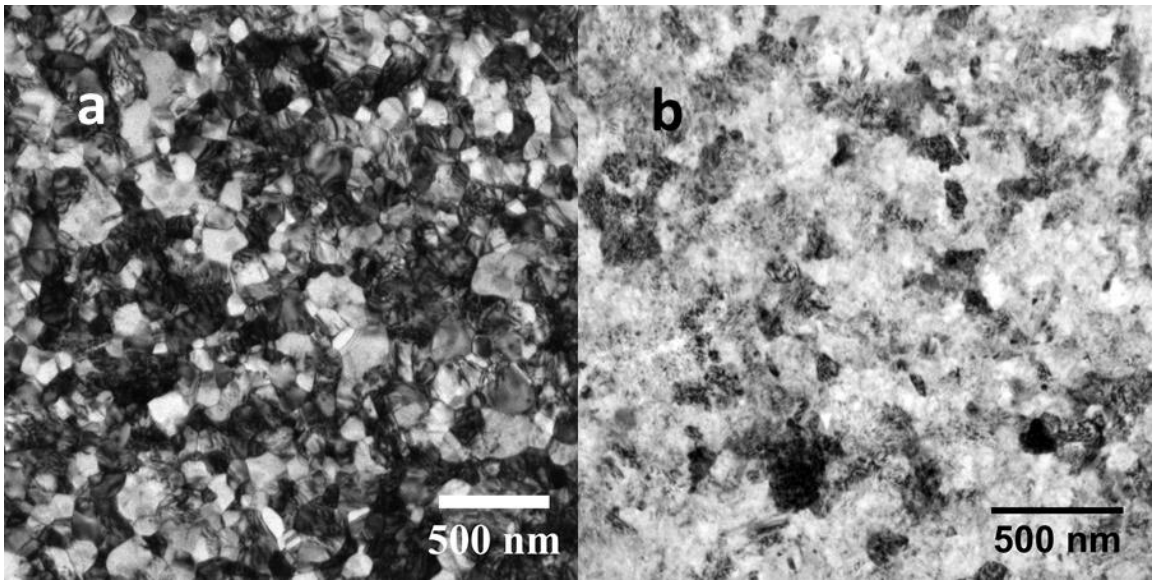

Figure 1: (a) TEM micrograph of nc Al thin film with a mean grain size of 125nm. (b) TEM micrograph of a $Ti_{45}Al_{55}$ intermetallic thin film deposited by DC magnetron sputtering.

CHAPTER 2
LITERATURE REVIEW

Nanocrystalline and amorphous thin films have been the subject of extensive research in recent years. Specifically, many studies have focused on the microstructural evolution and mechanical behavior of these materials. The following sections contain a review of the research most pertinent to this dissertation.

2.1 Nanocrystalline Materials

Nanocrystalline (nc) metals and alloys have a mean grain size less than 100 nm. This class of materials exhibits a wide range of enhanced mechanical properties including high yield strength and wear resistance (Kumar, Van Swygenhoven, and Suresh 2003). The small grain size of these materials leads to a high volume fraction of grain boundaries (Meyers, Mishra, and Benson 2006), which results in significant grain boundary strengthening via the Hall-Petch effect (Figure 2).

nc materials can be synthesized by top-down or bottom-up processes. Top down processes like cryomilling and compaction or severe plastic deformation can be used to synthesize bulk nanocrystalline materials (Valiev et al. 2006; C.C. Koch, 2003) . On the other hand, bottom up processes such as physical vapor deposition and electrodeposition enable the synthesis of nanoscale nc materials (C. J. Chen et al. 2009; Kumar et al. 2003).

The grain boundaries in these materials act as sources and sinks for dislocations and mediate deformation mechanisms like grain boundary sliding. Therefore, the character of these boundaries has been the subject of in-depth research. While grain boundaries in nc metals were previously considered to be fairly thick amorphous regions (Zhu et al. 1987), recent experiments using high resolution electron microscopy (Kumar et al. 2003) as well as molecular dynamics simulations (Van Swygenhoven, Farkas, and Caro 2000) have revealed that the crystalline order is only distorted over a distance of few atomic planes (typically less than 1 nm).

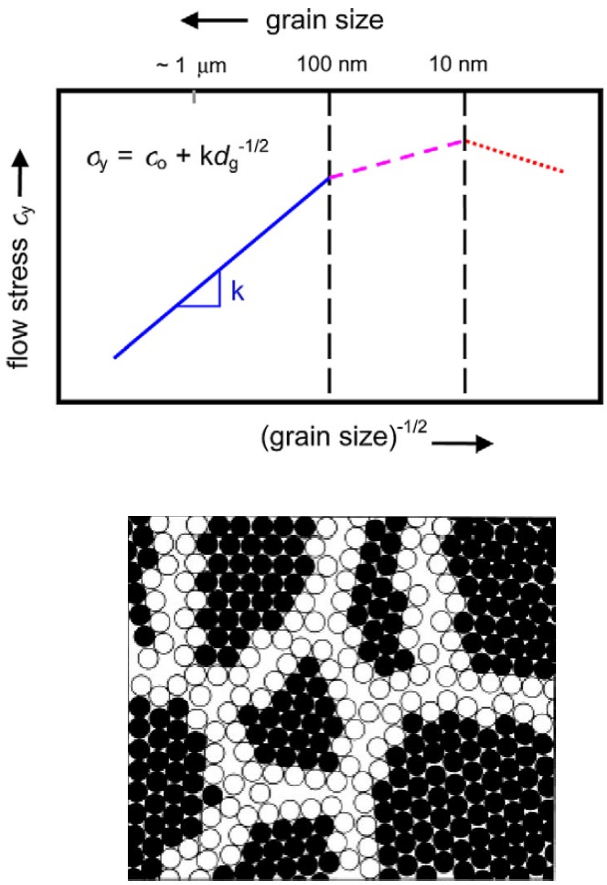

Figure 2. (Top) Increase in yield strength with decreasing grain size in nc materials (Kumar et al., 2003). (Bottom) Model representing the structure of nc materials. Large fraction of atoms in grain boundaries (white circles) can be seen in nc materials (Meyer et al, 2006).

Nc metals have been shown to exhibit substantially higher hardness and yield strength compared to coarse grained materials (Sanders, Eastman, and Weertman 1997). However, these materials exhibit poor ductility as they do not strain harden through dislocation pileups at grain boundaries. These materials also show a dearth of intrinsic dislocations, with the majority of dislocations being nucleated and absorbed at grain boundaries during straining (Kumar, Van Swygenhoven, and Suresh 2003). It has also been shown that below grain sizes of 10 nm these materials become relatively weaker as phenomena like grain boundary sliding and coble creep start to dominate (Masumura, Hazzledine, and Pande 1998). Additionally, these materials also show high strain rate sensitivity, with their tensile strength increasing with loading rate (Lu, Sui, and Lu 2000). This has been attributed to the presence of different stress states at the grain boundaries compared to the grain interior.

In addition to enhanced mechanical properties, nanocrystalline materials have been shown to exhibit certain unusual properties, which are intimately related to their structures. For instance, Rajagopalan et al. have shown that by having a large distribution of grain sizes in nanocrystalline metals, recovery of plastic strain can be achieved (Rajagopalan, Han, and Saif 2007). Therefore, it becomes clear that there is the need for the development of a technique that can enable the synthesis of nanocrystalline metals with tailored structures, which would enable the extraction of unique properties from nc metals. The synthesis-structure-property relationships in these materials also need further investigation.

2.2 Metallic Glasses

Metallic glasses are amorphous metallic alloys that lack long range order and microstructural defects such as grain boundaries and dislocations that are present in crystalline metals and alloys (Ashby and Greer 2006). These materials are known to have high yield strength, hardness and excellent corrosion resistance. Metallic glasses also show an extended elastic limit of up to 2% but have limited ductility and fail by the localization of plastic deformation in shear bands (Figure 3) (Pekarskaya, Kim, and Johnson 2001).

Bulk metallic glasses are produced by rapid cooling from a metallic liquid (Klement, Willens, and Duwez 1960) while nanoscale metallic glasses can be synthesized by sputter deposition (Masui et al. 1985). Bernal et al. envisioned the structure of metallic glasses to be that of a frozen metallic liquid with a purely geometric atomic arrangement (Bernal 1960). However, this model did not account for the short and medium range order that has is observed in metallic glasses. Recently, it has been suggested that metallic glasses can be modeled as consisting of effectively packed local structural units (Miracle 2004). These structural units however do not retain long range order due to internal strains and give rise to the amorphous structure beyond the nanoscale.

While undergoing deformation, metallic glasses are known to undergo local structural rearrangements through the formation of shear transformation zones (STZ) (Schuh, Hufnagel, and Ramamurty 2007). Furthermore, the formation of these STZs has been found to depend on the presence of free volume zones (Figure 4) in these materials (Argon and Shi 1982). Therefore, the free volume zones influence the mechanical behavior of these materials (Z. Wang et al. 2012). The free volume zones represent the less densely packed spaces among the atomic clusters, where atoms have a lower co-ordination number compared to more densely packed regions (Cohen, "Molecular Transport in Liquids and Glasses" 1959). The presence of free volume zones have also

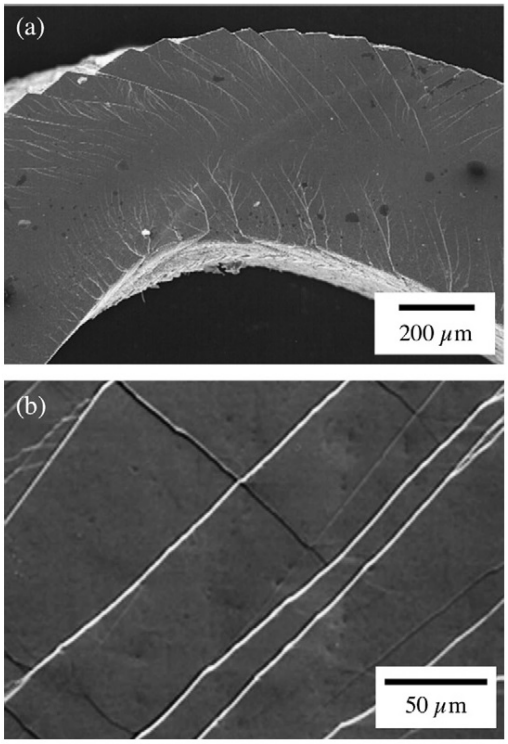

Figure 3. Images showing slip steps in a Zirconium based metallic glass that are associated with shear bands in metallic glasses. (Schuh et.al., 2007)

been linked to anelastic deformation (Caron et al. 2011) in metallic glasses that decrease their Young's modulus (E) by almost 30% compared to their crystalline counterparts.

Recently, a large volume of research has been focused on enhancing ductility in these materials by limiting their geometric size to the nanoscale (Jang and Greer 2010; Tian, Wang, and Shan 2016). Wang et al. reported that when the size of Al based metallic glass micropilllars was decreased from a few microns to 100 nm a size dependent strengthening behavior was observed (C. C. Wang et al. 2012). This size dependence of strength has been attributed to the balance between the strain energy buildup during yielding and the energy required to nucleate shear bands.

Additionally, the formation of shear bands is also suppressed in nanoscale metallic glass specimen. As a result, the deformation mechanisms operating in these materials are markedly different. Compression experiments on metallic glass nanopillars by Volkert et al. have shown that the post mortem microstructure consists of smooth mushroom like morphology instead of shear bands (Volkert, Donohue, and Spaepen 2008).

Thus, it is evidently clear that the deformation mechanisms operating at the nanoscale in metallic glasses need to be studied further. It also suggests that we need a new technique that can enable us to simultaneously image these materials at the nanoscale and obtain atomic scale strain information during deformation.

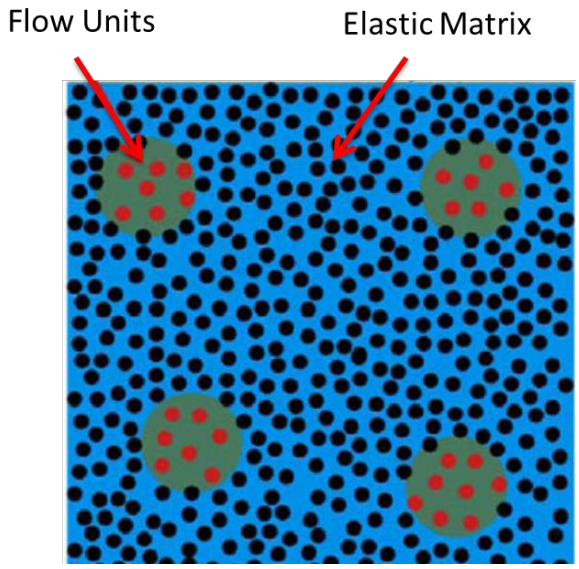

Figure 4: Atomic scale structure of metallic glasses showing anelastic flow units embedded in an elastic matrix. Reprinted from Wang et al. (2012).

2.3 Microstructural Engineering of NC materials

Comprehensive control over the microstructure would enable the design of material systems with specific mechanical, tribological and electrical properties. Techniques to synthesize nc materials can be broadly divided into “top down” or “bottom up” processes. Top down processes like cryo-milling involve attrition of larger sized particles to yield nanostructured materials while bottom up process comprise of building up nanostructures by the agglomeration of individual or clusters of atoms. Although both these approaches are extensively used, current methods that use either of these approaches have some inherent disadvantages. Top down methods like severe plastic deformation (SPD) yield highly heterogeneous microstructures which lead to variations in mechanical properties (Valiev et al. 2006) while bottom up processes like electrodeposition also offer limited control over the final microstructure (Xu et al. 2005).

Hence, here an alternate method to synthesize nc alloy films with tailored microstructures is developed that would address these issues.

While some techniques provide the ability to control the grain size in vapor deposited thin films, they usually depend on the thickness of the film deposited (Girault et al. 2013), the rate of deposition (Vopsaroiu et al. 2004) or annealing during or post deposition (Drera et al. 2015). In such techniques, either the grain size and thickness cannot be decoupled or the control over the grain aspect ratio cannot be easily achieved. Thus, there is a need to develop a process that would allow us to have a high degree of control of the final microstructure in thin films.

The process of grain growth in thin films formed from a vapor phase consists of the steps of nucleation, island formation, coalescence and grain coarsening (Petrov et al. 2003). Controlling and manipulating any of these steps could enable us to tailor the grain structure in these films. For example nano-diamond particles have been used to alter the nucleation kinetics in nanocrystalline diamond films formed by CVD, thereby achieving control over the microstructure (Buijnsters et al. 2013) (Figure 5). Palladium seed layers have been shown to enhance the epitaxial growth of sputter deposited Cu and Co films (Harp and Parkin 1994). Kwok et al. have used thin seed layers of PbTiO3 to aid the nucleation of lead zirconate titanate and alter its grain structure (Kwok and Desu 1993). Bias pretreatment has also been shown by Stoner et al. to modify the nucleation density of diamond deposited on silicon substrates by CVD (Stoner et al. 1992). Control over shape of PdSe nanocrystals has been achieved by altering the concentration of noble

metal nanoparticle seeds (Yong et al. 2006) . Dislocation bands remnant from severe rolling have also been used as heterogeneous nucleation sites to achieve grain refinement in Al–Mg–Si–Cu alloys during recrystallization (Troeger and Starke Jr 2000). Miller et al. show that isolated grains can act as seeds for the growth of highly oriented polycrystalline ZnO2 films (Miller and Lange 1991). Although such process do successfully alter the nucleation and growth mechanisms of nanocrystalline materials, there still remains the lack of a process that can comprehensively control the grain size, aspect ratio and spatial distribution of grains in polycrystalline thin films.

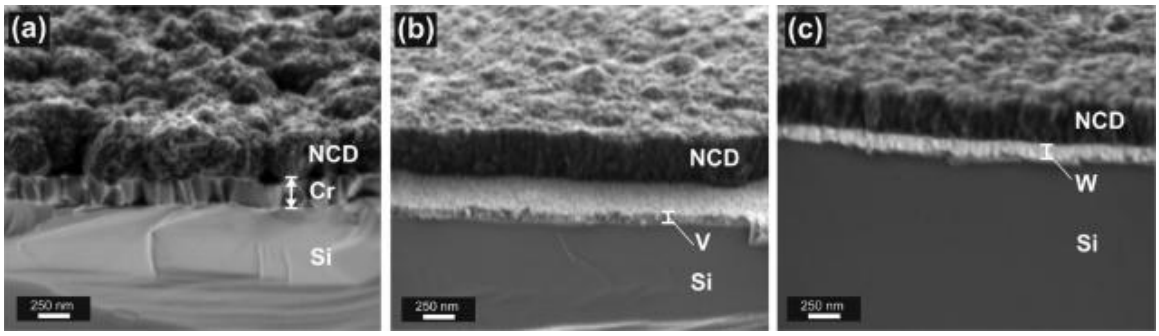

Figure 5: SEM images showing the difference in surface morphology of diamond films grown on Si having different intermediate seed layers. Reprinted from (Buijnsters et al. 2013).

2.4 Micro Strain Measurements in Metallic Glasses

Several techniques have been recently developed to measure the lattice strain of crystalline materials using the TEM (Béché et al. 2013; Mahr et al. 2015) (Figure 6). The methods employ either (i) high resolution TEM (Hüe et al. 2008) and dark field electron holography (Béché et al. 2011) or (ii) nano beam electron diffraction (Usuda et al. 2005) and convergent beam electron diffraction (Clément et al. 2004). However, the TEM has not been employed to measure micro strain in metallic glasses.

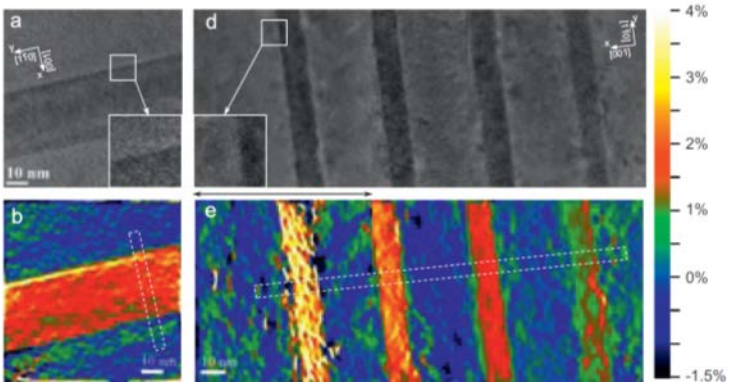

Figure 6: Images showing strain map obtained in SiGe multilayers using Graphical Phase Analysis (GPA) of HRTEM image. Reprinted from(Béché et al. 2013b).

The micro strain in metallic glasses has only been evaluated by techniques that use high energy x-ray and neutron diffraction (Poulsen et al. 2005; X. D. Wang et al. 2007; Mattern et al. 2009; T. C. Hufnagel, Ott, and Almer 2006). These techniques involve calculating the micro strain tensors by measuring the relative shift of diffraction peaks in reciprocal space during straining (Fig. 7). Such studies have helped shed new light into the behavior of metallic glasses. For example, it has been revealed that micro strains in metallic glasses are dependent on length scales. This implies that nearest neighbor shells are stiffer than distant atomic shells, which is contrary to the conventional understanding that the bonds in metallic glasses are isotropic in nature. Vempati et.al (Vempati et al. 2012) have postulated that this length scale dependence of strain in metallic glasses is due to heterogeneous non-affine atomic displacements. Ma et al. (Ma et al. 2012) have used in-situ neutron diffraction to show that the Young's and shear modulus of various metallic glasses are similar to their base metal component. High energy x-ray scattering has also been employed to study the strain around crack-tips in metallic glasses (Todd C. Hufnagel, Vempati, and Almer 2013) and the mechanism of

nucleation and propagation of shear bands during loading (Y. Huang et al. 2014). Plastic deformation in metallic glasses has also been studied and Scudion et al. have found that shear strain and structural anisotropy play a major role in the plastic behavior of metallic glasses (Scudino et al. 2015). While these studies have revealed several important insights into the deformation behavior of metallic glasses, the use of x-ray or neutron diffraction has restricted them to bulk, macro scale samples because of their relatively large beam sizes. Therefore, deformation behavior of metallic glasses at the nanoscale has remained largely unexplored.

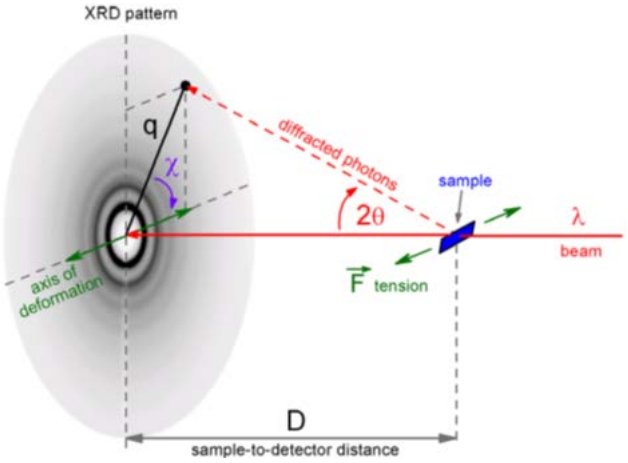

Figure 7: Experimental setup for micro strain evaluation in metallic glasses using XRD. The shift of diffraction peaks on straining is used to extract the micro strain. Reprinted from Mattern et.al., 2009.

2.5 E-Beam Effects on the Mechanical Behavior of Nanostructured Materials

It is well established that the TEM e-beam can cause radiation damage to the specimen being probed. Radiolysis, knock-on damage, and specimen heating are known to be the most common damage mechanisms (Williams and Carter 2009a). Crozier et al. have shown that the e-beam can cause sputtering damage on the exit surface of rutile

crystals (Crozier, McCartney, and Smith 1990). Intense nanometer sized beams have also been found to drill holes in thin specimens and cause accumulation of contaminants (Raymond F. Egerton, Wang, and Crozier 2006). Egerton et al have also had detailed discussions on the aspects of beam heating and shown that the increase in temperature caused by the e-beam is independent of specimen thickness (R. F. Egerton, Li, and Malac 2004). Apart from these conventional damage mechanisms, the e-beam has also been shown to alter the deformation mechanisms in nanomaterials. The e-beam can activate dislocations, and defects generated by e-beam exposure can lead to additional deformation processes. For example, low to moderate intensity e-beam has been used to induce superplastic deformation in nanoscale silica particles and nanowires that are usually brittle at low temperatures (Figure 8) (Zheng et al. 2010).

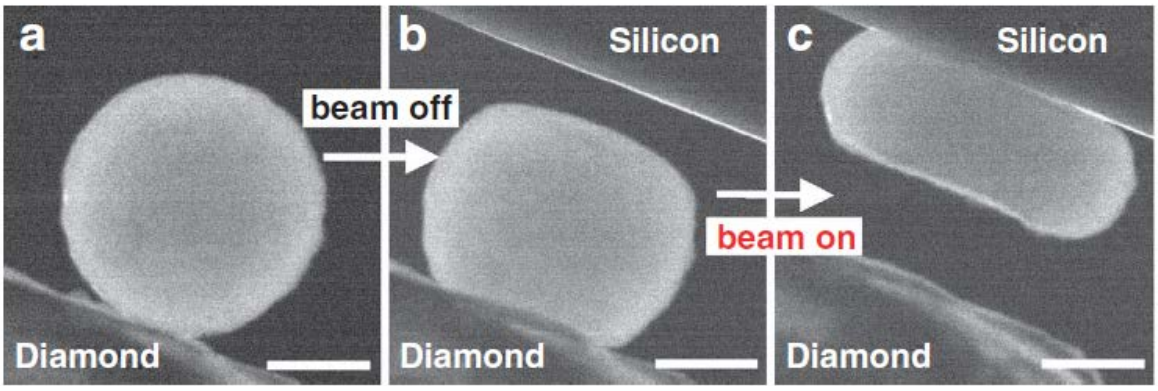

Figure 8: TEM images showing superplastic deformation induced in traditionally brittle amorphous silica particle by the TEM e-beam. Reprinted from Zheng et.al, 2010.

CHAPTER 3

EXPERIMENTAL TOOLS AND METHODS

This chapter describes the major tools and techniques that were used to synthesize the thin films and fabricate the MEMS based tensile testing stage.

The following is the overview of the process flow for the fabrication of the MEMS device.

1. Sputter deposition of thin film on Si wafer.
2. Spin coating of photoresist on top and bottom surfaces of wafer.
3. Alignment of the top side of the wafer with front side photomask and exposure of wafer to UV light through the mask.
4. Development of alignment marks on the top side of the wafer.
5. Alignment of back side mask with the developed alignment marks on the top side of the wafer.
6. Development of all MEMS device features on the top and bottom side of the wafer.
7. Reactive ion etching of metal from exposed regions on the top side of the wafer.
8. Through-thickness, anisotropic, deep reactive ion etching of the wafer from the bottom side of the wafer.
9. Removal of the remnant photoresist from the MEMS devices using an oxygen plasma asher.

3.1 Magnetron Sputtering System

A magnetron sputtering system (Orion 5 system manufactured by AJA International) was employed to synthesize all the thin films studied in this dissertation (Figure 9). Sputtering is a form of physical vapor deposition in which inert gas ions are used to knock off atoms from the material target onto a substrate. It is an excellent technique to deposit uniform thin films with fine control over the film thickness and composition. The Orion 5 system has three confocal magnetron sputtering guns, which can be operated individually or simultaneously. Simultaneous deposition from multiple targets makes the growth of alloys and metallic glass films possible. The tool possesses two DC and one RF power sources. The DC power sources are used to deposit metals while the RF source can be used to deposit semiconductors and insulators. Each gun is equipped with a pneumatically operated shutter that can be used to stop deposition from that specific gun. Ultra-high purity argon plasma is used to sputter off atoms from 2" diameter metallic or dielectric targets. It is also possible to clean substrates by back sputtering using the argon plasma by employing a RF reverse bias. The tool can also be used to grow dielectric thin films (SiN_x) by a reactive sputtering technique. This is achieved by introducing a gas like nitrogen along with the plasma forming argon. The main sputtering chamber is connected to a load lock through a gate valve. The presence of the load lock facilitates faster sample pump down and transfer times. The tool is equipped with two turbo molecular pumps (one for the main chamber and the other for the load-lock) backed up by mechanical pumps. This enables the system to routinely achieve base pressures better than 5×10^{-8} Torr upon proper chamber conditioning treatments. The conditioning steps include depositing gettering materials like titanium

and aluminum on the chamber walls and performing a bake-out of the chamber using heating strips. The substrate holder is made of Inconel and can be heated up to 800^{o}C by ceramic heating lamps. This enables the annealing of thin films during or post deposition.

Figure 9: Left: Orion 5 Sputter Deposition Tool used to synthesize metallic and amorphous thin films. Right: Magnetron sputtering guns having copper targets. Pictures courtesy AJA International.

3.2 Plasma Enhanced Chemical Vapor Deposition

An Oxford PECVD system (Figure 10) was used to grow SiN_x films on the silicon wafers prior to depositing metallic thin films that were to be subjected to annealing at high temperatures. The layer of SiN_x acts as an effective diffusion barrier and prevents the inter-diffusion of constituent elements of the thin film and the silicon substrate. The tool uses silane and ammonia as precursor gases to reactively grow SiN_x films while argon is used as the carrier gas. The depositions are carried out at a temperature of 350^{o}C.

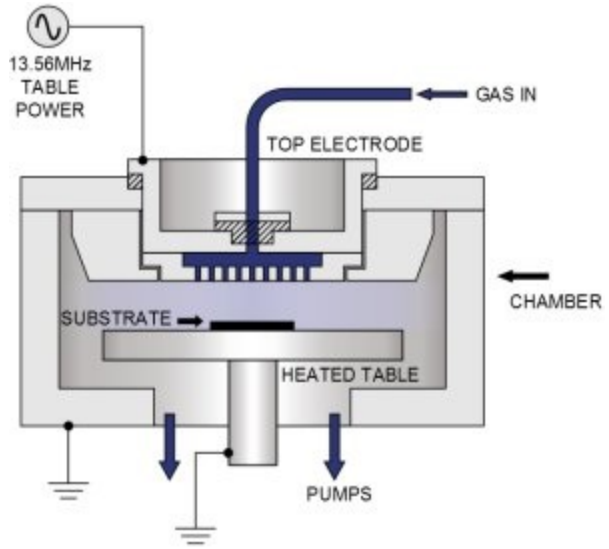

Figure 10: Layout of the Oxford PECVD tool. Picture courtesy Oxford Instruments.

3.3 Microfabrication Tools

Multiple microfabrication tools were employed to fabricate the MEMS tensile testing stage and to prepare TEM samples of the thin films. Photolithography and reactive ion etching techniques were extensively used to fabricate the MEMS device. The major tools are described below.

3.3.1 Photoresist Spinner

Photoresist spinners were used to spin coat AZ 4620 and AZ 4330 photoresists on the silicon wafers. A coat of HMDS (Hexamethlydisilazane) was initially applied on the wafers. Following this, photoresist was applied on the wafer using a pipette. The wafer was spun at speeds between 2000-4000 RPM to uniformly coat the photoresist on its surface. Depending on the spinning parameters and the kind of photoresist used, the

thickness of the resist layer obtained was between 3-6 µm. After spin coating, the wafers are subjected to a soft bake process at 100^0C to prepare it for the alignment step.

3.3.2 EVG 620 Aligner

After spin coating the wafers with photoresist, the EVG 620 aligner was used to align the chrome mask containing the MEMS device design (Figure 11) and the wafer. After aligning the wafer to specific alignment marks on the mask, the tool exposed the wafer to UV light. The exposed photoresist was subsequently developed using AZ 300MIF to reveal the MEMS device patterns on the wafer.

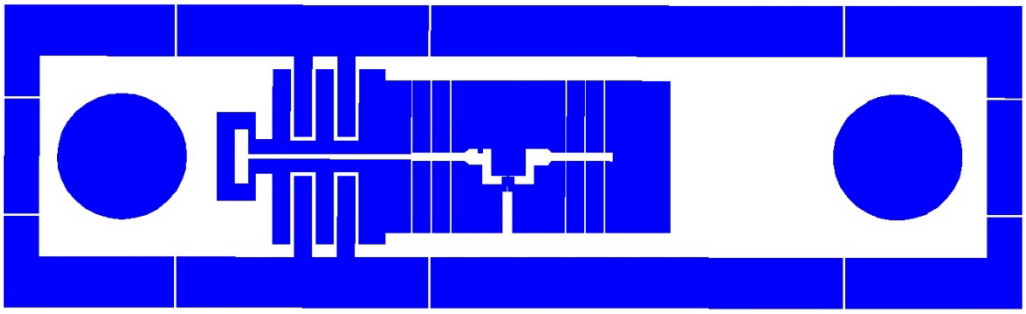

Figure 11: Design of back-side mask used in the EVG 620 aligner to transfer MEMS device pattern onto the wafers. White represents the opaque regions while blue represent transparent regions.

3.3.3 Oxford Plasmalab 80+ Reactive Ion Etcher (RIE)

Following the transfer of the MEMS device pattern onto the wafer, the metallic thin film layer was etched away in specific locations using the RIE (Figure 12). The tool uses plasma of Cl_2 and BCl_3 gases to etch away the metal layer using a combination of physical and chemical etching. The wafer is placed on the electrode of the tool to accelerate the plasma ions towards the wafer. This causes anisotropic etching of the metal

film with the etch rate normal to the wafer surface being greater than the etch rate in the plane of the wafer.

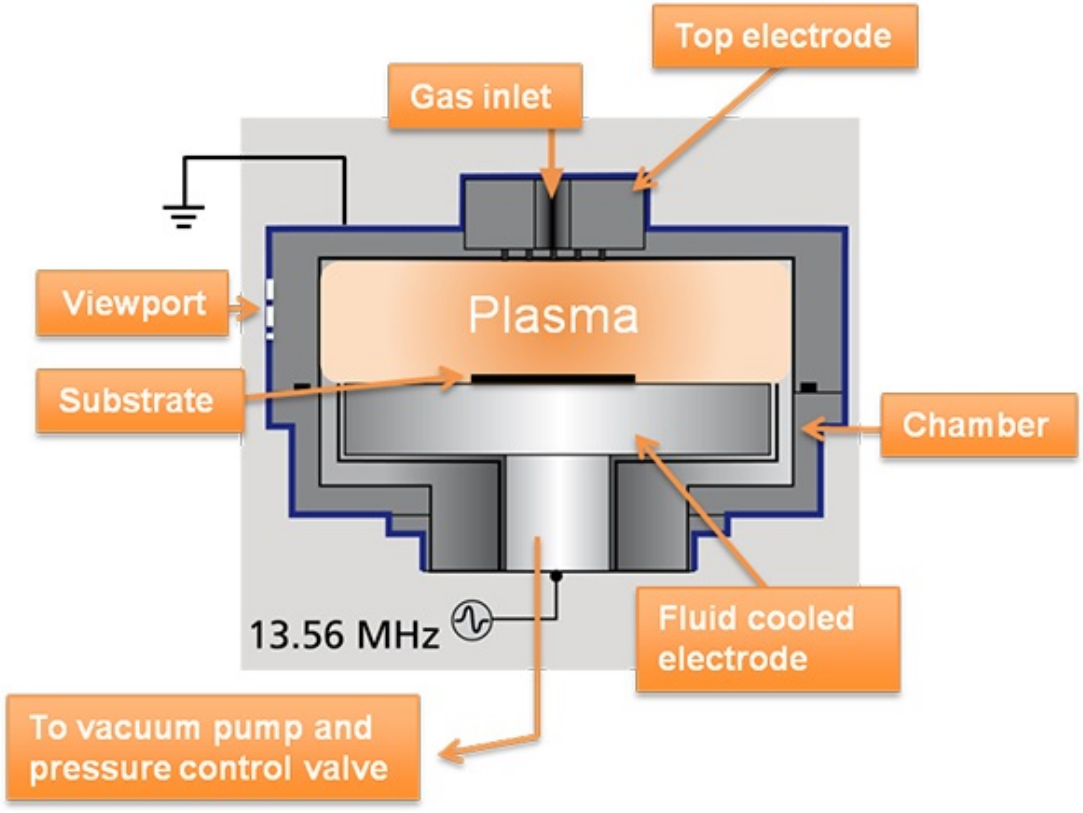

Figure 12: Layout of the RIE chamber. The BCl_3 and Cl_2 gases are used to anisotropically etch metal films. Image courtesy Oxford Instruments.

3.3.4 STS Advanced Silicon Etcher

Fabrication of the MEMS device required the etching of high aspect ratio features. Large depths needed to be etched while simultaneously ensuring that the walls of MEMS device beams remained vertical. This was achieved by using an inductively couple plasma etcher. This tool uses a two-step “Bosch” process to achieve extremely anisotropic etch features (Figure 13) (Abdolvand and Ayazi 2008).

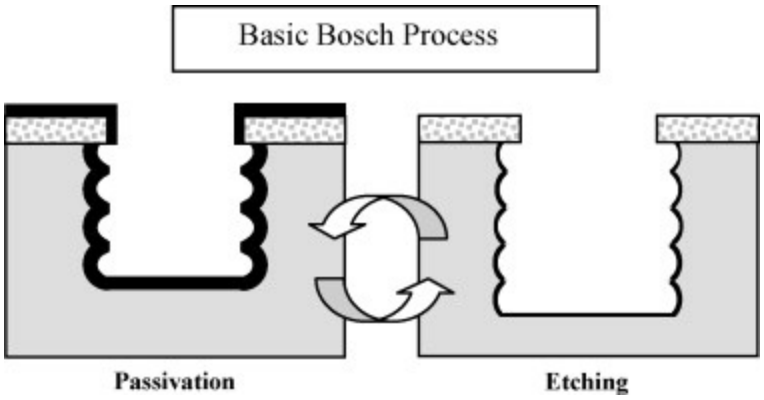

Figure 13 Schematic representation of the two step Bosch process (Abdolvand et. al, 2008).

The first step is the deposition of a thin passivation layer of C_4F_8. This layer serves the purpose of protecting the side walls of the MEMS device. Following this step, a SF_6 based plasma is used to etch away silicon in specific locations of the wafer. Cured photoresist acts as the etch mask while the developed regions of the photoresist are etched away. In this step, the electrode on which the wafer is placed accelerates the SF_6 ions towards it. As a result, a physical sputtering of atoms of the wafer takes place. Since the plasma ions are accelerated in a direction normal to the wafer surface, the passivation layer of C_4F_8, along with Si atoms, in the plane of the wafer surface are sputtered off more effectively. However, the passivation layer on features that are normal to plane of the wafer, do not get sputtered off by the plasma and are thus able to protect the vertical walls. Subsequently, chemical etching by the fluorine ions take place. Since the features in the plane of the wafer are not protected by the Teflon coating, they get etched away more easily while the side walls remain protected by the passivation layer. The tool continuously switches between the etching and passivation steps till the wafer is etched all the way through its thickness, thus, completing the fabrication of the MEMS device.

3.4 MEMS Tensile Testing Stage

A MEMS based tensile testing stage was used to conduct uniaxial tensile tests on freestanding thin films (Fig. 14). The device has a number of features that give it the unique capability to measure macroscopic stress and strain acting on the thin films while carrying out in situ TEM and SEM experiments.

The straining is achieved by pulling the device apart using pins that pass through the holes on each end. The pins are actuated by stages driven by motors or piezoelectric actuators. The freestanding thin film is connected to the MEMS device by a number of silicon beams. On one end of the beam, connecting the film to the device is a "T-bone" with a specific gap, which ensures that the sample does not accidentally get strained before an experiment (Figure 14). As the MEMS device is stretched from one end, the U-beams (Figure 14) get deformed. The deformation of the U-beams causes the T-bone gap to close. When the T-bone gap is eliminated, the sample is engaged and starts getting strained.

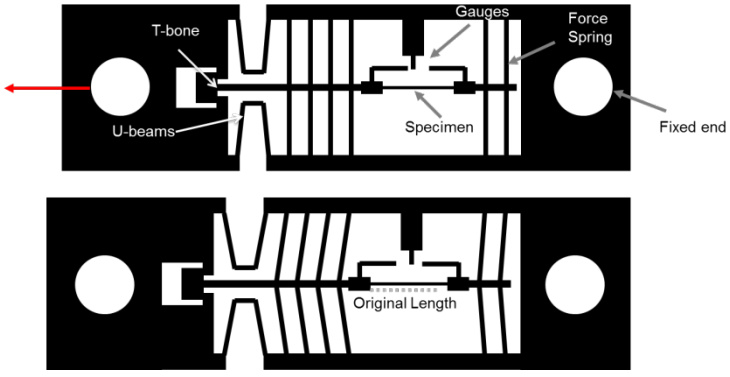

Figure 14: Image showing the operation of the MEMS device.

The device is equipped with a set of front beams, which eliminate any misalignment during the loading process and also protect the sample from damage from

air pressure gradients while loading and unloading from vacuum chambers. Three gauges are designed into the device to measure the macroscopic stress and strain acting on the sample (Figure 15 d). The strain sensing gauges x and y are attached on opposite ends of the sample. Thus, the change in relative displacement between x and y gives a measure of the elongation on the sample. The back beams of the device are designed to measure the stress acting on the sample. The sample and the back beams can be viewed as springs in series. As a result, the force acting on the back beams equals the force acting on the sample. The relative displacement between gauge x, connected to the back beams, and stationary gauge z is used to measure the deflection on the back beams. This deflection multiplied by the stiffness of the back beams, which is calibrated using a needle of standard stiffness, gives us the force acting on the sample. Due to the small footprint of the device, it can be used to carry out in situ TEM and SEM experiments. The device was developed in Prof Taher Saif's group at UIUC (Han and Saif 2006; Haque and Saif 2002).

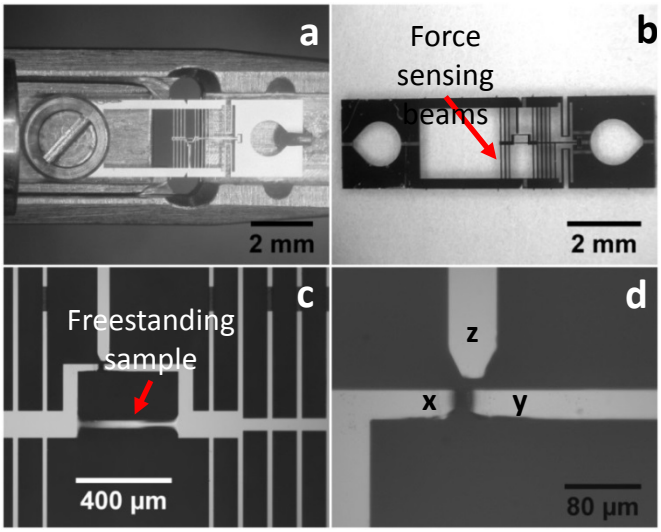

Figure 15: (a) The MEMS based tensile testing holder loaded on a TEM straining holder. (b) The deflection of the force sensing back beams enables the measurement of the stress acting on the specimen. (c) Freestanding thin film specimen. (d) The relative displacement between strain sensing gauges x and y corresponds to the elongation of the sample while the relative displacement of gauges x and z multiplied by the stiffness of the force sensing back beams gives a measure of

3.5 In situ TEM Setup

The freestanding metallic and amorphous thin films were subjected to in-situ TEM straining and annealing. In situ annealing was carried out to study the crystallization behavior of amorphous thin films while the in situ straining was used to investigate the mechanical behavior of nanocrystalline and amorphous thin films. The Philips CM200 and the FEI Tecnai F20 TEMs were used to carry out the in situ annealing. A Gatan single tilt heating holder having Tantalum heating elements was used to heat the thin films. The sample was resistively heated in the holder and the maximum annealing temperature achievable was 800^{o}C. The in situ straining experiments were carried out in Philips CM200 and JEOL ARM200F TEMs. A Gatan single tilt straining holder was used to strain the MEMS devices (Figure 16). Displacement pulses of about 150 nm were applied to the sample in each step followed by capturing images and diffraction patterns at areas of interest.

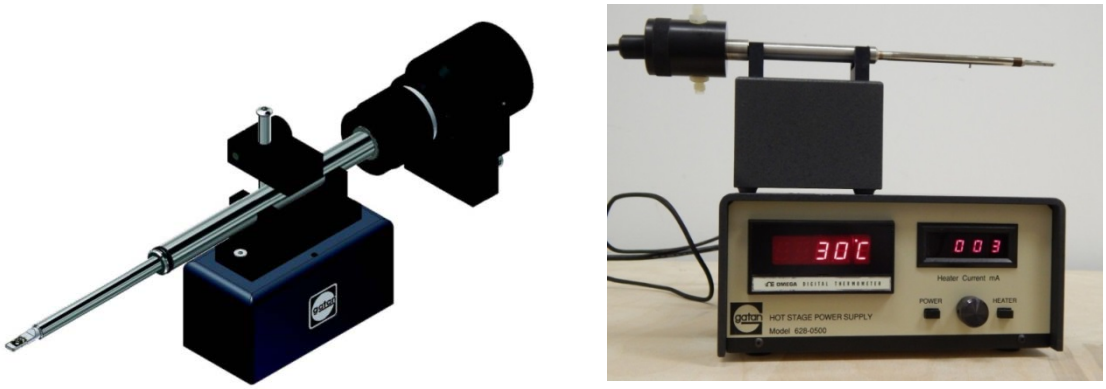

Figure 16: Left: TEM single tilt straining holder. Right: TEM heating holder. Pictures courtesy Gatan.

CHAPTER 4

Synthesis of Thin Films with Precisely Controlled Microstructures

4.1 Introduction

Synthesis of nanostructured materials with an optimal combination of mechanical properties requires rigorous and independent control of a diverse set of microstructural parameters. For instance, to simultaneously realize high strength and considerable ductility, it is necessary to control not only the mean size but also the size dispersion and spatial distribution of grains (Fang et al. 2011; Kou, Lu, and Li 2014; X. Wu et al. 2014). Unfortunately, current methods to synthesize nanostructured materials (Meyers, Mishra, and Benson 2006) can seldom satisfy these requirements. Here, a new methodology to precisely tune the nanostructure of thin films and coatings via systematic, in-situ seeding of crystalline nanoscale domains (seeds) into amorphous precursor films is presented. When the amorphous films are subsequently crystallized by thermal annealing, the seeds serve as preferential grain nucleation sites and control their microstructure. The capability and generality of this approach is demonstrated by meticulously tailoring the mean size, geometry and spatial distribution of nanostructured grains in structural (TiAl) as well as functional (TiNi) thin films. This approach, which is applicable to a broad class of metallic alloys and ceramics, enables explicit microstructural control of thin film materials for a wide spectrum of applications.

Nanostructured materials are typically synthesized using two distinct approaches - top down methods that involve attrition of bulk polycrystalline materials or bottom up

methods that involve the agglomeration of individual atoms or clusters. However, current synthesis methods that use either of these approaches provide little or no ability to tune a broad range of microstructural parameters simultaneously. Top-down methods like severe plastic deformation that are used to produce bulk nanostructured materials offer minimal capability to vary the grain size distribution or texture and often yield heterogeneous microstructures that exhibit large variation in mechanical properties (Valiev et al. 2006). Alternate bulk processing techniques like ball-milling and consolidation suffer from additional problems related to material purity and porosity (C. C. Koch, 2016). Bottom-up methods provide a greater capability to control the microstructure compared to top-down methods. In electrodeposition, for instance, the mean grain size can be reproducibly controlled by altering current densities or using additives (B. Y. C. Wu, Schuh, and Ferreira, 2005), but impurity contamination is still an issue. Physical vapor deposition (PVD) processes, which are typically used to synthesize nanostructured thin films, are cleaner than electrodeposition and allow us to vary the texture and mean grain size by changing the film thickness, substrate material, deposition rate or temperature (Thompson 2000). Nevertheless, the mean grain size of the films and their thickness cannot be easily decoupled and there is little control over the grain size dispersion or spatial distribution.

Hence, researchers have experimented with different methods to alter the various stages of microstructural evolution in thin films, which in the case of Volmer-Weber growth includes nucleation, island formation, coalescence and grain coarsening. In particular, several studies have focused on controlling the grain nucleation process through the use of seed layers or isolated seed crystals. However, these techniques have

only been used to control a narrow set of microstructural parameters in specific materials and their broader applicability is unclear.

Here, a new methodology is described to meticulously control the nanostructure of metallic alloy and ceramic thin films and coatings. The first step of the process (Figure 17a) is the deposition of a relatively thick (λ = 25-200 nm), amorphous layer of the thin film material at room temperature (RT). This can, for example, be accomplished by co-sputtering the constitutive elements of a metallic alloy. The next step is the deposition of a seed layer (0.5-2 nm thick) that has a crystalline structure at RT. As this layer is very thin, it is non-contiguous and results in the formation of crystalline nanoscale domains (seeds). The size and average spacing (δ) of these seeds can be controlled by varying the thickness of the seed layer or the deposition rate and temperature (Thompson 2000). These steps are repeated until the desired overall film thickness is obtained. Finally, the amorphous matrix with the seeds is crystallized by annealing at high temperature. During annealing, the seeds serve as preferential grain nucleation sites and control the final microstructure of the films. Since both λ and δ can be independently varied during each step of the growth process, the size, dispersion and spatial distribution of grains can be explicitly controlled.

4.2 Materials and Experimental Procedure

Plasma enhanced chemical vapor deposition (PECVD) was used to deposit 60 nm thick SiN_x onto 200 μm thick (100) silicon wafers. The SiN_x was deposited to prevent inter-diffusion between the silicon substrate and the thin film during annealing. TiAl and TiNi thin films were then co-deposited on the Si/SiN_x substrate by DC magnetron

sputtering using an ATC Orion 5 sputter system manufactured by AJA International. These films were deposited using 99.999 % pure Ti, Al, Cr and Ni targets manufactured by Kurt J. Lesker Company and were amorphous in the as-deposited state. The composition of the films was controlled by tuning the power of the individual sputtering guns. Rutherford backscattering spectrometry was used to determine the atomic composition of the films and X-ray diffraction was used to confirm the amorphous nature of the films.

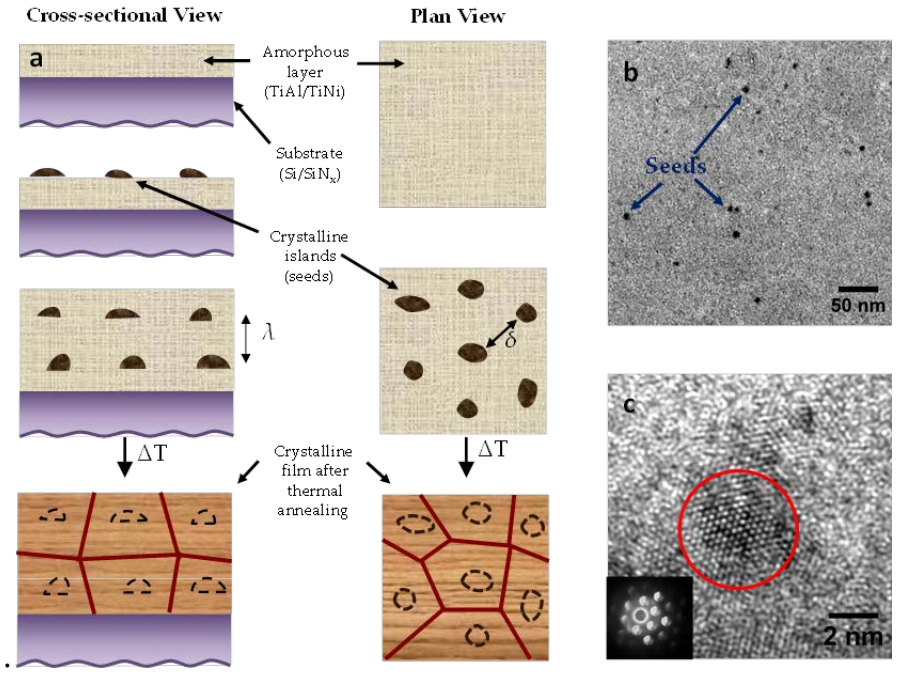

Figure 17: Schematic of the process: (a) First, an amorphous layer of the thin film material (TiAl/TiNi) is deposited on a substrate (Si/SiNx). Next, a thin crystalline seed layer (Ti/Al/Cr) is deposited on the amorphous layer. The seed material is chosen such that this layer is non-contiguous and leads to the formation of crystalline nanoscale domains (seeds). A second amorphous layer is then deposited to sandwich the seeds. These steps are repeated until the desired film thickness is obtained. λ is the spacing of the seed layers along the film thickness, while δ is the in-plane spacing between the seeds. Both λ and δ can be independently varied during each step by altering the deposition parameters. Following the deposition, the film is thermally annealed to crystallize it. The seeds serve as grain preferential nucleation sites during annealing and hence the grain heights and diameters scale with λ and δ, respectively. (b) TEM bright-field image showing a dispersion of crystalline Ti seeds on an amorphous TiAl layer. (c) HR-TEM image showing the atoms on the (0001) plane of a Ti seed (red circle) surrounded by the amorphous TiAl matrix. The CBED pattern of the seed is shown in the inset.

The co-deposition of the films was carried out at room temperature at a base pressure of 5×10^{-8} Torr and an argon deposition pressure of 3 mTorr. The co-deposition was stopped at specific periods and thin (0.5-2 nm thick) layers of pure Ti, Al or Cr was deposited on the amorphous TiAl and TiNi films. These thin Al, Ti or Cr layers were crystalline in nature and formed nanoscale domains (seeds), which acted as preferential grain nucleation sites when the amorphous films were crystallized by thermal annealing. After the deposition of the crystalline seed layer, the co-deposition of TiAl and TiNi was resumed so that the crystalline seeds were encapsulated by two amorphous layers. This process was repeated to obtain a film comprised of single or multiple seed layers and the desired thickness. The thickness of the seed layers and their number and spacing were systematically altered to study the effect of seeds on the final microstructure. After the deposition was complete, the films were either annealed under vacuum ($< 10^{-6}$ Torr) in the sputtering chamber or annealed in a FEI Tecnai F20 transmission electron microscope (TEM) using a Gatan TEM heating holder. For annealing experiments inside the sputtering chamber, the temperature was increased to the final value within five minutes and held steady for the required amount of time. For the in-situ TEM annealing, the temperature was increased gradually to counteract the thermal drift of the specimen.

TEM specimens were fabricated out of Si/SiNx wafers having the TiAl/TiNi films on the top surface using microfabrication techniques. First, photoresist was spin coated on back of the wafer. An EVG620 mask aligner was then used to align the coated wafer with a glass mask containing the TEM specimen patterns and exposed to UV light. The exposed photoresist was then developed to complete the pattern transfer. An STS deep

reactive ion etcher was then used to back etch the wafer to reveal the freestanding thin film TEM specimen. The plan-view microstructures of the films were then analyzed using a JEOL 2010F TEM while in-situ heating experiments were carried out using the FEI Tecnai F20 TEM. A FEI NOVA200 dual beam focused ion beam and scanning electron microscope was used to fabricate cross-sectional TEM samples using conventional lift out techniques. The mean grain size of the films was typically calculated from TEM bright-field images. When the mean grain size was found to be <100 nm , the values were corroborated with measurements determined using the Scherrer formula from X-Ray Diffraction (XRD) peak profiles obtained using a PANalytical X'Pert PRO XRD tool.

4.3 Results and Discussion

A series of systematic studies were performed to test the viability of the process and uncover the effects of seed density and distribution on the microstructure of TiAl and TiNi thin films. The amorphous layers in the TiAl films had a nominal atomic composition of 45% Ti and 55% Al, whereas the TiNi films were equiatomic.

First, whether the thin seed layers indeed lead to the formation of well-dispersed, nanosized seeds was verified (Figure 17b). The crystallinity of the seeds was confirmed (Figure 17c) using high resolution transmission electron microscopy (HR-TEM) and convergent beam electron diffraction (CBED), and their chemical composition was verified using energy dispersive X-ray spectroscopy (Figure 18).

It should be noted that the presence of well delineated seeds does not preclude the possibility of locally contiguous layers of the seed material. Similarly, only a fraction of the seeds, which are above a critical size and have appropriate crystal orientations to produce diffraction contrast, are visible in the bright-field TEM image. Nonetheless, the average size and spatial distribution of the seeds are significantly different for different seed layer thicknesses (Figure 19), which strongly suggests that seed formation is not controlled by defects on the surface of the amorphous layer.

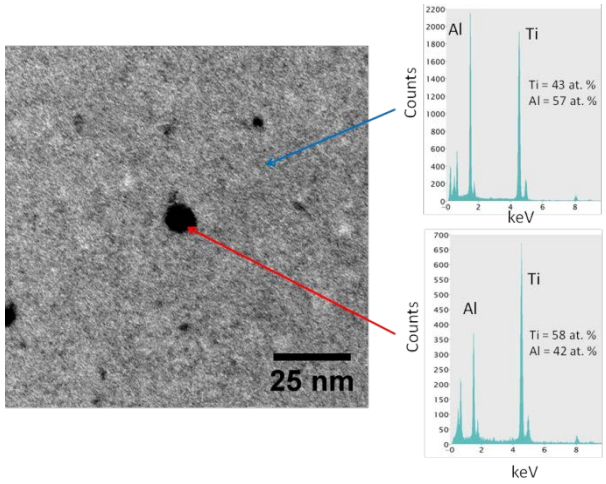

Figure 18: Composition of seed crystals: TEM bright-field image of a 40 nm thick amorphous TiAl film with a 1 nm thick Ti seed layer in the middle, before annealing. Isolated Ti seeds are clearly visible. Energy dispersive X-ray spectroscopy (right) of the seed region (indicated by red arrow) and the amorphous matrix (indicated by blue arrow) reveals the difference in their composition. Note that the composition of the seed region also includes the amorphous matrix encapsulating the seed. The accuracy of the composition determined by the method is ±2 %.

The seeds were found to modify both the crystallization kinetics and the final microstructure of the films. When seeded and unseeded amorphous TiAl films were annealed at 550^{o}C for a period of two hours, partial crystallization in the seeded film was observed, whereas the unseeded film remained completely amorphous (Figure 20).

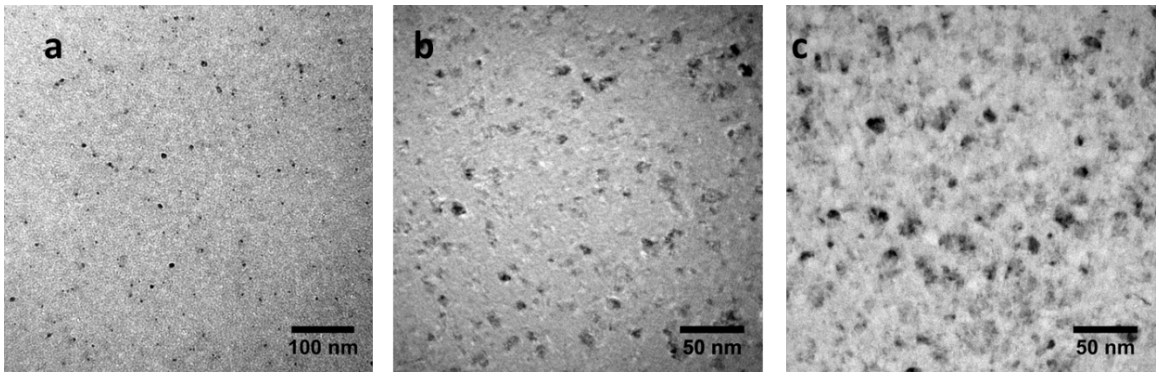

Figure 19: Effect of seed layer thickness on size and spatial distribution of seeds: TEM bright-field images of (a) 40 nm thick TiAl film with 0.5 nm thick Ti seed layer in the middle before annealing. (b) 40 nm thick TiAl film with 1.5 nm thick Ti seed layer in the middle before annealing. (c) 40 nm thick TiAl film with a 2 nm thick seed layer in the middle before annealing.

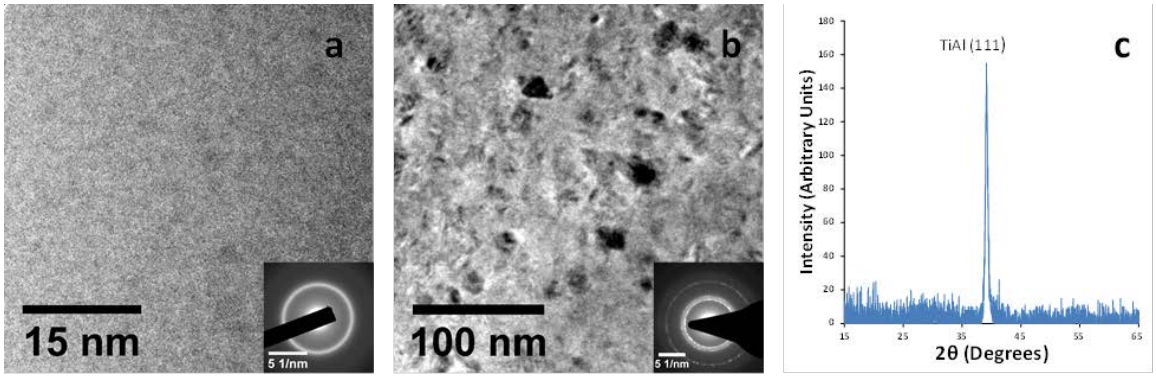

Figure 20: Enhanced crystallization due to seeds: (a) TEM bright-field image of a TiAl film with no seed layer after 2 hours of annealing at 550^{o}C. This film remains completely amorphous as indicated by the diffuse ring in the selected area diffraction (SAD) pattern (inset). (b) TEM bright-field image of the TiAl film with a single 1 nm thick Ti seed layer in the middle after 2 hours of annealing at 550^{o}C. The film showed partial crystallization and spots started to appear in the SAD pattern (inset). (c) XRD pattern of the film in (b). The presence of a well-defined (111) ϒ-TiAl peak indicates that the film has started to

More interestingly, the seeded films exhibited a much smaller mean grain size (d_m) compared to the unseeded films when the annealing temperature was increased. Figures 21a and 21b show microstructures of TiAl films without and with Ti seeds annealed at 600^{o}C for a period of four hours. The unseeded films had $d_m \sim 1$ μm, whereas the seeded film had a $d_m = 62$ nm. Notably, the seeded film retained its nanostructure (d_m

= 63 nm) even upon annealing at 750^{o}C (Figure 21c), which is approximately 0.6 times the melting temperature (T_m) of TiAl. This high thermal stability contrasts with the typical behavior of nanostructured metals, which show abnormal grain growth even at low temperatures (Ames et al. 2008; Kacher et al. 2011). The same microstructural stability was also observed when an Al seed layer was used instead (Figure 22). This thermal stability can be due to two specific reasons. Firstly, most of the grains in the TiAl films had a (111) out-of-plane texture. Since this plane of atoms has the lowest surface energy (C. V. Thompson, 1990), further growth of the grains driven by surface energy minimizations would have been curtailed. Secondly, these films were found to buckle when they were released from their substrates. This indicates that the films were under compressive stresses because of the thermal mismatch between the substrate and the film. As compressive residual stresses retard diffusion processes, grain growth by diffusion would have been minimized.

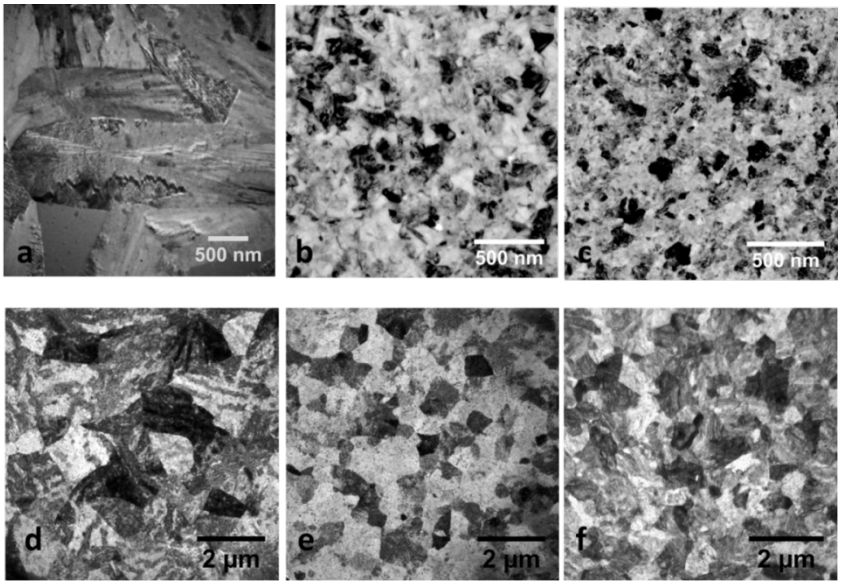

Figure 21: Grain growth inhibition by seed crystals: Bright-field TEM images of: (a) 100 nm thick TiAl film with no seed layer after annealing at 600^{o}C for 4 hours showing large micrometer-sized grains (d_m ~ 1 μm). (b) 100 nm thick TiAl film with a single 1 nm Ti seed layer after annealing at 600^{o}C for 4 hours (d_m =

42 nm). (c) 100 nm thick TiAl film with a single 1 nm Ti seed layer after 4 hours of annealing at 750°C. The grains remain in the nanocrystalline regime (d_m = 48 nm) and show little growth compared to (b). (d) 100 nm thick TiNi film with no seed layer after annealing at 600°C for 4 hours. Large micrometer-sized grains are visible and d_m = 1.4 μm. (e) 100 nm thick TiNi film with a single 1 nm thick Ti seed layer after annealing at 600°C for 4 hours (d_m = 540 nm). (f) 100 nm thick TiNi film with a single 1 nm thick Ti seed layer after annealing at 750°C for 4 hours. The film had a smaller mean grain size (d_m = 580 nm) compared to the unseeded film in (d) even at this temperature. For all the seeded films, the seed layer was deposited in the middle of the film.

It is noted that the Ti and Al seed layers change the overall composition of Ti and Al in the film by less than 1% and do not induce the formation of additional phases, which may alter the grain size. Both the unseeded and seeded films are primarily composed of the gamma phase, as revealed by X-ray diffraction (Figure 23). The same trends in d_m were observed in the unseeded and seeded TiNi films as well but d_m was significantly higher compared to TiAl films (Figures 21d-f).

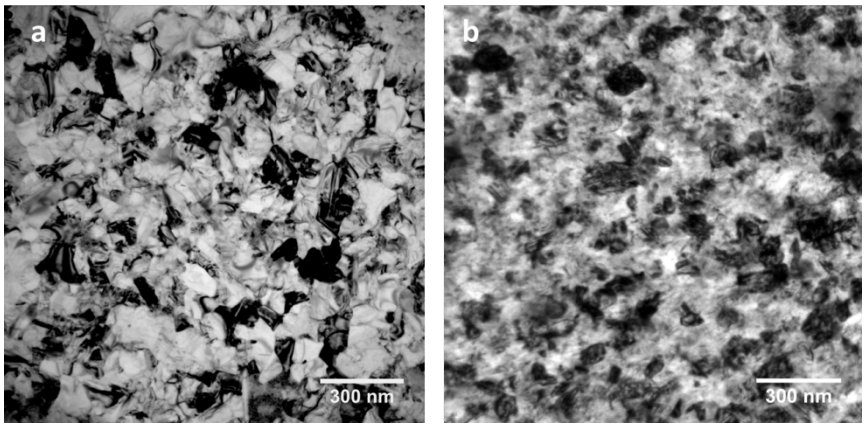

Figure 22: TiAl films with Al seeds: TEM bright-field image of (a) TiAl film, 100 nm thick with a single 1 nm Al seed layer in the middle after 4 hours of annealing at 650°C. The film was nanostructured at this temperature. (b) TiAl film, 100 nm thick with a single 1 nm Al seed layer in the middle after 4 hours of annealing at 750°C. The film retained its nanostructure even at this elevated temperature.

As indicated in Figure 17, if the seeds act as preferential nucleation sites, the mean in-plane spacing between the grain nuclei should scale with δ and the number of grains across the thickness should scale with the number of seed layers. In effect, a larger

δ and λ should lead to a larger mean diameter and height, respectively, for the grains. To test this assumption, δ and λ were systematically varied and the resultant microstructures of the films analyzed. To increase δ for a given seed layer thickness, coarsening and coalescence of the seeds was induced (Thompson 2000) by increasing the film temperature (T_{seed}) for a short period of time immediately after the seed layer was deposited. We note that T_{seed} was sufficiently small ($\leq 150^{o}C$) to avoid crystallization of the amorphous layer underneath. After this step, the film was allowed to cool back to RT and the subsequent amorphous layer was deposited. Figures 24 (a-c) provide direct evidence that by altering δ the mean grain size can be systematically varied. The mean grain size of the TiAl films was least (62 nm) when no seed coalescence was induced and progressively increased with increasing T_{seed}, even though all other material parameters (type, number and thickness of seed layers, and film composition) and annealing conditions for crystallization were identical.

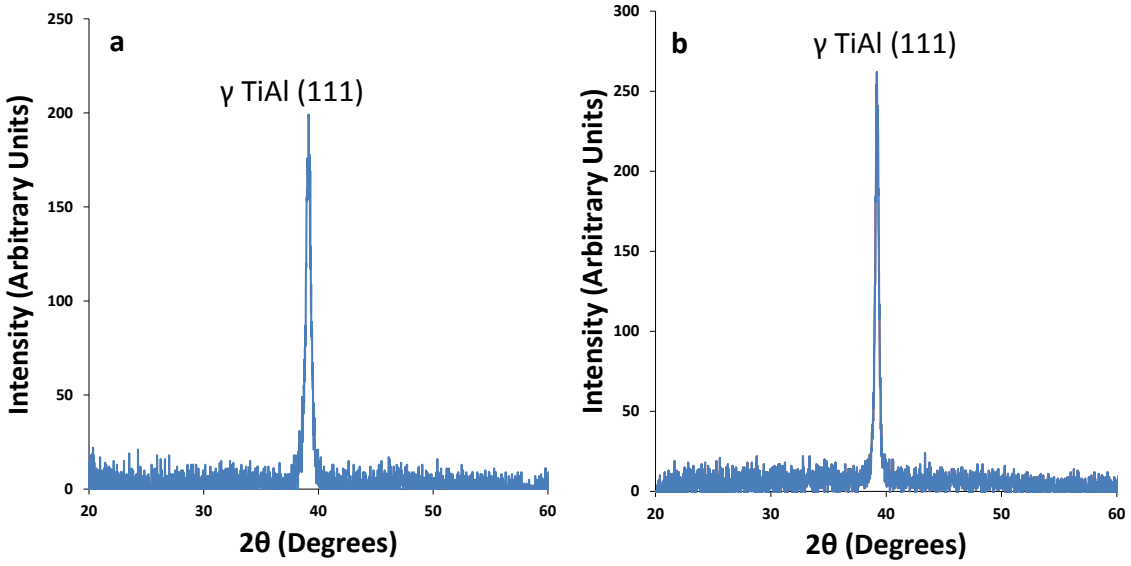

Figure 23: Texture of TiAl films: (a) XRD measurements show the strong (111) texture of a TiAl film with a 1 nm Al seed layer after 4 hours of annealing at $650^{0}C$. (b) XRD measurements of a TiAl film deposited without any seed layer after 4 hours of annealing at $600^{0}C$. This film also exhibits a strong (111) texture.

To ascertain the effect of λ, films with different number of seed layers were synthesized and their microstructures analyzed through cross-sectional TEM (Figure 25). The TEM analysis revealed that when a single seed layer is used, the grains in the crystallized film are columnar and typically traverse the entire thickness (Figures 25 a, d). In contrast, when more than one seed layer was used, multiple grains with more equiaxed structure were observed across the film thickness (Figures 25 b, e). More importantly, the average number of grains across the thickness scaled with the number of seed layers, which provides further proof that the seeds act as preferential grain nucleation sites and control the microstructure.

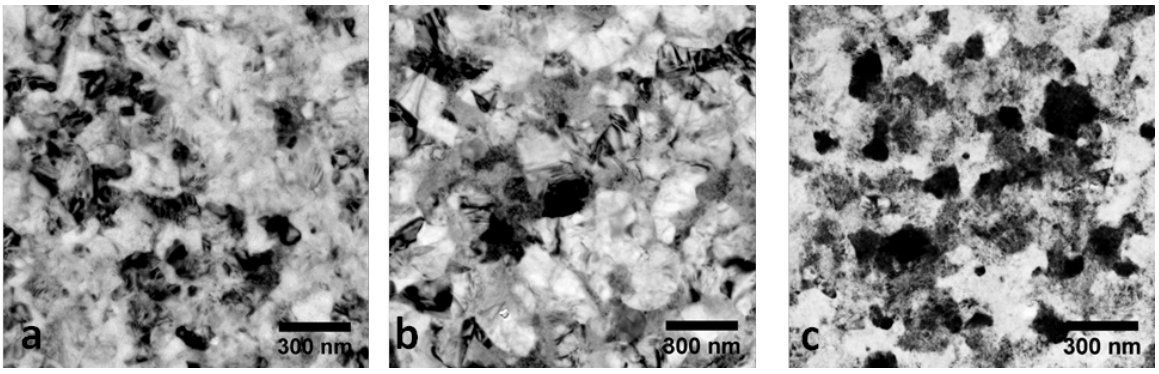

Figure 24: Tailoring the mean grain size (d_m) of films: (a-c) TEM bright-field images of three different 100 nm thick TiAl films with a single 1 nm Ti seed layer after annealing at 600^0C for 4 hours. In addition to the final 600^0C annealing, the films in (b) and (c) were subjected to a low temperature thermal anneal (T_{seed}) for 10 min immediately after the seed layer was deposited to increase the inter-seed spacing (δ) by promoting seed coalescence. For the film in (a) which was not subjected to the low temperature anneal d_m = 62 nm. The film in (b) was subjected to $T_{seed} = 100^0$C and d_m increased to 140 nm. When T_{seed} was increased to 150^0C for the film in (c), d_m further increased to 170 nm. In all the

Apart from the ability to explicitly tailor the grain diameters and geometry, the method also enables systematic control of the size dispersion and spatial distribution of grains. To demonstrate this capability, λ and δ were varied across the thickness to create films with specific gradient microstructures. For instance, the films in Figures 25c and 25f are composed of smaller, equiaxed grains near the top and bottom and larger grains in

the middle, whereas the film in Figure 26 has ultrafine grains (d_m > 200 nm) in one half and nanocrystalline grains (d_m < 50 nm) in the other half. As mentioned earlier, such gradient/multimodal microstructures enable high strength, ductility and fatigue resistance (Yang et al. 2013) and promote significant deformability even in materials that exhibit limited plasticity (Edalati et al. 2012). The highly heterogeneous microstructure will also considerably enhance the capability of nanostructured materials to recover inelastic strain and dissipate energy (Rajagopalan, Han, and Saif 2007).

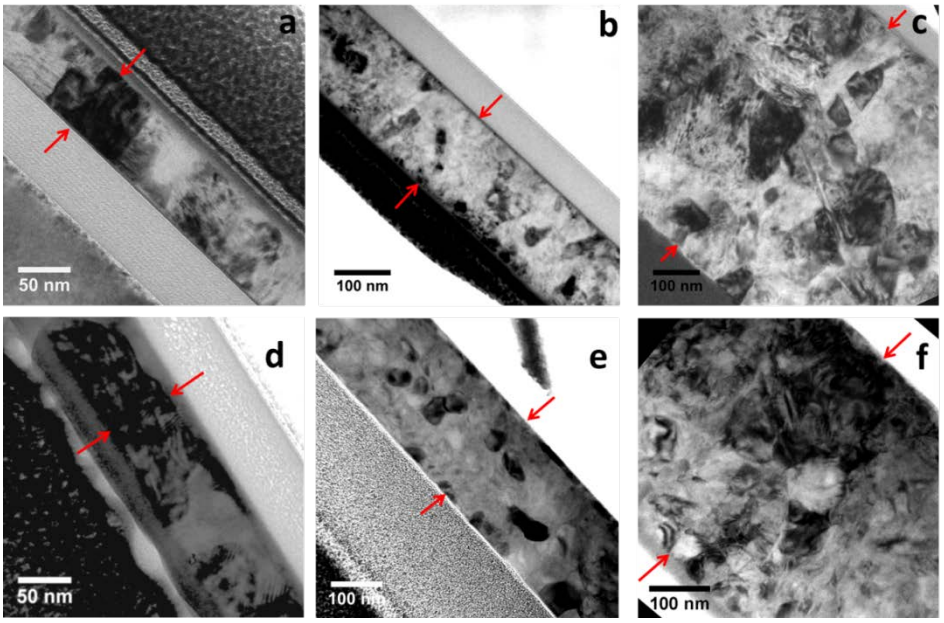

Figure 25: Control of grain geometry, size dispersion and spatial distribution: TEM bright-field cross-sectional images of: (a) A 100 nm thick TiAl film with a single 1 nm thick seed layer in the middle after annealing at 650°C for 4 hours. The grains typically traverse the entire thickness of the film and have a columnar structure. (b) A 200 nm thick TiAl film, with four 1 nm thick Ti seed layers spaced 50 nm apart, after annealing at 650°C for 4 hours. Multiple grains along the thickness are observed. (c) A TiAl film, with smaller seed layer spacing near the top and bottom and larger spacing in the middle, after annealing at 650°C for 4 hours. A gradient microstructure is formed upon annealing. (d) A 100 nm thick TiNi film with a single 1 nm thick Ti seed layer in the middle after annealing at 650°C for 4 hours. Similar to (a) single grains traverse the thickness of the film. (e) A 200 nm thick TiNi film, with four 1 nm thick Ti seed layers, after annealing at 650°C for 4 hours. Multiple grains along the thickness are observed. (f) A TiNi film, with multiple seed layers and varying λ, after annealing at 650°C for 4 hours. A gradient in the grain size can be seen along the thickness similar to (c). The red arrows in the figures indicate the TiAl and TiNi film cross-sections.

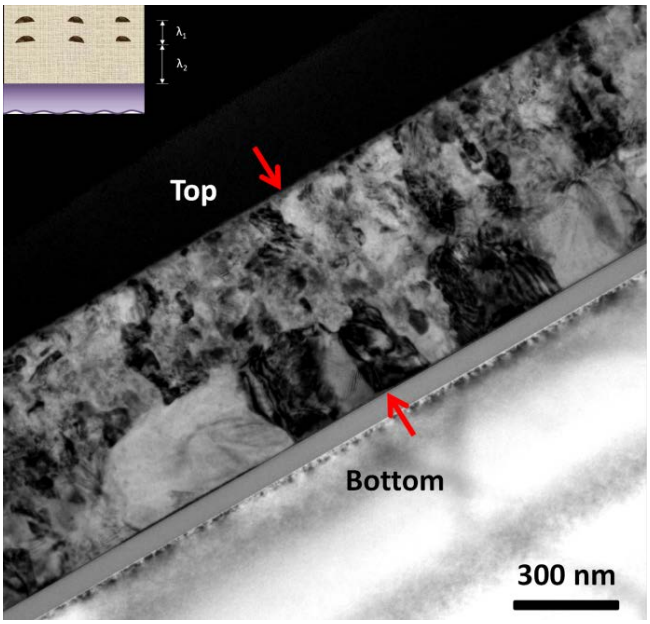

Figure 26: TiAl film with gradient microstructure: Cross-sectional TEM image of a TiAl film which was grown to have ultrafine grains (> 200 nm) in the bottom half and nanocrystalline grains (< 50 nm) in the top half. The gradient microstructure was obtained by having a much larger seed layer spacing (λ) in the bottom half of the film compared to the top half.

To investigate how the seeds alter the crystallization process, in-situ TEM annealing of TiAl films with and without seed layers was carried out. The experiments reveal that the seeds indeed act as preferential grain nucleation sites and a large number of grains are simultaneously nucleated in the seeded films as the temperature is increased (Figure 27). Since the spacing between the grains is inversely related to their density, the average size of the grains when they impinge on each other is small.

Furthermore, because the nucleated grains have a strong (111) texture (Figure 23), abnormal grain growth induced by surface energy minimization is restricted (Vitos et al. 1998). Therefore, grain growth after impingement is minimal. In contrast, the crystallization process was significantly different in the unseeded films, where only a

small number of grains nucleated upon annealing. Typically, the spacing between the nuclei was in the order of micrometers, which led to a significantly larger mean grain size (Figures 27 c, d,). In other words, the crystallization of the unseeded metallic glass films was growth controlled and not nucleation controlled. Such growth controlled crystallization has been recently observed in other metallic glass thin films as well (Lee et al. 2016).

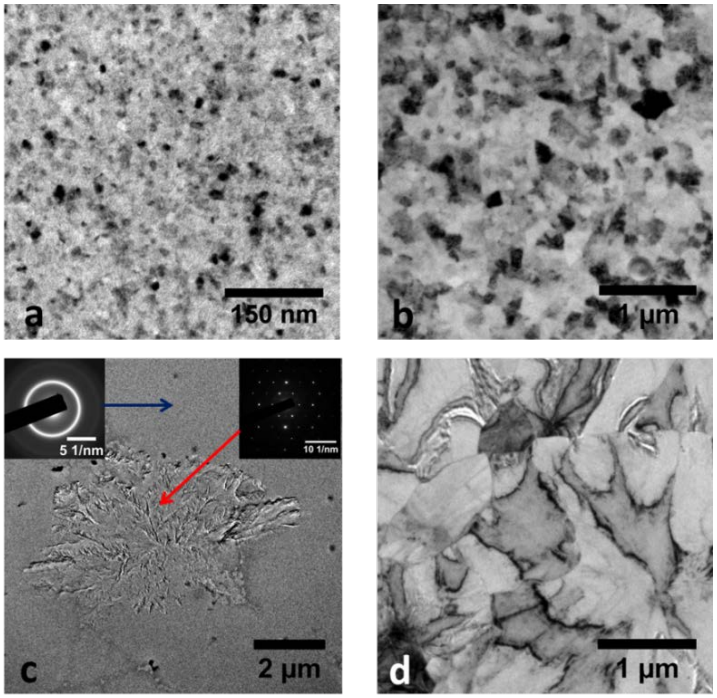

Figure 27: In-situ TEM annealing: (a-b) TEM bright-field images taken during in-situ annealing of a 100 nm thick TiAl film with a single 1 nm thick Ti seed layer in the middle. The image in (a) was taken after heating the film at 550^{o}C for 1 hour and shows small grains with sizes ranging from 5-25 nm. Figure (b) corresponds to the film after heating at 650^{o}C for 30 minutes and shows nanostructured grains. (c-d) TEM bright-field images taken during in-situ heating of a 100 nm thick TiAl film with no seed layer. The image in (c) was taken after heating the film at 600^{o}C for 1 hour and shows the nucleation of a large crystalline phase (red arrow), as revealed by the corresponding selected area diffraction pattern. The rest of the film (blue arrow) still remained amorphous. Figure (d) corresponds to the film after heating at 650^{o}C for 30 minutes and shows the formation of large micrometer-sized grains.

Having attained control over the grain size and dispersion using the seed mediated crystallization technique, the possibility of altering the phases of the films needed to be

investigated. To conduct this study, NiTi was chosen as the material system as its mechanical behavior changes significantly depending on whether it exists in the austenite or martensite phase (X. Huang, Ackland, and Rabe 2003). XRD and microstructural analysis of the NiTi films synthesized by using Ti seeds revealed that they were predominantly martensitic at room temperature (RT) (Figure 28a).

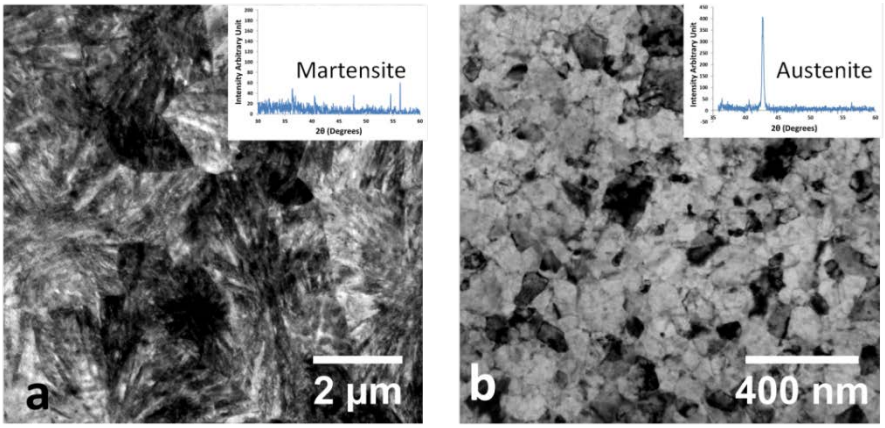

Figure 28: The nature of the seed element was found to have an effect on the final phase of the films after annealing. In TiNi films, Ti seeds were found to stabilize the martensite phase as seen in (a) while Cr seeds stabilized the austenite phase as seen in (b). This provides us with a template to control the phases emerging in an intermetallic system.

With a stable martensite phase at RT, the only way to induce phase transformation in NiTi is by using a thermal stimulus. The pseudoelastic behavior of NiTi on the other hand, is driven by a stress induced phase transformation from the austenite to martensite phase. Thus to study the pseudoelasticity of NiTi, which plays a critical role in actuation and sensor applications, we require the material to be in its austenitic phase. In this regard, it is known that adding a minute amount of chromium (1-2 atomic %) to NiTi can have an effect of stabilizing the austenitic phase (Hosoda et al. 1998). To combine the austenite stabilization effect of the Cr in conjunction with the seed mediated crystallization process, 100 nm thick NiTi thin films with 1nm thick Cr seed layers were

synthesized. Upon annealing at 600^0C for 4 hours it was found that the Cr seeds stabilized the austenite phase and restricted the grain size to 120 nm (Figure 28b). Thus, control of the grain size as well as the phase in NiTi films was attained by using a Cr seed layer.

4.4 Conclusions

The results described above demonstrate the capability of the method to tune the mean size, geometry, size dispersion, spatial distribution and phase composition of grains in thin films. TiAl and TiNi have been used to demonstrate viability in this study, but this approach can be extended to a broad class of metallic alloys and ceramics that can be deposited in the amorphous state. Examples of such materials include binary (CuZr, FeAl, NiAl, ZrTi), ternary (ZrCuAl, PdCuSi) and quaternary (ZrAlCuNi) alloys and ceramics such as SiC and WC (Masui et al. 1985; C. J. Chen et al. 2009; El Khakani et al. 1994; Rincón et al. 2003; Chu et al. 2012). In this context, it should be mentioned that materials synthesized by vapor deposition are farther from equilibrium compared to those obtained by liquid-to-solid processes, which are typically used to produce bulk metallic glasses. Thus, a larger spectrum of metallic alloys (over wider composition ranges) can be deposited as amorphous thin films (Chu et al. 2012). It is also relevant to note that seed layers have been shown to influence the growth of ceramic nanostructures (Greene et al. 2005) and nanostructuring leads to enhanced hardness and fracture toughness in SiC and WC (Szlufarska, Nakano, and Vashishta 2005).

While this chapter has focused on the control of grain size, structure and spatial distribution, the approach outlined here provides a rich design template to manipulate the microstructure of ceramic and metallic alloy films. For example, non-constituent elements can be used as seed layers to nucleate and stabilize metastable phases (Schleip, Herlach, and Feuerbacher 1990) that cannot be obtained by conventional processing routes. Note that many metals form isolated islands during the initial stages of film growth on amorphous substrates (Venables, Spiller, and Hanbucken 1984) and hence can be employed as seed layers. Likewise, seed layers can be used to precisely alter the local composition and nucleate additional phases that have complementary properties to the primary phase. For instance, by selectively using thicker Ti seed layers near the surface, the lamellar phase (higher Ti composition, better fracture toughness) can be nucleated to mitigate surface crack initiation in gamma TiAl films that have high specific strength and thermal conductivity (Westbrook, n.d.). Thus, this approach can enable the synthesis of novel thin film materials with unique microstructural features and physical properties, which are unattainable using current processing techniques. Finally, in addition to sputtering, the approach outlined here is directly applicable to other PVD processes such as evaporation and, in principle, can be adapted to electrodeposition, provided amorphous microstructures can be obtained (Moffat 1994; Trelewicz and Schuh 2007).

CHAPTER 5

In situ TEM Straining of NiTi Thin Films with Tailored Microstructures

5.1 Introduction

Nickel-titanium alloys are known to exhibit shape memory behavior. These materials undergo a transformation from a high temperature austenite phase (B2) to a low temperature martensite phase (B19') (X. Huang, Ackland, and Rabe 2003). This transformation can be induced by a thermal or mechanical stimulus. The transformation is usually reversible upon the removal of the thermal or mechanical stimulus and forms the basis for the shape memory or pseudoelastic behavior. These materials are technologically important as they exhibit extremely large transformation stresses and strains and thus can be used in a wide range of applications in the medical and aerospace industry (Fu et al. 2004). Moreover, nanoscale NiTi thin films also find applications as actuators and sensors in MEMS devices (Fu et al. 2001).

In these materials the stress induced transformation from the austenite to martensite phase is known to be extremely sensitive to the composition and the microstructure (Otsuka and Ren 2005). It has been shown the transformation paths change drastically with increasing Ni or Ti content in these materials (Hosoda et al. 1998). Adding a third alloying element like Co or Cr has also been shown to have a significant effect on the shape memory behavior (Hosoda et al. 1998).

Moreover, grain size also influences the transformation in NiTi. Research studies have shown that with decreasing grain size the transformation from the austenite to the

martensite phase becomes increasingly difficult (Waitz et al. 2007). Thus, there are many nanoscale microstructural aspects that need to be investigated in this system. Although in situ TEM techniques have been used to study the behavior of microcrystalline and single crystal NiTi alloys (Waitz, Kazykhanov, and Karnthaler 2004; J. Ye et al. 2010), the behavior of these materials in the nanocrystalline regime remains relatively unexplored. Nanocrystalline metals and alloys are known to exhibit significantly higher yield strength and hardness compared to coarse grained materials (Kumar, Van Swygenhoven, and Suresh 2003). Thus combining the shape memory behavior of NiTi with a nanocrystalline grain structure could substantially increase the transformation stress in these materials. As the transformation stress influences functions like actuation and damping, nanocrystalline NiTi alloys could provide capabilities that are beyond the reach of conventional coarse-grained shape memory alloys. Additionally, nanocrystalline materials with a heterogeneous distribution of grain sizes have been shown to recover plastic strain (Rajagopalan, Han, and Saif 2007). This recovery is driven by inhomogeneous distribution of stresses within grains of different sizes. Thus keeping the grain size of NiTi in the nanocrystalline regime could potentially open up an additional pathway for strain recovery.

In this study, nanocrystalline NiTi thin films were sputter deposited using the seed mediated crystallization process described in Chapter 4. Chromium seed layers were used to stabilize the austenitic phase and maintain a nanocrystalline grain size. These films were subjected to in situ TEM straining to study the stress induced martensite transformation. Experiments revealed that stress induced transformation in these

materials was accompanied by plastic deformation in austenitic grains. Moreover, the transformation stress was found to be extremely high.

5.2 Materials and Experimental Procedure

A 150 nm thick NiTi film was synthesized by co-deposition of Ti and Ni on a 4" diameter, 200 μm thick, (100)-oriented silicon wafer by DC Magnetron Sputtering at a base pressure of 5×10^{-8} Torr. A 300 nm thick SiN_x layer was grown on the wafer prior to NiTi deposition using PECVD to act as a diffusion barrier. The composition of the film was controlled by varying the power on the individual sputtering guns containing 99.999% pure Ti and Ni targets. The film was amorphous in the as-deposited state. After depositing 75 nm of the film, the deposition was halted. At this stage, a 1.5 nm thick Cr seed layer was deposited on the amorphous NiTi. This seed layer was then covered by a second 75nm thick NiTi layer, thus making the total thickness of the film 150 nm. The film was then crystallized by subjecting it to annealing at 600^{o}C for 4 hours inside the sputtering chamber. Photolithography and reactive ion etching techniques described in pervious sections were then used to co-fabricate MEMS based tensile testing stages having built-in strain and force gauges along with dog-bone shaped freestanding film samples (Figure 15).

For the in situ TEM experiments, MEMS devices containing the NiTi film samples were loaded onto a Gatan™ straining TEM holder and tensile tests were carried out in a JEOL ARM 200F microscope at an accelerating voltage of 200 kV. The samples were uniaxially strained in steps of 150 nm and bright-field images were recorded using a Gatan™ Orius CCD camera. Ex-situ tensile experiments were also carried out to

measure the stress vs strain curve of these films. In these ex-situ experiments, the films were quasi-statically strained using a piezoelectric stage.

5.3 Results and Discussion

The NiTi films were found to have a mean grain size of 115 nm. The grains in the film were predominantly austenitic with a few larger grains showing martensitic needles (Figure 29a). When the films were strained in situ, a stress induced phase transformation was observed in these films at about 1% strain. Interestingly the stress for transformation was 900MPa which is significantly larger than that observed in coarse-grained NiTi (Otsuka and Ren 2005). Upon undergoing phase transformation the microstructure of the films became predominantly martensitic (Figure 29b). Bright field TEM images showed an abundance of the needle like martensitic phase. When the films were unloaded, the reverse transformation from martensite to austenite was found to occur. After the films were completely unloaded, although most of the austenite phase was recovered, there were still some grains that remained martensitic (Figure 29c).

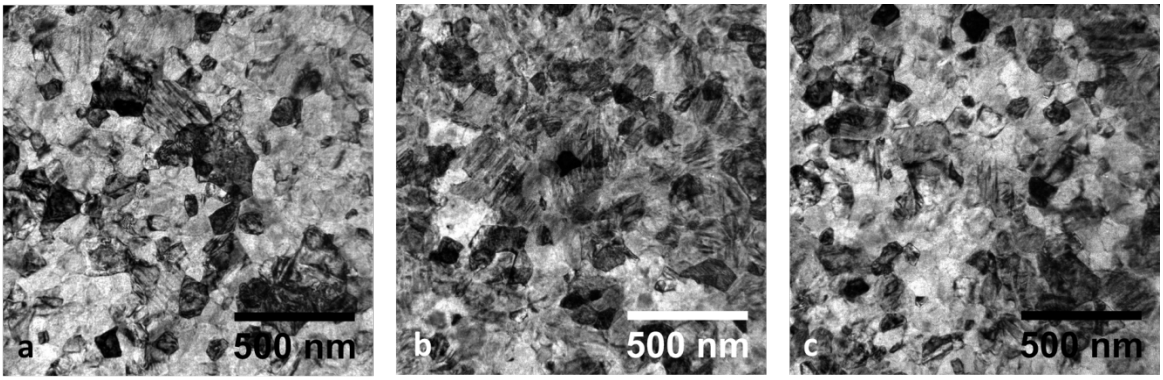

Figure 29 TEM bright field images taken during in situ straining of NiTi. Image (a) was taken prior to straining and shows predominantly austenitic grains. Image (b) corresponds to the film at a strain of 1%. A large number of martensitic grains are visible. Image (c) was taken after unloading the film. Most of the austenite is recovered upon unloading.

Ex situ tensile tests revealed that the stress induced transformation of the austenite to martensite phase leads to a drastic change in the stress vs strain curve slope (Figure 30). In coarse grained NiTi this transformation usually manifests itself as a horizontal plateau in the stress strain curve. In our samples, although the slope of the stress vs strain curve decreases drastically, it does not plateau out completely. This behavior is reminiscent of the gradual elastic-plastic transition that has been observed in other nanocrystalline metals and alloys. In other words, the stress-strain behavior of the NiTi films suggests that the phase transformation is accompanied by plastic deformation. During unloading of the films, evidence of this plastic deformation was found in the form of dislocation events (Figure 37). Thus, in the films, we have a stress induced phase transformation and dislocation mediated plasticity occurring simultaneously.

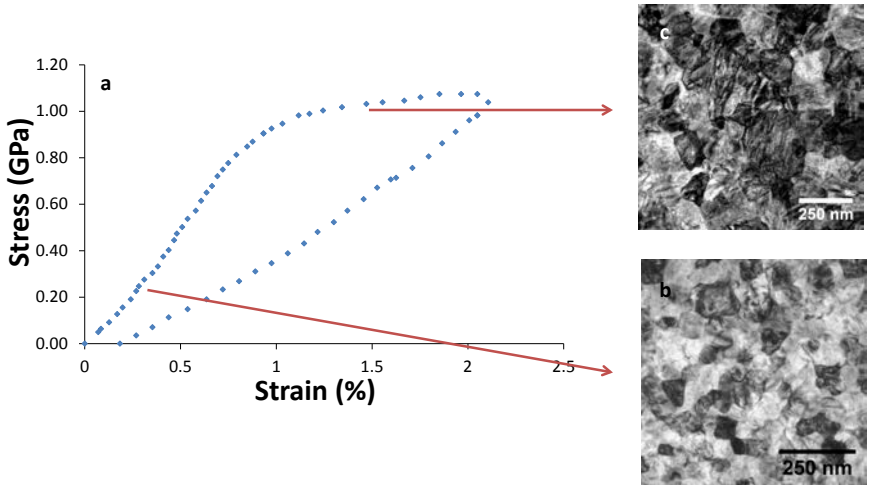

Figure 30: (a) Ex situ stress vs strain curve of NiTi. We can observe a drastic change in the slope of the curve which corresponds to the martensite transformation. We also see that the film recovers a majority of the plastic strain. (b) TEM image showing an austenitic structure prior to loading. (c) TEM image shows a majority of martensitic grains after a stress induced phase transformation.

From the stress vs strain curve we also observe that most of the inelastic strain is recovered in these thin films upon unloading. The recovery of the inelastic strain is

predominantly driven by reverse phase transformation from the martensite to the austenite phase upon unloading. However, the observation of dislocation events in certain austenite grains suggests that reverse plastic deformation is also occurring simultaneously. The plastic strain recovery in these nanocrystalline grains might be driven by an inhomogeneous distribution of stresses in the film (Rajagopalan, Han, and Saif 2007). Thus, there could be two distinct mechanisms that lead to inelastic strain recovery in these films.

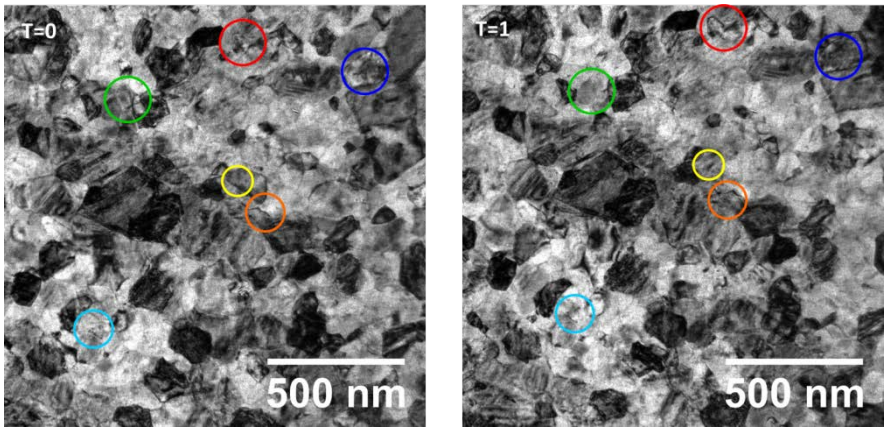

Figure 31: TEM bright field images taken during unloading of the NiTi films. Dislocation events are represented by the colored circles. These images provide evidence of plastic deformation in the austenite grains during straining

5.4 Conclusions

NiTi thin films with a stabilized austenite phase were synthesized using a seed layer mediated process. The films were subjected in situ TEM straining using MEMS devices. In situ experiments revealed stress included martensite transformations in the films. Dislocation events in the austenitic grains also suggested the presence of plastic deformation. This indicates that the films recover inelastic strain through two distinct mechanisms.

CHAPTER 6

Decoupling Elastic and Anelastic Strains in Metallic Glass Thin Films using in situ TEM Diffraction

6.1 Introduction

Metallic glasses are known to have higher strength, hardness and corrosion resistance than conventional metals and better toughness than ceramics, making them highly attractive for a variety of applications (Telford 2004; W. H. Wang, Dong, and Shek 2004; Löffler 2003). In spite of their limited ductility, metallic glasses have shown promise for structural applications due to their high elastic limit, which can extend up to 2% (Telford 2004; Ashby and Greer 2006). Nevertheless, significant efforts have been directed towards addressing this lack of ductility, which is attributed to highly localized plastic flow in shear bands (Ashby and Greer 2006). In one such study, Wang et al showed that enhanced plastic deformation in Zr based bulk metallic glasses is possible through the suppression of shear localization by using geometrical constraints (Z. T. Wang et al. 2013). Alternatively, researchers have shown that when sample dimensions are reduced to the nanoscale homogeneous flow supersedes shear band propagation as the dominant mode of deformation, resulting in enhanced ductility (Jang and Greer 2010). Furthermore, molecular dynamics (MD) simulations have revealed that metallic glass thin films can deform plastically below a critical thickness by non–localized flow (Zhong et al. 2016), providing further promise for increased ductility in these materials at the nanoscale.

In addition to enhancing the ductility, numerous studies have also focused on understanding the deformation processes in metallic glasses which are notably different from conventional metals due to the absence of long range order and defects such as dislocations and grain boundaries (Todd C. Hufnagel, Schuh, and Falk 2016; Dmowski et al. 2010; Antonaglia et al. 2014; Bruck et al. 1994; Bruck, Rosakis, and Johnson 1996; Hays, Kim, and Johnson 2000). In particular, in situ high energy X-ray and neutron diffraction techniques have been extensively used to measure micro strains in metallic glass systems (Poulsen et al. 2005; X. D. Wang et al. 2007; Mattern et al. 2009; T. C. Hufnagel, Ott, and Almer 2006). These techniques calculate the elastic micro strain tensor by measuring the relative shift of diffraction peaks in reciprocal space during straining. Such in situ deformation studies have helped to shed new light into the mechanical behavior of metallic glasses. While these studies have significantly enhanced our understanding of the deformation processes in metallic glasses, the use of X-ray or neutron diffraction has restricted the experiments to bulk, macroscopic samples. Therefore, the deformation behavior of metallic glasses at the micro and nanoscale has remained relatively unexplored.

In this study, a novel technique (Ebner et al. 2016) was used to extract the local elastic strain tensor from selected area electron diffraction (SAD) patterns during in situ TEM tensile straining of freestanding $Ti_{45}Al_{55}$ metallic glass thin films. The local atomic-level elastic strain was derived by analyzing the deformation induced anisotropic geometric changes in the first diffuse ring of the SAD patterns. The in situ TEM straining was enabled by MEMS based tensile testing stages that allow the concurrent

measurement of the macroscopic stress and strain (ε_{macro}) on the thin film samples. The in situ experiments showed that the macroscopic stress-strain response of the film was linear. However, the local elastic strain derived from the SAD patterns was consistently lower than ε_{macro}, revealing the presence of anelastic deformation. This anelasticity was independently confirmed by measuring the rate dependent stress-strain response of the film. In addition, the straining narrowed the spread of the nearest neighbor atomic distances as revealed by a reduction in the width of the SAD amorphous ring.

The results show that in situ TEM electron diffraction can be used to detect deformation induced structural rearrangements, and decouple atomic-level elastic strain from anelastic deformation in metallic glasses. A unique advantage of this technique is that elastic strain can be measured at precise locations with sub-micrometer resolution, which is not possible using X-ray or neutron diffraction. This capability, for example, could be used to measure elastic strains near crystalline regions in a partially devitrified metallic glass. These crystallites have been shown to alter the fracture morphology (Nagendra et al. 2000) and knowledge of the near-field elastic strain can aid a deeper analysis of this phenomenon. In addition to the above, loading induced microstructural changes can potentially be monitored through special imaging techniques to obtain a more comprehensive picture of the deformation processes in metallic glasses.

6.2 Materials and Experimental Procedure

A 150 nm thick TiAl (45 atomic % Ti, 55 atomic % Al) film was synthesized by co-deposition of Ti and Al on a 4” diameter, 200 μm thick, (100)-oriented silicon wafer

by DC Magnetron Sputtering at a base pressure of 5×10^{-8} Torr. The composition of the film was controlled by varying the power on the individual sputtering guns containing 99.999% pure Ti and Al targets. The film was amorphous in the as-deposited state. Rutherford backscattering spectrometry was used to determine the composition of the films and X-ray diffraction analysis confirmed the amorphous nature of the film. Photolithography and reactive ion etching techniques were then used to co-fabricate MEMS based tensile testing stages having built-in strain and force gauges along with dog-bone shaped freestanding film samples (Figure 15).

For the in situ TEM experiments, MEMS devices containing the $Ti_{45}Al_{55}$ film samples were loaded onto a Philips™ straining TEM holder and tensile tests were carried out in a Philips CM200 TEM at an accelerating voltage of 200 kV. The samples were uniaxially strained in steps of 150 nm and bright-field images and SAD patterns were recorded using a Gatan™ Orius CCD camera after allowing the film to relax for 5 minutes. The averaged strain rate over the duration of the experiments was ~ 10^{-6}/s, essentially resulting in quasi-static loading.

SAD patterns were taken from a circular area of diameter 1.2 μm with an exposure time of 10 s. Before each SAD pattern was acquired, a normalization procedure was performed to reduce the magnetic remanence of the lenses so that the variation of the camera length in different SAD patterns was minimized. The illumination condition of the TEM was also kept constant during the experiment. To ensure that the electron beam did not cause any stress relaxation or anomalous changes in sample geometry (Sarkar,

Rentenberger, and Rajagopalan 2015) one of the samples was continuously exposed to the electron beam for 60 minutes and the stress, ε_{macro} and atomic-level elastic strain were recorded before and after exposure. No noticeable difference was seen in the any of these quantities.

Three $Ti_{45}Al_{55}$ film samples were tested in situ in the TEM. The first sample was loaded up to ε_{macro} = 0.6%, while the second and third samples were loaded until failure. The second sample was loaded and unloaded once before it was strained to failure whereas the first and third samples were subjected to a single loading. In addition, ex situ uniaxial tensile load-unload experiments were performed at different strain rates (10^{-6}/s to 10^{-2}/s) on two samples. A piezoelectric actuator (Physik Instrumente) was used to load the MEMS devices and a CMOS camera (Thor Labs) was used to acquire images of the gauges during the experiments. A more detailed description of the procedure adopted for these strain rate experiments is provided in (Izadi and Rajagopalan 2016).

The macroscopic stress and strain on the samples were measured using the built-in gauges of the MEMS stage. A custom MATLAB™ program, which tracks prescribed features across a series of images using cross-correlation techniques, was used to measure the displacement of the gauges and thus the sample stress and strain. The macroscopic stress and strain resolutions were 2 MPa and 0.005%, respectively, for the in situ TEM experiments and 5 MPa and 0.01%, respectively, for the ex situ strain rate experiments. A script (Ebner et al. 2016) written on the GATAN™ Digital-Micrograph platform was used to analyze the SAD patterns and extract the 2D strain tensor and the principal strain

along the longitudinal (e_{11}) and transverse direction (e_{22}). The script measures the ellipticity introduced in the SAD ring by the applied strain to extract the elastic strain (Figures 32b, c). Since these elastic strains correspond to the strain on an atomic level, they are denoted as atomic-level elastic strains to distinguish them from the macroscopic strain (ε_{macro}) in the entire sample. The atomic-level elastic strain can be quantified on a micrometer scale using this technique with an accuracy and precision of 10^{-4} and 2×10^{-4}, respectively.

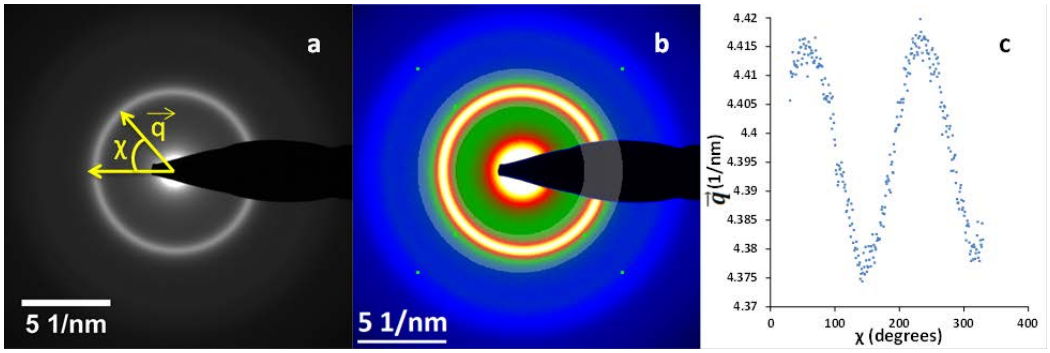

Figure 32: Evolution of the ellipticity of SAD pattern with strain: (a) SAD pattern of the amorphous film where $\vec{q}$ corresponds to the reciprocal lattice vector of the first ring and χ is the azimuthal angle. (b) An ellipse being fitted to the SAD pattern of the strained film using a script written on the Digital Micrograph platform to extract the atomic-level elastic strain. (c) A plot of the reciprocal lattice vector ($\vec{q}$) corresponding to the maxima positions of the SAD ring shows the peaks and valleys appearing at different azimuthal angles (χ) due to the ellipticity introduced by straining.

6.3 Results and Discussion

TEM bright-field images of the film showed contrast that is characteristic of a metallic glass, containing no crystalline phases (Fig. 33a). It should be pointed out that the dark features present in the bright-field images are photoresist residues left from sample fabrication. The amorphous structure of the thin film was confirmed by the SAD pattern containing broad diffuse rings (Fig. 32a) as well as X-ray diffraction. RBS

measurements revealed the composition of the film to be 45 atomic % Ti and 55 atomic % Al.

Sample	E using ε_{macro} (GPa)	E using e_{11} (GPa)	$\mu\ (-\frac{e_{22}}{\quad})$
1	154	169	0.195
2	152	176	0.245
3	158	173	0.21

Table 1: Elastic Modulus (E) for in situ TEM straining experiments calculated using ε_{macro} and e_{11}. For sample 2, the values reflect the average of two cycles.

The in situ TEM tensile experiments revealed an absence of plasticity (Figure 34) with all three films exhibiting a linear macroscopic stress-strain behavior up to the maximum strain/failure. The failure occurred in a catastrophic manner due to localized deformation in a shear band (Figure 33b). Contrary to previous reports (H. Chen et al. 1994), bright field, dark field and SAD images of the TiAl fracture surface did not indicate the formation of nanocrystals by the localized deformation. From the morphology of the fracture surface shown under dark-field condition in Figure 33b, small deflections of the catastrophic shear band propagating at a mean inclination angle of 60° with respect to the thin film surface can be revealed.

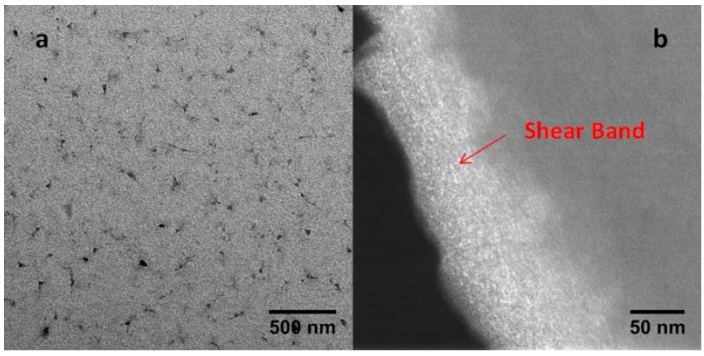

Figure 33: Microstructure of TiAl film: (a) TEM bright field image of the $Ti_{45}Al_{55}$ film before straining, indicative of a typical amorphous microstructure. (b) TEM dark field image of the fractured edge of the third sample. The brightness gradient in the image points to shear banding as the mode of failure.

The calculated longitudinal principal strain e_{11} correlated well with ε_{macro} in all three samples but it was on average about 10% smaller, leading to a similar difference in the calculated Young's modulus (E). Specifically, E calculated using the applied stress and ε_{macro} was found to be 155±3 GPa, which is lower than the E of bulk crystalline γ TiAl (175-188 GPa) (He et al. 1995). This lower E is consistent with the presence of anelastic deformation that is common in many metallic glasses (H. S. Chen, Krause, and Coleman 1975). The Young's modulus computed using the longitudinal atomic-level elastic strain (e_{11}) values, in contrast, was found to be 173±3 GPa, almost identical to that of crystalline TiAl.

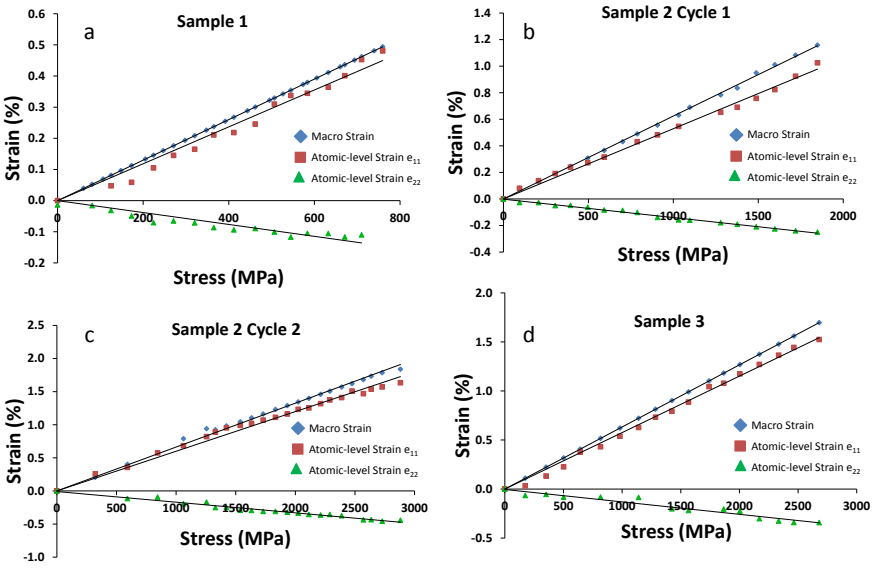

Figure 34: Macroscopic and atomic-level elastic strain versus stress: (a) The macroscopic and atomic-level elastic strains versus stress plot for the first TiAl sample. (b) Strain versus stress plot for the 1st cycle of the second sample. The sample was unloaded before failure. (c) Strain versus stress plot of the second sample for the 2nd cycle, where it was loaded until failure. (d) Strain versus stress plot of the third sample, which was loaded until failure. In all the plots, the black lines represent the lines of best fit whereas the symbols represent raw data points.

The Poisson's ratio (μ) calculated from the linear fit of the variation of e_{22} and e_{11} from all three samples was found to be 0.215±0.02, in good agreement with the results

from other metallic glass systems containing Ti and Al (Telford 2004). The E and μ obtained from each in situ TEM experiment is listed in Table 1. The Poisson's ratio was also independently calculated from in situ scanning electron microscopy (SEM) tensile experiments. In the in situ SEM experiments, the distances between markers (photoresist residue left from fabrication) along the longitudinal and transverse directions of a sample were tracked as a function of applied strain (Figure 35). By measuring the change in the transverse strain as a function of the longitudinal strain a Poisson's ratio of 0.23±0.035 was obtained, which is consistent with the in situ TEM measurements.

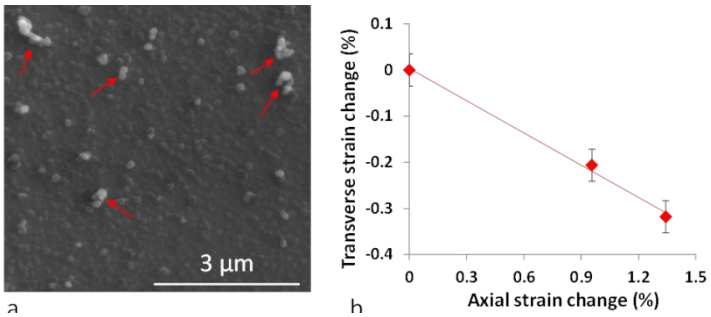

Figure 35: In situ SEM straining experiments: (a) SEM image of a TiAl sample with some of the residual photoresist markers from sample fabrication indicated by red arrows. (b) Change in transverse strain as a function of axial strain for the sample. The slope of the red line is ~ 0.235, which corresponds to the Poisson's ratio of the sample

The full width at half maximum (FWHM) of the first diffraction ring (Figure 36) was also calculated along all directions for the samples. The FWHM measurements were then averaged and normalized by the mean of the major and minor semi-axis of the elliptic diffraction ring. The normalization was done to mitigate any effect from potential perturbations of the TEM camera length. These normalized FWHM values, which correspond to the spread of the first nearest neighbor atomic distances, for sample 2 is shown Figure 36c. The FWHM values decreased linearly with increasing stress in both

cycles but saturated at high stresses in the second one (Figure 36c). Interestingly, the FWHM versus stress curves for the two cycles do not overlap as the FWHM increased after unloading. The same trend of decreasing FWHM with increasing stress was obtained when only the longitudinal and transverse directions were considered.

As mentioned previously, there was significant difference between the longitudinal elastic strain and macroscopic strain in the in situ TEM experiments. To explore the cause of this discrepancy, ex situ tensile load-unload experiments at different strain rates (10^{-6}/s - 10^{-2}/s) were conducted on two samples. The strain rates were chosen such that the lowest strain rate was roughly similar to the averaged strain rate during the in situ TEM experiments.

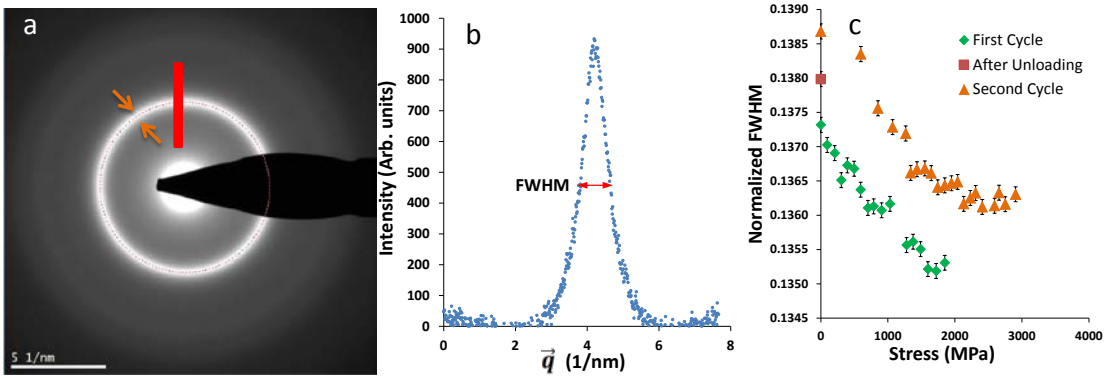

Figure 36: FWHM measurements on metallic glass TiAl films: (a) A typical SAD pattern analyzed during the loading of Sample 2. The orange arrows indicate the width of the 1st amorphous ring, which corresponds to the spread in the first nearest neighbor atomic distances. The red line corresponds to the intensity curve in (b). (b) The background subtracted intensity plot corresponding to the red line in (a). The FWHM of the peak was found to change with loading. (c) The normalized FWHM values of the first diffraction ring of the second sample during the two loading cycles. The FWHM values decrease with increasing stress, indicating a drop in the spread of nearest neighbor distances and an increase in short range order. The change in cycle 1 appears to be temporary as the initial FWHM value for the 2nd cycle is higher.

The experiments showed that the stress-strain response was linear during both loading and unloading at all rates. There was also no residual strain after unloading in any

of the experiments, confirming the lack of plastic deformation. However, the measurements revealed a rate dependence of E (Figure 37), which increased from 156±1 GPa at the lowest strain rate to 166±1 GPa (6-7% increase) at the highest strain rate (10^{-2}/s). Thus, for a given stress the measured ε_{macro} at the highest rates was about 6-7% smaller than the strain at the lowest rate.

The in situ TEM experiments of the TiAl thin films revealed failure stresses between 2.7-2.9 GPa and macroscopic failure strains between 1.7-1.9%. By tracking the geometric changes in the SAD patterns, we were able to measure the atomic-level elastic strain tensor, which showed that the longitudinal elastic strain (e_{11}) was consistently smaller by about 10% compared to ε_{macro}. No discernable plasticity was seen in any of the samples and failure occurred by shear localization (Schuh, Hufnagel, and Ramamurty 2007). Nevertheless, an analysis of the atomic scale response and comparison of the macroscopic strain and atomic-level elastic strain reveals several interesting details about the deformation induced structural changes in the metallic glass film.

First, we consider the discrepancy between ε_{macro} and e_{11} in the amorphous TiAl film. The change in the geometry of the SAD patterns, from which e_{11} is obtained, is sensitive only to elastic strain. In the in situ TEM experiments, ε_{macro} was about 10% larger than e_{11}. The strain rate experiments (Figure 37) show that ε_{macro} at the lowest rate is 6-7% higher than ε_{macro} at the highest rate for a given stress. In effect, at least 6-7% of ε_{macro} is due to anelastic deformation at rates (~10^{-6}/s) comparable to those applied in the

in-situ TEM experiments. Thus, a major part of the observed difference between ε_{macro} and e_{11} in the in situ TEM experiments can be accounted for by anelasticity.

Furthermore, it has been shown that in metallic glasses atomic-level elastic strain in the nearest neighbor shells can be smaller than distant atomic shells (T. C. Hufnagel, Ott, and Almer 2006). Since the geometric changes in the first diffraction ring correspond to the nearest neighbor shell, it is possible that the calculated e_{11} underestimates the elastic strain in the film. This could, in principle explain why anelasticity does not fully account for the difference between ε_{macro} and e_{11}.

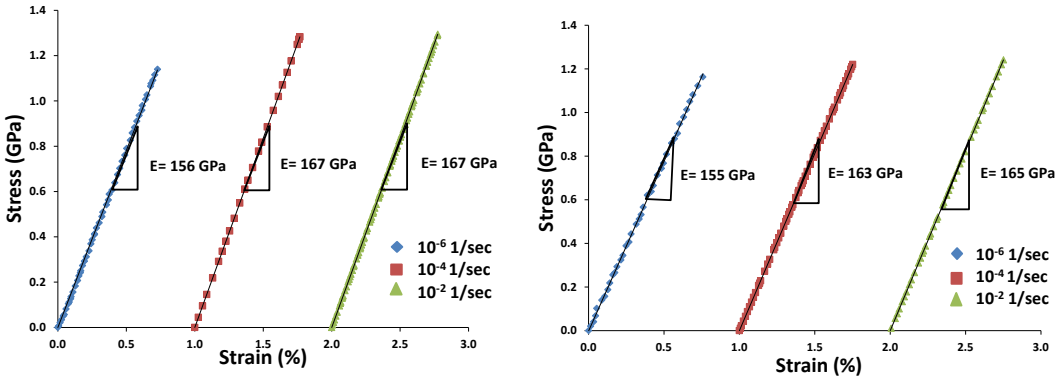

Figure 37: Strain rate dependent Young's modulus of TiAl films: (a, b) Stress-strain response of two TiAl thin film samples subjected to ex-situ straining at 3 different strain rates. The E obtained at the highest strain rate is about 7 % greater than the E obtained from the lowest rate. The strain values for the experiments carried out at 10^{-4}/s and 10^{-2}/s have been offset by 1 and 2 % strains respectively.

In this context, it is worth noting that even in previous in situ XRD deformation studies on metallic glasses, *E* calculated using atomic-level elastic strain was about 5-6% greater than the value obtained using macroscopic strain (Mattern et al. 2009; T. C. Hufnagel, Ott, and Almer 2006). The results obtained in this study suggest that those differences might have been a result of anelasticity. Anelastic deformation in metallic glasses is often attributed to the presence of atomic free volume zones (J. C. Ye et al.

2010), the extent of which depends on the processing conditions and the thermal/mechanical history. Metallic glass thin films that are synthesized by sputtering are known to have a larger fraction of free volume zones (Chang et al. 2014) and this could be the reason for the higher anelastic strain observed in our samples.

From a microscopic viewpoint, anelasticity can be seen as a manifestation of deformation-induced structural rearrangements (Tong et al. 2015) and MD simulations have found correlations between the short-range order of atomic clusters and the extent of their anelastic deformation (Ding, Cheng, and Ma 2012). The FWHM measurements in this study support such an atomic scale interpretation of anelasticity. As shown in Figure 36c, the normalized FWHM values of the amorphous ring decrease with increasing stress, which suggests a change in short-range order (narrower spread of first nearest neighbor distances). More importantly, the results indicate that these structural rearrangements start to occur from the initial stages of deformation, which is consistent with the presence of anelastic deformation even at low stresses/strains. The saturation of the FWHM values at very high stresses (> 2 GPa), however, does indicate that the structural rearrangements become progressively harder as the sample approaches catastrophic failure though the formation of shear bands. It is also worth noting that upon unloading after the first cycle, the normalized FWHM increased to a higher value (Figure 36c). This suggests that even in the absence of plasticity, the deformation resulted in a permanent change in the amorphous structure of the film.

In addition to anelasticity, the elastic properties (E and μ) obtained from the in situ TEM experiments also provide some insights into the atomic-scale response.

Notably, the macroscopic E (155±3 GPa) of the metallic glass TiAl film is lower than the E of crystalline TiAl (175-188 GPa) due to the presence of anelastic deformation. However, the E (173±3 GPa) obtained from the atomic-level longitudinal elastic strain (e_{11}) is nearly identical to that of crystalline TiAl. This suggests that the atomic-level stiffness of metallic bonds in amorphous TiAl is very similar to that of crystalline TiAl. Similarly, the relatively low Poisson's ratio (μ = 0.215±0.02) of the TiAl metallic glass film is also consistent with small failure strains (~2%). Previous studies have shown that μ < 0.3 in metallic glass systems leads to a brittle failure (Lewandowski, Wang, and Greer 2005) and the lack of plasticity in our samples supports this conclusion.

6.4 Conclusions

To summarize, most prevalent techniques for calculating atomic-level strains in metallic glasses employ high energy X-ray or neutron diffraction. Here, it is shown that TEM electron diffraction can also be used to accurately calculate atomic-level elastic strains in metallic glass films. This technique has the advantage of measuring atomic-level elastic strains from localized regions (< 1 μm^2) while also allowing us to monitor changes in microstructure using special TEM imaging methods, which is not possible in X-ray or neutron diffraction. This capability, for example, could be used to study the origins of plastic flow in thin (< 100 nm) metallic glass films (Guo et al. 2007) or quantitatively analyze the elastic strain near crystalline inclusions. More importantly, the method allows us to detect mechanically induced structural rearrangements, and decouple atomic-level elastic strain from larger scale anelastic deformations without the need for experiments at multiple strain rates or frequencies.

CHAPTER 7

Electron Beam Inducted Artifacts During in situ TEM Deformation of Nc and Ufg Aluminum

7.1 Introduction

A critical assumption underlying in situ transmission electron microscopy studies is that the electron beam (e-beam) exposure does not fundamentally alter the intrinsic deformation behavior of the materials being probed. In this research it was found that e-beam exposure caused increased defect activation and marked stress relaxation in aluminum films spanning a range of thicknesses (225-400 nanometers) and grain sizes (125-220 nanometers). Furthermore, the e-beam induced anomalous sample necking, which unusually depends on beam diameter rather than intensity. Notably, the stress relaxation in aluminum occurred at beam energies well below the damage thresholds. More remarkably, the stress relaxation and/or sample necking is significantly more pronounced at lower accelerating voltages (120 kV versus 200 kV). These observations in aluminum were added to experiments done on gold in which similar results were seen. Thus the beam induced artifacts observed in two metals with highly dissimilar atomic weights and properties indicate that e-beam exposure can cause anomalous behavior in a broad spectrum of nanostructured materials, and simultaneously suggest a strategy to minimize such artifacts.

7.2 Materials and Experimental Procedure

Two Al films, 225 nm and 400 nm thick, respectively were deposited on 200-μm thick, 100 mm diameter, (100) silicon (Si) wafers using DC magnetron sputtering. Before deposition, the Si wafers were etched with hydrofluoric acid to remove the native silicon dioxide layer. Experiments had also been previously carried out on 80 nm thick Au films by Dr. Rajagopalan and Dr. Rentenberger. The 225 nm thick Al film (from here on referred to as Al-225 film) and the Au film were deposited immediately after the removal of the silicon dioxide layer at base pressures of $1.5x10^{-8}$ Torr and $5x10^{-8}$ Torr respectively. The 400 nm thick Al film (from here on referred to as Al-400 film) film was deposited at a base pressure of $1.5x10^{-7}$ Torr about 1.5 hours after the removal of the oxide layer. For all depositions, the argon pressure was 3 mTorr and the deposition rate was between 4-5 nm/minute. Dog-bone shaped freestanding samples of the two films were then co-fabricated with micro-electro-mechanical systems (MEMS) based tensile testing devices described earlier (Figure 15) using photolithography and plasma etching techniques.

The MEMS devices with the freestanding film samples were mounted on a displacement controlled single tilt, straining holder and the films were subjected to cyclic deformation inside a Philips CM200 TEM equipped with a LaB_6 cathode. In each of the straining cycles the beam condition was systematically controlled as follows. The beam intensity was varied for a given exposed area by changing the e-beam current. The beam current was controlled by altering the Wehnelt bias, the filament heating current of the TEM and the size of the condenser aperture. In all the experiments, the microstructure

was observed under TEM bright field conditions and recorded using an Orius Gatan™ CCD camera.

Strain pulses (typically corresponding to < 0.1% strain) were applied to the sample, following which the sample was allowed to relax for a period of 5 minutes and the stress-strain data was then recorded. Two types of experiments were performed to quantify the effect of e-beam exposure. In the first set of experiments, the stress-strain response of the Al-225, Al-400 and Au film during the first cycle was measured without e-beam exposure to serve as a reference. In the subsequent cycles, the films were exposed to the e-beam at different accelerating voltages and the beam diameter (area) and intensity were systematically varied. In the second set of experiments on the Al-225 film, the sample was exposed to the e-beam only at two points during each loading to quantify beam-induced stress relaxation. At both these points, stress-strain data was recorded for a period of 15 minutes, typically at 5-minute intervals. Table 2 and 3 show the beam conditions for all the experiments.

The stress-strain response of the films was obtained by analyzing images of the built-in force and displacement gauges during deformation, using a custom MATLAB™ program. The program tracks prescribed features using cross-correlation techniques across a series of images to calculate the displacement of the gauges. Using this process, stress and strain resolutions better than 2 MPa and 0.005%, respectively, were obtained for both Al and Au films.

Al 225	**Cycle**	**Voltage (kV)**	**Area (μm^2)**	**Current (nA)**	**Intensity (A/cm^2)**	**$\sigma_{1\%}$ (MPa)**
	1	0	0	0	0	380
	2	80	12.5	44	0.352	358
	3	120	201	103	0.051	362
	4	200	201	61	0.03	408
	5	200	804	61	0.007	419
	6	120	804	103	0.012	445
Al-400	**Cycle**	**Voltage (kV)**	**Area (μm^2)**	**Current (nA)**	**Intensity (A/cm^2)**	**$\sigma_{0.75\%}$ (MPa)**
	1	0	0	0	0	120
	2	120	201	14	0.0069	109
	3	200	201	10	0.0049	167
Au-80	**Cycle**	**Voltage (kV)**	**Area (μm^2)**	**Current (nA)**	**Intensity (A/cm^2)**	**$\sigma_{1\%}$ (MPa)**
	1	0	0	0	0	452
	2	120	7	95	1.357	369
	3	200	7	95	1.357	464

Table 2: Beam condition and the corresponding stress response of the Al-225, Al-400 and Au-80 samples during cyclic deformation.

Cycle	Voltage (kV)	Area (μm^2)	Current (nA)	Intensity (A/cm^2)	1^{st} Stress Drop (%)	2^{nd} Stress Drop (%)
1	120	201	71	0.035	8.06	7.79
2	200	201	71	0.035	2.88	6.24
3	120	804	61	0.0075	7.37	10.63
4	200	804	66	0.0082	4.32	7.79

Table 3: Beam condition and the corresponding stress response of the Al-225 sample during relaxation experiments

Once the raw stress-strain data was obtained, the data was fitted with polynomial functions to obtain the stress at a given strain. To avoid over fitting, for both loading and unloading the polynomial order was chosen so that there were at least three data points for each coefficient. Typically, fourth order polynomials were used to fit the stress-strain

data for loading and third order polynomials were used for unloading. For stress-relaxation, for which only four or fewer data points were measured, a linear fit was chosen. The R^2 value was higher than 0.995 for all the loading and unloading fits, except for the second loading of the Au film (R^2 = 0.993). Similarly, the R^2 value for fits to the Al-225 stress relaxation data exceeded 0.98 except for the 1st stress drop in cycle 2 (R^2 = 0.804), when the relaxation was very small (Table 3). The equations of the fitted curves were then used to extract the stress at 1% strain ($\sigma_{1\%}$) for the Al-225 and Au films, the stress at 0.75% strain ($\sigma_{0.75\%}$) for the Al-400 film and the stress drop for relaxation experiments on the Al-225 film. $\sigma_{1\%}$ and $\sigma_{0.75\%}$ were calculated for a particular cycle after offsetting the stress-strain curve to account for residual plastic strain from previous cycles. To ensure robustness of the fits, $\sigma_{1\%}$ and $\sigma_{0.75\%}$ were also calculated by fitting higher order and lower order polynomials and the values compared. No meaningful changes in the stress values were observed.

7.3 Results and Discussion

The microstructure of the films was characterized by TEM and x-ray diffraction (XRD). The analyses (Figure 38A, B) revealed a *d* of 120 nm and a nearly bicrystalline microstructure for the Al-225 film. The Al-400 film had a higher *d* of 220 nm and a mild (110) out-of-plane texture with random in-plane grain orientations (Figure 38C, D), whereas the Au film had a *d* of 50 nm and a strong (111) out-of-plane texture with random in-plane grain orientations (Figures 38E, F)**.**

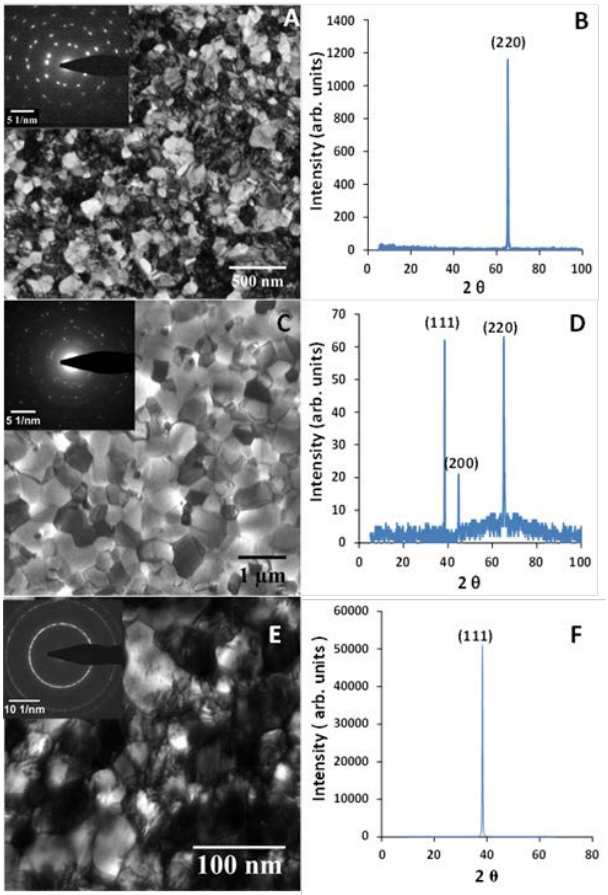

Figure 38: Microstructure of Al and Au Films: (A) Bright-field TEM image of the undeformed Al-225 film (d = 120 nm). Selected area diffraction (SAD) of the film showing an (110) out of plane texture with two in-plane variants rotated 90^0 with respect to each other (inset). (B) XRD scan of the Al-225 film showing a single (220) peak. (C) Bright-field TEM image of the undeformed Al-400 film (d = 220 nm). SAD of the film showing a mild (110) out of plane texture and random in-plane texture (inset). (D) XRD scan of the Al-400 film. The (111) and (220) peaks have similar intensities, whereas in random polycrystalline Al their ratio is 10:3, which shows a mild (110) texture in the film. (E) Bright-field TEM image of the undeformed Au-80 film (d = 50 nm). SAD of the film showing a (111) out of plane texture with random in-plane texture (inset). (F) XRD scan of the Au-80 film showing a single (111) peak.

Figure 39 shows the stress-strain response of the films for the cyclic loading and stress relaxation experiments under different beam conditions. To quantify the e-beam effect on the stress-strain response during the cyclic loading experiments, the stress at the same strain level during each cycle are compared, after offsetting the stress-strain curve to account for residual plastic strain from previous cycles. For the Al-225 and Au film,

$\sigma_{1\%}$ is used for comparison. The overall trend is very similar even if the stress at a lower strain level is used for comparison. The Al-400 film started deforming plastically at lower strain and hence was subjected to smaller strains during each cycle. Therefore, we compare the $\sigma_{0.75\%}$ during each cycle. $\sigma_{1\%}$ for the Al-225 and Au film and $\sigma_{0.75\%}$ for the Al-400 film during each cycle is summarized in Table 2.

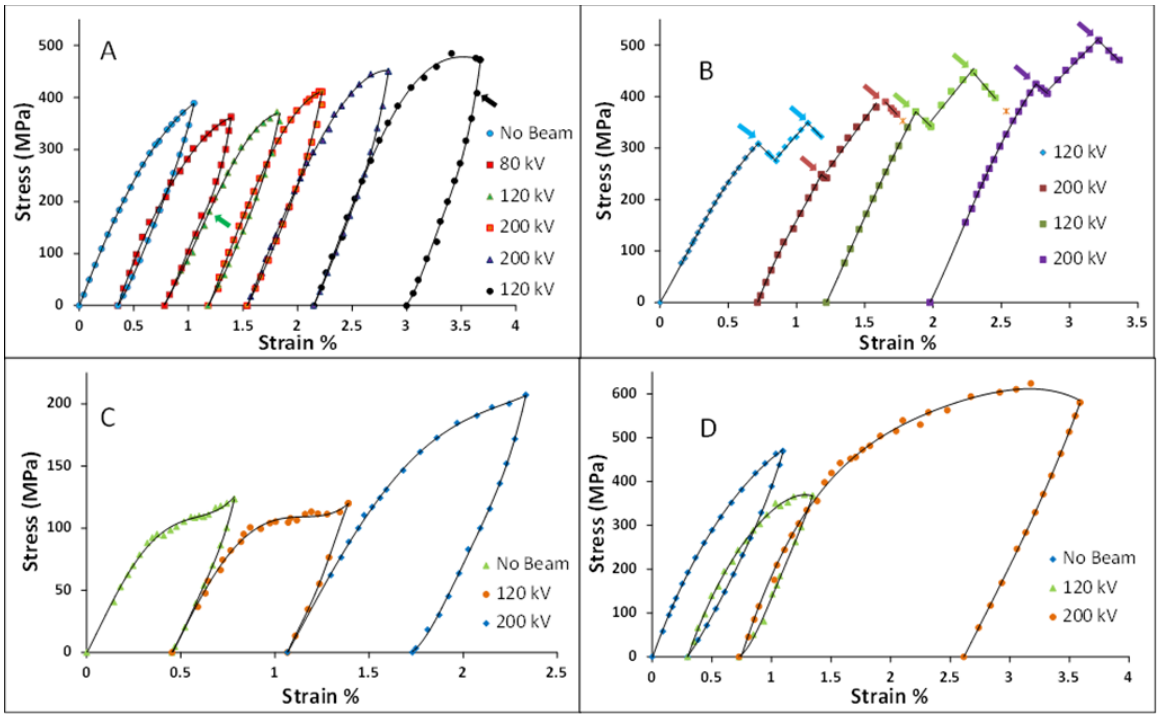

Figure 39 Cyclic Stress-Strain Response and Stress Relaxation of Al and Au films: (A): Stress-strain response of Al-225 film over six cycles under different beam conditions. A relaxation in stress can be observed for the 2nd and 3rd cycle with respect to the 1st cycle when an 80 kV and 120 kV e-beam were incident on the film, respectively. The imaging conditions for the different deformation cycles are summarized in Table 2. The green and black arrows correspond to Figure 40 and supplementary video 2, respectively. (B): Beam induced stress relaxation in the Al-225 film. The film was exposed to the e-beam only at two points during each loading (indicated by arrows) and stress-strain data was recorded over a period of 15 minutes. Stress relaxation was substantially higher at 120 kV compared to 200 kV. At the end of the 2nd and 3rd cycles, the e-beam was moved to a new location, which led to significant additional relaxation (indicated by the orange cross). (C): Stress-strain response of the Al-400 film over three cycles with different beam conditions. (D) Stress-strain response of the Au film over three cycles with different beam conditions. In all the figures the solid black lines corresponds to the fitted curves while the individual points correspond to the raw data.

As evident from Figure 39A as well as the tabulated values in Table 2, $\sigma_{1\%}$ for the Al-225 film decreased from 380 MPa in the 1st cycle (no e-beam exposure) to 358 MPa and 362 MPa, respectively, in the 2nd (80 kV) and 3rd cycle (120 kV). In cyclic loading of metal films, the stress for a given strain usually increases in subsequent cycles due to strain hardening. In contrast, $\sigma_{1\%}$ during the 2nd cycle decreased by 5.7% with respect to the 1st cycle and was still lower by nearly 4.7% during the 3rd cycle, clearly indicating the effect of e-beam exposure. However, when the accelerating voltage was increased to 200 kV in the 4th cycle, $\sigma_{1\%}$ was significantly higher (408 MPa), a 7.4% increase over the 1st cycle and a 12.7% increase over the 3rd cycle.

To study the effect of beam intensity, the accelerating voltage and beam current (area times intensity) were kept constant, while intensity was reduced 4-fold between the 4th and 5th cycles. This resulted in an increase of $\sigma_{1\%}$ to 419 MPa from 408 MPa. To confirm this trend, the accelerating voltage (120 kV) and beam current for the 6th cycle were made identical to the 3rd cycle but the intensity was again decreased 4-fold. $\sigma_{1\%}$ during the 6th cycle (445 MPa) was nearly 23% higher than the 3rd cycle. The cyclic stress-strain data in Figure 39A strongly suggested that beam-induced stress relaxation is higher at 120 kV compared to 200 kV. To unambiguously verify this behavior, stress relaxation experiments were performed on the same film (Figure 39B) at 120 kV and 200 kV. As evident from the data (Table 3), stress relaxation was significantly higher at 120 kV, even though the intensity was identical or even larger at 200 kV (compare Cycle 4 with Cycle 3).

To ensure that the larger stress relaxation observed at lower accelerating voltages is not unique to a particular grain size, specimen thickness or material, the cyclic load-unload experiments were repeated on an Al film (Al-400) with a larger thickness and grain size and an Au film with much smaller thickness and grain size. The stress-strain response of the Al-400 and Au film (Figures 39C, 39D), were consistent with the behavior of the Al-225 film, showing significantly higher stress relaxation at 120 kV compared to 200 kV.

In addition to the stress-strain response, the evolution of the microstructure during and after deformation was also monitored. The Al-225 film showed a small increase in *d* from 120 nm to 135 nm after deformation. In contrast, the Al-400 and Au film did not show any grain growth. In all the films dislocation activity was seen even at small strains where the stress-strain curve showed little deviation from linearity. Figure 40 shows an example of such dislocation activity in the Al-225 film during the third deformation cycle when the strain was ~0.41% (indicated by the green arrow in Figure 39A). The video corresponding to these images (videoS1) is available as supplementary material. Notably, significant dislocation activity was also seen during the initial stages of unloading (videoS2), when the macroscopic stress-strain response was elastic. The stress corresponding to videoS2 is about 408 MPa (indicated by the black arrow in Figure 39A), 76 MPa lower than the peak stress during the cycle. These observations suggested that dislocations are activated by e-beam exposure, leading to localized plastic deformation.

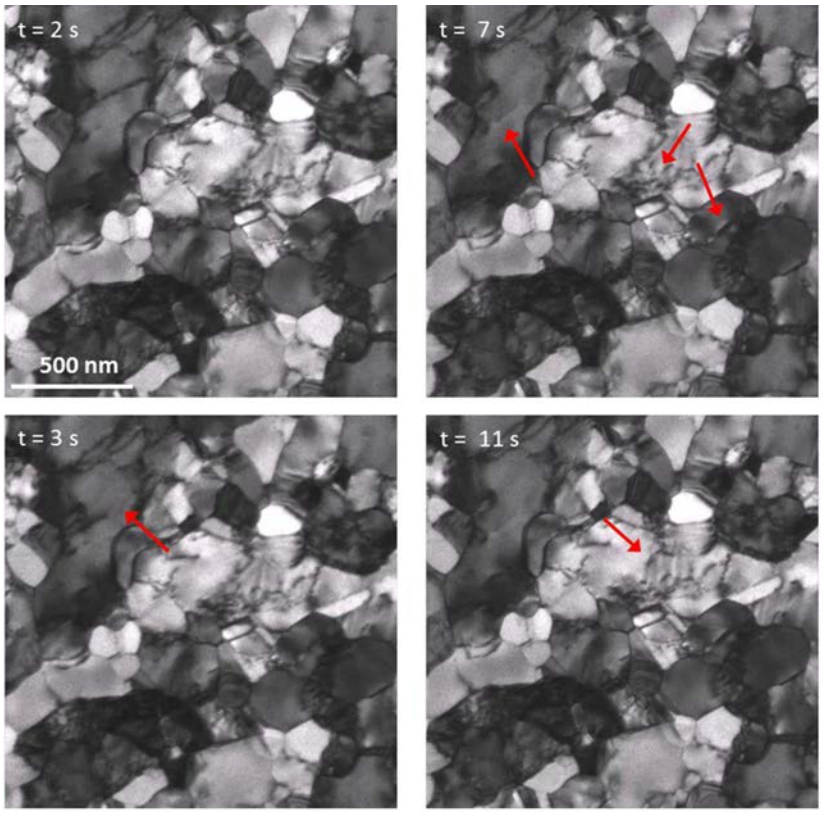

Figure 40: Dislocation Motion During Straining: TEM bright-field images of the Al-225 film after the application of a set of displacement pulses during the 3rd cycle. The approximate stress and strain at this point was 225 MPa and 0.41%, respectively (green arrow in Figure 39A). The red arrows point to locations of dislocation activity. The video corresponding to these images (video S1) is available as supplementary material.

To confirm this, during the stress relaxation experiments on the Al-225 film (Figure 39B) the e-beam was shifted to a different area of the sample at the end of 2nd loading cycle for approximately 2 minutes. Immediately upon e-beam exposure, substantial dislocation activity (videoS3) was observed in the new area, which was accompanied by further stress relaxation (orange cross at the end of 2nd cycle). Note that this additional stress relaxation occurred even though the sample had been exposed to the e-beam for 15 minutes in the previous observational area and significant stress relaxation (> 6%) had already occurred. We similarly shifted the beam to a new location at the end

of the 3rd cycle and again observed significant additional relaxation (orange cross at the end of 3rd cycle).

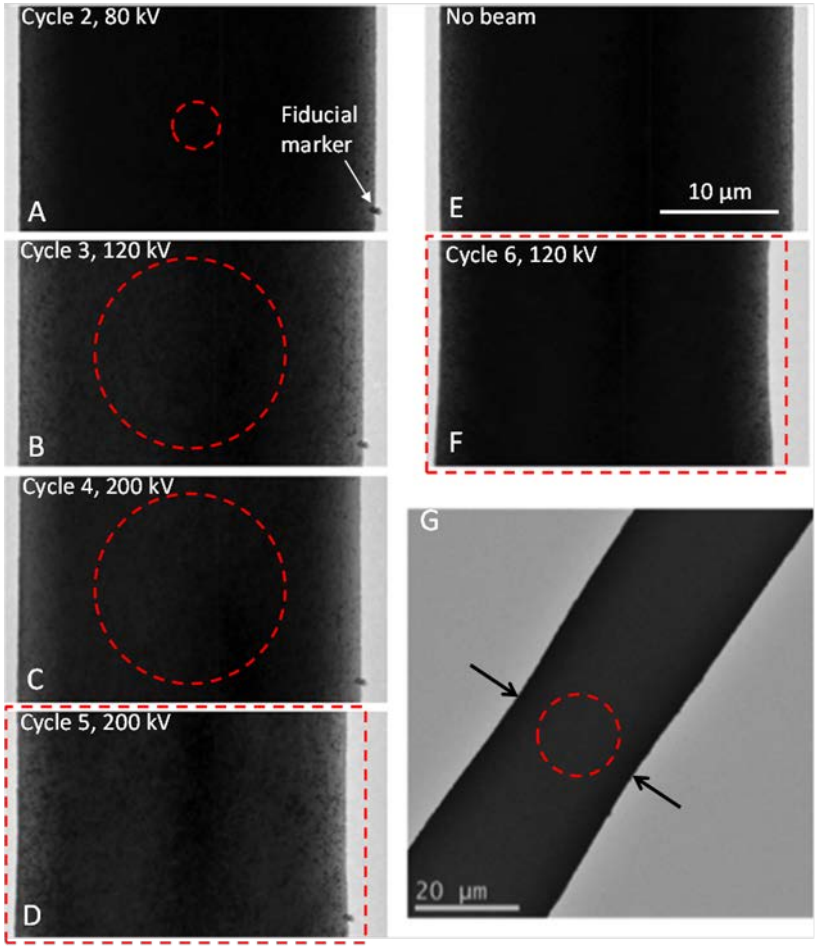

Figure 41: Anomalous Necking of Films: (A-F) TEM images of the Al-225 sample at the locations where it was exposed to the e-beam, with scale bar shown in (E). The left edge of the sample is aligned so that changes in width after each cycle can be easily seen. The red circles in (A-C) are the area exposed to the e-beam. In (D) and (F), the entire width of the sample was exposed, as indicated by the red rectangles. The center of the e-beam was at the same location from the 2nd cycle to 5th cycle. The imaging area was changed during the 6th cycle; (E) and (F) correspond to the new area before and after the 6th cycle. The necking of the sample is clearly visible in (D) and (F). (G) TEM image of the 400 nm sample after the 2nd cycle, with the arrows pointing to the necked region.

Apart from microstructural changes, significant necking along the sample width was seen in the Al-225 film (Fig. 41). This localized necking exactly corresponded to the location of the e-beam on the sample (indicated by a red circle or rectangle), which

strongly suggests that the necking is a direct consequence of e-beam exposure. In the Al-225 film, the width reduced from 30 μm to 27.54 μm, an 8.2% reduction, after 5 deformation cycles. To understand the effect of beam conditions on necking, the changes in sample width (Δw) from the 2nd to 5th cycle was analyzed. Since the initial sample width (at the beam location) was different for each cycle, the percentage width reduction ($\Delta w/w$) is calculated for each cycle. Then $\Delta w/w$ was normalized by the plastic strain (ε_p) imposed in that cycle. After this normalization, a clear dependence of necking on both the beam area as well as accelerating voltage was found (Table 4).

Cycle	Voltage (kV)	Area (μm2)	Intensity (A/cm2)	Plastic strain (%)	Initial width (μm)	Final width (μm)	%WR	%WR/ Plastic strain
1	0	0	0	0.355	30	30	0.00	0.00
2	80	12.5	0.352	0.426	30	30	0.00	0.00
3	120	201	0.051	0.399	30	29	3.33	8.35
4	200	201	0.03	0.357	29	28.66	1.17	3.28
5	200	804	0.007	0.606	28.66	27.54	3.91	6.45
6	120	804	0.012	0.848	30	27.54	8.20	9.67

Table 4: The percentage Width Reduction (WR) in each cycle normalized by the amount of plastic strain induced in each cycle.

When the beam area was very small (2nd cycle) there was no notable decrease in the sample width. For a given accelerating voltage and beam current (4th and 5th cycle), the normalized width reduction ($r = (\Delta w/w)/\varepsilon_p$) is significantly larger when the beam area is larger. This suggests that the extent of necking is more dependent on the beam area than intensity. Similar to stress relaxation, necking was also more pronounced at 120 kV.

For example, in the 3rd cycle (120 kV beam) r = 8.35, which is higher by a factor of 2.5 compared to the 4th cycle (200 kV beam, r = 3.28), even though the beam area was the same and beam intensity was only 1.7 times larger. Interestingly, when the e-beam was shifted to a new region for the 6th cycle (120 kV), a new neck appeared in that region and there was no further reduction in width of the previously necked region, which confirms that necking results from e-beam exposure. Furthermore, the specimen width decreased from 30 μm to 27.54 μm (8.2% reduction) in a single cycle.

Similar sample necking was seen in the Al-400 film as well (Fig. 41g) but the reduction in width was even more pronounced. The sample width reduced from 30 μm to 26.85 μm (10.5% reduction) after just one cycle of deformation at 120 kV, even though the imposed plastic strain was only 0.6% and the beam intensity was also quite low (Table 2). In the Au film no obvious necking was observed, presumably because the beam area was much smaller (Table 2).

Radiolysis, caused by the inelastic scattering of incident beam electrons, and knock-on displacement, due to elastic scattering of beam electrons, are the two main radiation damage mechanisms in TEM. However, in conducting materials such as metals, radiolysis is mostly suppressed because of the high density of delocalized electrons (R. F. Egerton, Li, and Malac 2004), which leaves knock-on displacement as the primary damage mechanism. Since knock-on displacement typically increases with accelerating voltage, a maximum voltage of 200 kV is used in most in situ TEM deformation experiments on metals to mitigate radiation damage. Nevertheless, recent studies have

shown that even low to moderate e-beam exposure in a TEM can affect the mechanical behavior of nanoscale materials such as nanoparticles and nanowires (Zheng et al. 2010b; Dai et al. 2012).

The experiments in this study demonstrate that the mechanical behavior of nanocrystalline and ultra-fine grained metals is also significantly affected by electron irradiation. In particular, the experiments reveal two unexpected trends as discussed below. First, beam-induced artifacts in nanostructured metals occur at beam energies far below the radiation damage (knock-on displacement) thresholds of these materials. Second, the beam-induced artifacts are more pronounced at lower accelerating voltages.

Knock-on displacement occurs when the beam energy exceeds a threshold, and may either result in the formation of vacancy-interstitial pairs in the bulk or lead to sputtering at the surfaces. However, the threshold energy for knock-on displacement in the bulk is usually larger than at the surface. For Al, the bulk displacement threshold energy exceeds 100 kV (Mingler and Karnthaler 2006) but the surface sputtering threshold energy is only 65 kV (R. F. Egerton et al. 2010). Since substantial stress relaxation is observed at 80 kV for the Al-225 sample (Figure 39a), it is conceivable that surface sputtering could be partly responsible for the observed relaxation. However, the experiments on the Al-400 film (Figure 39c) strongly suggest otherwise. If surface sputtering were a primary damage mechanism, the e-beam effect would be much smaller on the Al-400 film because of its higher thickness. In contrast, stress relaxation as well as

necking in the Al-400 film (at 120 kV) is much more pronounced compared to the Al-225 film.

The experiments on the Au film provide even stronger evidence that knock-on displacement is not responsible for the observed stress relaxation. The estimated surface sputtering threshold energy for Au is around 400 kV (R. F. Egerton et al. 2010) and the threshold for knock-on displacement in the bulk exceeds 1000 kV. Therefore, very little or no e-beam effect would be expected at 120 kV. Still, considerable stress relaxation (> 10%) is observed when the film is exposed to the 120 kV beam (Figure 39d and Table 2).

The experiments also reveal that the e-beam effects are more pronounced at 120 kV compared to 200 kV for all three films and the results are consistent across both cyclic loading as well as stress relaxation experiments (Figure 39, Table 2). For example, in the Al-400 film $\sigma_{0.75\%}$ decreased by 9% in the 2nd cycle compared to the 1st cycle (no beam) due to irradiation by 120 keV electrons, whereas $\sigma_{0.75\%}$ increased by ~40% when 200 keV electrons were used to image the sample in the 3rd cycle. Thus, there was a qualitative change in the stress-strain response when the accelerating voltage was changed, even though the beam areas were identical and beam intensities were comparable. The stress-strain behavior of the Au film (Figure 39d, Table 2) provides even more convincing evidence that the e-beam effect is higher at lower voltages since in this case the beam conditions (area, intensity and current) were identical. While $\sigma_{1\%}$ decreased by 11% between the 1st cycle (no beam) and 2nd cycle (120 kV beam), it was 5% higher in the 3rd cycle (200 kV beam) compared to the 1st cycle.

The trends in stress relaxation strongly indicate that knock-on displacement cannot explain the observations. This suggests that other processes are responsible for the changes in stress-strain behavior and sample geometry. It is well known that conduction electrons interact with lattice defects such as grain boundaries and dislocations and this leads to an increase in electrical resistivity (Bross and Haberlen 1993) compared to a perfect crystal. Furthermore, it has been shown that an electric current pulse of high density (10^4 A/cm^2) can assist dislocations in overcoming obstacles causing electroplasticity (Sprecher, Mannan, and Conrad 1986).

In the present case, the incident beam electrons play a role analogous to the electric current pulse. The beam electrons scatter inelastically near lattice defects and generate local lattice vibrations (phonons) either by scattering-induced phonon generation or via the excitation and damping of plasmons (Zhong-lin Wang 2013; R. F. Egerton 2013). The interaction of the phonons and dislocations leads to depinning of dislocations pinned at the grain boundaries. This phonon-assisted depinning increases dislocation mobility and consequently results in stress relaxation. For a given beam area, the number of inelastic scattering events increases with increasing beam intensity. Therefore, stress relaxation caused by phonon assisted depinning of dislocations increases with increasing beam intensity. Similarly, if the intensity is constant and the beam area increases, stress relaxation is again higher because dislocation activation is enhanced in a larger fraction of grains across the sample width.

Notably, this mechanism is consistent with the observation that when the beam is shifted to a new location there is increased dislocation activity in both the Al-225 film

(videoS3) and the Au film (videoS4). In this context, it is also worth noting that the cross-section of inelastic processes typically decreases with increasing beam energy (Williams and Carter 2009b). Therefore, the probability for phonon generation and dislocation activation would be higher at 120 kV compared to 200 kV, which can explain the higher e-beam effect at 120 kV. However, it is important to note that these phonons generated by inelastic scattering of beam electrons do not lead to a sustained increase in the overall sample temperature. Both Al and Au have high thermal conductivity (> 200 W/m/K) and even the largest beam currents used in our experiments are not expected to raise the sample temperature by more than 1 K (Williams and Carter 2009b). This remains the case even when we account for the lower thermal conductivity of nanocrystalline materials (Dong, Wen, and Melnik 2014).

If the stress relaxation is indeed due to the inelastic scattering of the e-beam near lattice defects and grain boundaries, by changing the grain boundary area in two films with identical thicknesses, it should be possible to detect a quantitative difference in the effect of the beam. Thus, to test this hypothesis, two Al films with identical thicknesses (400nm) but different mean grain sizes (400nm and 210nm) were synthesized (Figure 42).

This was achieved by depositing the films at different temperatures. The deposition of the film with d_m=400nm was carried out on HF etched (111) Si wafers at a temperature of 400^0C. On the other hand the film with d_m=210nm was deposited on (100) Si wafers having a native oxide layer at room temperature. Due to the different deposition

parameters, significantly different grains sizes were achieved in the two films. These films were then subjected to stress relaxation tests with identical beam intensities and sample areas exposed. After 10 minutes of exposure to the e-beam, the stress relaxation in the film with the smaller grain size was found to be 13% compared to only 4% percent stress relaxation in the film with the larger grain size. As the grain boundary area is greater in the film with the smaller grain size, these observations confirm that the e-beam induced relaxation in our experiments is caused by the inelastic scattering of the e-beam at grain boundaries and defects.

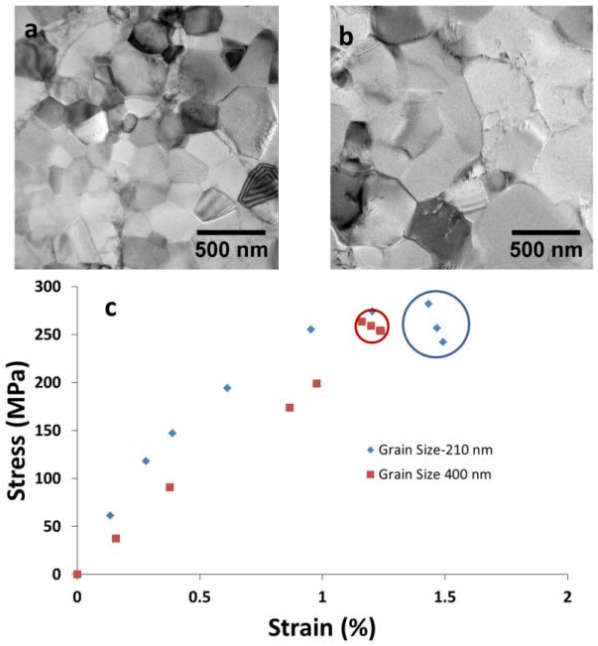

Figure 42: E-beam induced stress relaxation experiments on Al films with identical thickness but different grain sizes. (a) TEM bright field image of 400 nm thick Al film with a mean grain size (d_m) of 210nm. (b) TEM bright field image of 400 nm thick Al film with a mean grain size (d_m) of 400nm. (c) Stress relaxation data for the two films. The blue data points correspond to the film with d_m=210 nm and the red data points correspond the film with d_m=400 nm. The stress relaxation points in each experiment are encircled. For the same beam intensity and sample area exposed, the stress relaxation in the film with the lower grain size is 13% compared to only 4% in the film with the higher grain size.

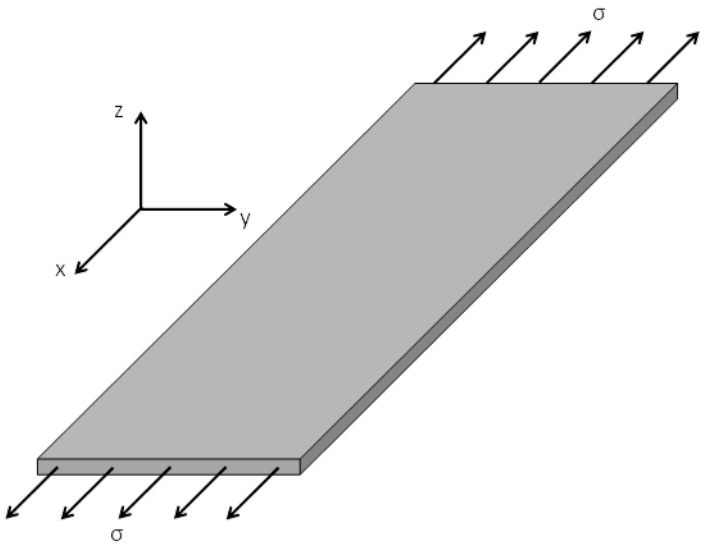

Figure 43: Schematic of the deformation of thin films in our experiments. When uniaxial stress is applied, the film has a tendency to decrease its thickness rather than width because of constraints from sample geometry. The free surfaces along the y-direction (width) are farther apart, which constrain the film from contracting laterally in the x-y plane. This leads to a plane stress-like condition in the x-y plane, with both σ_x and σ_y positive, and causes more reduction in thickness.

In addition to stress relaxation, the e-beam also caused considerable necking of the films (Fig. 41). This necking along the width is highly unusual because in thin film samples with a relatively large width, the thickness tends to decrease more during uniaxial loading due to geometrical constraints (Fig. 43). Similar to stress relaxation, the necking was also more pronounced at a lower accelerating voltage. But somewhat surprisingly the extent of necking was more sensitive to the beam area than beam intensity (compare 4^{th} and 5^{th} cycles or 3^{rd} and 6^{th} cycles of the Al-225 film). One possible explanation is that when the beam area is large, dislocation activation is increased in a higher fraction of grains across the sample width and these grains collectively deform to form a neck. When the beam area is small, plastic relaxation is enhanced in only a small fraction of grains across the sample. So even if the extent of relaxation in these grains is higher (because of higher beam intensity), their deformation

is constrained by the surrounding grains that undergo no relaxation. Thus, there is less macroscopic necking of the sample.

7.4 Conclusions

Overall, these results unambiguously show that the beam energy required to induce stress relaxation in nanostructured metals is substantially lower than their radiation damage threshold and that the relaxation is more pronounced at lower beam energies. It is important to note that these beam-induced artifacts are observed in two metals (Al and Au) that have highly dissimilar atomic weights and substantial differences in material properties (stacking fault energy, for example). The observations are also consistent across a range of sample thicknesses and grain sizes. This strongly suggests that e-beam exposure is likely to alter the deformation behavior in a broad spectrum of nanostructured metals, including commonly studied metals such as nickel and copper.

Furthermore, our results show that e-beam exposure causes anomalous changes in geometry when a larger cross-sectional area of the sample is exposed. Therefore, materials with sub micrometer dimensions (nanowires, nano pillars), which typically have their entire cross-section illuminated by the e-beam during in situ deformation experiments, are likely to be more susceptible to e-beam induced artifacts. Hence, caution needs to be exercised in interpreting the stress-strain response of such materials from in situ experiments.

While the observations clearly demonstrate the e-beam effect on the deformation response of nanocrystalline and ultrafine-grained metals, they also suggest a strategy to

minimize beam-induced artifacts during in situ testing. The results indicate that beam-assisted dislocation activation is far more important in these materials compared to radiolysis or knock-on damage. And since dislocation activation is reduced at higher beam energies, it may be prudent to employ higher accelerating voltages during in situ testing of nanostructured materials. However, it should be noted that the e-beam intensities used in this study are quite low (< 1.5 A/cm^2). When higher intensities (for high resolution imaging or spectroscopy applications) are employed, knock-on damage could become significant at higher accelerating voltages. Therefore, careful studies are required to establish appropriate imaging conditions to minimize beam-induced artifacts during in situ TEM deformation of nanocrystalline and ultrafine-grained metals.

.

CHAPTER 8

CONCLUSIONS

8.1 Summary of Research Findings

This dissertation has focused on synthesizing thin films with precisely controlled microstructures and using in situ TEM techniques to study their mechanical behavior. The major conclusions of the research are enlisted below.

- The microstructure of sputter deposited TiAl and TiNi thin films were tailored by using a seed layer mediated crystallization process. The technique used thin, crystalline Ti or Al seed layers to alter the crystallization behavior of amorphous intermetallic thin films. The seed layers aided crystallization and inhibited grain growth. Altering the in-plane seed spacing using a low temperature annealing heat treatment changed the final in-plane grain size. The spacing of the seed layers along the thickness of the films also altered the grain height. As a result, this technique was able to achieve control of the in-plane grain size as well as grain height. Consequently, it enabled the synthesis of films with gradient microstructures.

- The seed element used was found to have an effect on the phase constitution of the crystallized film. In NiTi, using a Cr seed instead of a Ti seed led to a stabilized austenite phase at room temperature and a nanocrystalline grain size. In situ TEM straining was subsequently used to study the stress induced phase

transformation in these films. Experiments revealed an extremely high transformation stress in these films. This was due to the small grain size of the films and plastic deformation in the austenite grains that accompanied the stress induced martensite transformation.

- Since the films with tailored microstructures were crystallized from an amorphous phase, a technique was developed to measure the local atomic level elastic strain and detect atomic scale rearrangements in metallic glass thin films. The technique measures geometric changes in selected area diffraction patterns to measure atomic level elastic strain tensors during in situ TEM straining. Atomic scale strain measurements revealed the presence of anelastic deformation in TiAl metallic glass. The anelastic deformation was found to be a result of atomic level structural rearrangements in the films caused by the applied stress.

- As in situ TEM straining was used to study the mechanical behavior of thin films, systematic experiments were carried out to determine the artifacts induced by the e-beam in the stress vs strain behavior of nc materials. Experiments revealed that the e-beam causes stress relaxation and anomalous necking in the samples during straining. These effects were more pronounced at lower accelerating voltages and were seen to occur in Al and Au films. It was revealed that the artifacts were caused by inelastic scattering events near grain boundaries and lattice defects in the films which resulted in enhanced dislocation activity. The findings suggest that at low e-beam intensities, artifacts are minimized at higher accelerating voltages.

8.2 Future Work

Although this dissertation has made contributions to the understanding of synthesis and mechanical behavior of thin films, there are many areas that still need to be explored. Firstly, the mechanical behavior of NiTi and TiAl films with gradient microstructures, which were synthesized using the seed mediated crystallization process, need to be investigated. It has been shown that a gradient structure can provide an optimal combination of strength and ductility in metallic materials. Thus, this aspect needs to be further studied. Moreover, the ability to stabilize different phases in NiTi thin films by using different seed elements also gives the capability to synthesize films with stabilized austenite and martensite phases at different regions along the thickness of the films. This could lead to a unique combination of properties from each of the phases, the martensite phase being more ductile while the smaller austenite grains having higher strength as well as the ability to undergo stress induced martensite transformation.

Additionally, there is scope for more research on the aspects of the stress induced transformations of the NiTi films with the stabilized austenitic phase. In situ TEM straining gives us the unique capability to use high resolution imaging and various diffraction techniques to study the dynamics of the transformation. Automated crystal orientation mapping (ACOM) in the TEM could help us uncover the crystallographic relationships between the martensitic variants that evolve during straining and the parent austenite phase. Having a deeper understanding of the transformation process would help us synthesize thin films with an optimal distribution of austenitic grain sizes.

Since having seed layers enhances crystallization in intermetallic thin films, the technique could also be used to synthesize amorphous-nanocrystalline composite films. Nanocrystalline materials exhibit excellent tensile strength while metallic glasses have an extended elastic limit. Thus combining these two classes of materials could also lead to novel and unique properties in these materials. Having synthesized amorphous-nanocrystalline composites, in situ TEM straining can be used to study the evolution of local atomic level elastic strains in the amorphous phase while also monitoring microstructural changes in the crystalline phase. Since amorphous metallic glasses fail by the propagation of shear bands, having intermittent crystalline layers or grains could help impede shear band growth.

In addition, there are other aspects of the deformation of metallic glasses that can be explored in further detail as well. The presence of free volume zones has been shown to influence anelastic deformation in these materials. It is also known that the fraction of free volume zones depends on the synthesis parameters of metallic glasses. By altering the argon pressure and gun power during sputter deposition, metallic glasses having different metastable energy landscapes can be synthesized. Tracking the atomic level strain evolution in films synthesized using different sputtering conditions could spread light on the influence of synthesis parameters on the mechanical behavior of metallic glasses. Finally, the mechanical and thermal history of metallic glasses has been known to cause structural rejuvenation in metallic glasses. Thus, using in situ straining combined with selected area diffraction we could investigate the difference in atomic scale behavior of metallic glasses that have been cycled thermally or mechanically.

REFERENCES

Abdolvand, Reza, and Farrokh Ayazi. 2008. “An Advanced Reactive Ion Etching Process for Very High Aspect-Ratio Sub-Micron Wide Trenches in Silicon.” *Sensors and Actuators A: Physical* 144 (1): 109–16. doi:10.1016/j.sna.2007.12.026.

Ames, Markus, Jürgen Markmann, Rudolf Karos, Andreas Michels, Andreas Tschöpe, and Rainer Birringer. 2008. “Unraveling the Nature of Room Temperature Grain Growth in Nanocrystalline Materials.” *Acta Materialia* 56 (16): 4255–66. doi:10.1016/j.actamat.2008.04.051.

Antonaglia, James, Wendelin J. Wright, Xiaojun Gu, Rachel R. Byer, Todd C. Hufnagel, Michael LeBlanc, Jonathan T. Uhl, and Karin A. Dahmen. 2014. “Bulk Metallic Glasses Deform via Slip Avalanches.” *Physical Review Letters* 112 (15): 155501. doi:10.1103/PhysRevLett.112.155501.

Argon, A. S., and L. T. Shi. 1982. “Analysis of Plastic Flow in an Amorphous Soap Bubble Raft by the Use of an Inter-Bubble Potential.” *Philosophical Magazine A* 46 (2): 275–94. doi:10.1080/01418618208239919.

Ashby, M. F., and A. L. Greer. 2006. “Metallic Glasses as Structural Materials.” *Scripta Materialia*, Viewpoint set no: 37. On mechanical behavior of metallic glasses Viewpoint set no: 37. On mechanical behavior of metallic glasses, 54 (3): 321–26. doi:10.1016/j.scriptamat.2005.09.051.

Béché, A., J. L. Rouvière, J. P. Barnes, and D. Cooper. 2011. “Dark Field Electron Holography for Strain Measurement.” *Ultramicroscopy* 111 (3): 227–38. doi:10.1016/j.ultramic.2010.11.030.

Béché, A., J. L. Rouvière, J. P. Barnes, and D. Cooper, 2013a. “Strain Measurement at the Nanoscale: Comparison between Convergent Beam Electron Diffraction, Nano-Beam Electron Diffraction, High Resolution Imaging and Dark Field Electron Holography.” *Ultramicroscopy* 131: 10–23.

Bernal, J. D. 1960. “Geometry of the Structure of Monatomic Liquids.” *Nature* 185 (January): 68–70. doi:10.1038/185068a0.

Bross, H., and O. Haberlen. 1993. “The Scattering of Electrons by Edge Dislocations in Al.” *Journal of Physics: Condensed Matter* 5 (41): 7687. doi:10.1088/0953-8984/5/41/016.

Bruck, H. A., T. Christman, A. J. Rosakis, and W. L. Johnson. 1994. “Quasi-Static Constitutive Behavior of $Zr_{41.25}Ti_{13.75}Ni_{10}Cu_{12.5}Be_{22.5}$ Bulk Amorphous Alloys.” http://inis.iaea.org/Search/search.aspx?orig_q=RN:25039053.

Bruck, H. A., A. J. Rosakis, and W. L. Johnson. 1996. “The Dynamic Compressive Behavior of Beryllium Bearing Bulk Metallic Glasses.” *Journal of Materials Research* 11 (02): 503–511. doi:10.1557/JMR.1996.0060.

Buijnsters, Josephus G., Jean-Pierre Celis, Ruud W. A. Hendrikx, and Luis Vázquez. 2013. “Metallic Seed Nanolayers for Enhanced Nucleation of Nanocrystalline Diamond Thin Films.” *The Journal of Physical Chemistry C* 117 (44): 23322–32. doi:10.1021/jp4071482.

Caron, A., R. Wunderlich, L. Gu, and H. -J. Fecht. 2011. “Structurally Enhanced Anelasticity in Zr-Based Bulk Metallic Glasses.” *Scripta Materialia* 64 (10): 946–49. doi:10.1016/j.scriptamat.2011.01.043.

Chang, C. M., C. H. Wang, J. H. Hsu, and J. C. Huang. 2014. “Al–Ni–Y–X (X = Cu, Ta, Zr) Metallic Glass Composite Thin Films for Broad-Band Uniform Reflectivity.” *Thin Solid Films* 571, Part 1 (November): 194–97. doi:10.1016/j.tsf.2014.10.048.

Chen, C. J., J. C. Huang, H. S. Chou, Y. H. Lai, L. W. Chang, X. H. Du, J. P. Chu, and T. G. Nieh. 2009. “On the Amorphous and Nanocrystalline Zr–Cu and Zr–Ti Co-Sputtered Thin Films.” *Journal of Alloys and Compounds*, 14th International Symposium on Metastable and Nano-Materials (ISMANAM-2007), 483 (1–2): 337–40. doi:10.1016/j.jallcom.2008.07.188.

Chen, H., Y. He, G. J. Shiflet, and S. J. Poon. 1994. “Deformation-Induced Nanocrystal Formation in Shear Bands of Amorphous Alloys.” *Nature* 367 (6463): 541–43. doi:10.1038/367541a0.

Chen, H. S., J. T. Krause, and E. Coleman. 1975. “Elastic Constants, Hardness and Their Implications to Flow Properties of Metallic Glasses.” *Journal of Non-Crystalline Solids* 18 (2): 157–71. doi:10.1016/0022-3093(75)90018-6.

Chu, Jinn P., J. S. C. Jang, J. C. Huang, H. S. Chou, Y. Yang, J. C. Ye, Y. C. Wang, et al. 2012. “Thin Film Metallic Glasses: Unique Properties and Potential Applications.” *Thin Solid Films* 520 (16): 5097–5122. doi:10.1016/j.tsf.2012.03.092.

Clément, L., R. Pantel, L. F. Tz Kwakman, and J. L. Rouvière. 2004. “Strain Measurements by Convergent-Beam Electron Diffraction: The Importance of Stress Relaxation in Lamella Preparations.” *Applied Physics Letters* 85 (4): 651–53. doi:10.1063/1.1774275.

Cohen, M. H., Turnbull, D. 1959. “Molecular Transport in Liquids and Glasses.” *The Journal of Chemical Physics* 31 (5): 1164–69. doi:10.1063/1.1730566.

Crozier, P. A., M. R. McCartney, and David J. Smith. 1990. “Observation of Exit Surface Sputtering in TiO2 Using Biased Secondary Electron Imaging.” *Surface Science* 237 (1–3): 232–40. doi:10.1016/0039-6028(90)90534-F.

Dai, Sheng, Jiong Zhao, Lin Xie, Yuan Cai, Ning Wang, and Jing Zhu. 2012. “Electron-Beam-Induced Elastic–Plastic Transition in Si Nanowires.” *Nano Letters* 12 (5): 2379–85. doi:10.1021/nl3003528.

Ding, J., Y. Q. Cheng, and E. Ma. 2012. “Correlating Local Structure with Inhomogeneous Elastic Deformation in a Metallic Glass.” *Applied Physics Letters* 101 (12): 121917. doi:10.1063/1.4754121.

Dmowski, W., T. Iwashita, C.-P. Chuang, J. Almer, and T. Egami. 2010. “Elastic Heterogeneity in Metallic Glasses.” *Physical Review Letters* 105 (20): 205502. doi:10.1103/PhysRevLett.105.205502.

Dong, Huicong, Bin Wen, and Roderick Melnik. 2014. “Relative Importance of Grain Boundaries and Size Effects in Thermal Conductivity of Nanocrystalline Materials.” *Scientific Reports* 4 (November). doi:10.1038/srep07037.

Drera, Giovanni, Alessio Giampietri, Ivano Alessandri, Elena Magnano, Federica Bondino, and Silvia Nappini. 2015. “Grain Size and Stoichiometry Control over RF-Sputtered Multiferroic BiFeO3 Thin Films on Silicon Substrates.” *Thin Solid Films* 589 (August): 551–55. doi:10.1016/j.tsf.2015.06.030.

Ebner, Christian, Rohit Sarkar, Jagannathan Rajagopalan, and Christian Rentenberger. 2016. “Local, Atomic--level Elastic Strain Measurements of Metallic Glass Thin Films by Electron Diffracion.” *Ultramicroscopy* In Review.

Edalati, Kaveh, Shoichi Toh, Hideaki Iwaoka, Masashi Watanabe, Zenji Horita, Daisuke Kashioka, Kyosuke Kishida, and Haruyuki Inui. 2012. “Ultrahigh Strength and High Plasticity in TiAl Intermetallics with Bimodal Grain Structure and Nanotwins.” *Scripta Materialia* 67 (10): 814–17. doi:10.1016/j.scriptamat.2012.07.030.

Egerton, R. F. 2013. “Control of Radiation Damage in the TEM.” *Ultramicroscopy*, Frontiers of Electron Microscopy in Materials Science, 127 (April): 100–108. doi:10.1016/j.ultramic.2012.07.006.

Egerton, R. F., P. Li, and M. Malac. 2004. “Radiation Damage in the TEM and SEM.” *Micron*, International Wuhan Symposium on Advanced Electron Microscopy, 35 (6): 399–409. doi:10.1016/j.micron.2004.02.003.

Egerton, R. F., R. McLeod, F. Wang, and M. Malac. 2010. “Basic Questions Related to Electron-Induced Sputtering in the TEM.” *Ultramicroscopy*, PROCEEDINGS OF THE INTERNATIONAL WORKSHOP ON ENHANCED DATA GENERATED BY ELECTRONS, 110 (8): 991–97. doi:10.1016/j.ultramic.2009.11.003.

Egerton, Raymond F., Feng Wang, and Peter A. Crozier. 2006. “Beam-Induced Damage to Thin Specimens in an Intense Electron Probe.” *Microscopy and Microanalysis* 12 (01): 65–71. doi:10.1017/S1431927606060065.

El Khakani, M.a., M. Chaker, A. Jean, S. Boily, J.c. Kieffer, M.e. O’Hern, M.f. Ravet, and F. Rousseaux. 1994. “Hardness and Young’s Modulus of Amorphous a-SiC Thin Films Determined by Nanoindentation and Bulge Tests.” *Journal of Materials Research* 9 (01): 96–103. doi:10.1557/JMR.1994.0096.

Fang, T. H., W. L. Li, N. R. Tao, and K. Lu. 2011. “Revealing Extraordinary Intrinsic Tensile Plasticity in Gradient Nano-Grained Copper.” *Science* 331 (6024): 1587–90. doi:10.1126/science.1200177.

Floro, Jerrold A., Eric Chason, Robert C. Cammarata, and David J. Srolovitz. 2002. “Physical Origins of Intrinsic Stresses in Volmer–Weber Thin Films.” *MRS Bulletin* 27 (01): 19–25. doi:10.1557/mrs2002.15.

Fu, Yongqing, Hejun Du, Weimin Huang, Sam Zhang, and Min Hu. 2004. “TiNi-Based Thin Films in MEMS Applications: A Review.” *Sensors and Actuators A: Physical* 112 (2–3): 395–408. doi:10.1016/j.sna.2004.02.019.

Fu, Yongqing, Weimin Huang, Hejun Du, Xu Huang, Junping Tan, and Xiangyang Gao. 2001. “Characterization of TiNi Shape-Memory Alloy Thin Films for MEMS Applications.” *Surface and Coatings Technology* 145 (1–3): 107–12. doi:10.1016/S0257-8972(01)01324-X.

Girault, B., D. Eyidi, P. Goudeau, T. Sauvage, P. Guerin, E. Le Bourhis, and P.-O. Renault. 2013. “Controlled Nanostructuration of Polycrystalline Tungsten Thin Films.” *Journal of Applied Physics* 113 (17): 174310. doi:10.1063/1.4803699.

Greene, Lori E., Matt Law, Dawud H. Tan, Max Montano, Josh Goldberger, Gabor Somorjai, and Peidong Yang. 2005. “General Route to Vertical ZnO Nanowire Arrays Using Textured ZnO Seeds.” *Nano Letters* 5 (7): 1231–36. doi:10.1021/nl050788p.

Guo, H., P. F. Yan, Y. B. Wang, J. Tan, Z. F. Zhang, M. L. Sui, and E. Ma. 2007. “Tensile Ductility and Necking of Metallic Glass.” *Nature Materials* 6 (10): 735–39. doi:10.1038/nmat1984.

Han, Jong H., and M. Taher A. Saif. 2006. “In Situ Microtensile Stage for Electromechanical Characterization of Nanoscale Freestanding Films.” *Review of Scientific Instruments* 77 (4): 045102. doi:10.1063/1.2188368.

Haque, M. A., and M. T. A. Saif. 2002. “In-Situ Tensile Testing of Nano-Scale Specimens in SEM and TEM.” *Experimental Mechanics* 42 (1): 123–28. doi:10.1007/BF02411059.

Harp, G. R., and S. S. P. Parkin. 1994. “Seeded Epitaxy of Metals by Sputter Deposition.” *Applied Physics Letters* 65 (24): 3063–65. doi:10.1063/1.112507.

Hays, C. C., C. P. Kim, and W. L. Johnson. 2000. “Microstructure Controlled Shear Band Pattern Formation and Enhanced Plasticity of Bulk Metallic Glasses Containing in Situ Formed Ductile Phase Dendrite Dispersions.” *Physical Review Letters* 84 (13): 2901–4. doi:10.1103/PhysRevLett.84.2901.

He, Y., R.b. Schwarz, A. Migliori, and S.h. Whang. 1995. “Elastic Constants of Single Crystal γ – TiAl.” *Journal of Materials Research* 10 (05): 1187–1195. doi:10.1557/JMR.1995.1187.

Hosoda, H., S. Hanada, K. Inoue, T. Fukui, Y. Mishima, and T. Suzuki. 1998. “Martensite Transformation Temperatures and Mechanical Properties of Ternary NiTi Alloys with Offstoichiometric Compositions.” *Intermetallics* 6 (4): 291–301. doi:10.1016/S0966-9795(97)00100-3.

Huang, Xiangyang, Graeme J. Ackland, and Karin M. Rabe. 2003. “Crystal Structures and Shape-Memory Behaviour of NiTi.” *Nature Materials* 2 (5): 307–11. doi:10.1038/nmat884.

Huang, Yongjiang, J. C. Khong, Thomas Connolley, and J. Mi. 2014. “The Onset of Plasticity of a Zr-Based Bulk Metallic Glass.” *International Journal of Plasticity* 60 (September): 87–100. doi:10.1016/j.ijplas.2014.05.003.

Hüe, Florian, Martin Hÿtch, Hugo Bender, Florent Houdellier, and Alain Claverie. 2008. “Direct Mapping of Strain in a Strained Silicon Transistor by High-Resolution Electron Microscopy.” *Physical Review Letters* 100 (15): 156602. doi:10.1103/PhysRevLett.100.156602.

Hufnagel, T. C., R. T. Ott, and J. Almer. 2006. “Structural Aspects of Elastic Deformation of a Metallic Glass.” *Physical Review B* 73 (6): 064204. doi:10.1103/PhysRevB.73.064204.

Hufnagel, Todd C., Christopher A. Schuh, and Michael L. Falk. 2016. “Deformation of Metallic Glasses: Recent Developments in Theory, Simulations, and Experiments.” *Acta Materialia* 109 (May): 375–93. doi:10.1016/j.actamat.2016.01.049.

Hufnagel, Todd C., Uday K. Vempati, and Jonathan D. Almer. 2013. “Crack-Tip Strain Field Mapping and the Toughness of Metallic Glasses.” *PLoS ONE* 8 (12): e83289. doi:10.1371/journal.pone.0083289.

Izadi, Ehsan, and Jagannathan Rajagopalan. 2016. “Texture Dependent Strain Rate Sensitivity of Ultrafine-Grained Aluminum Films.” *Scripta Materialia* 114 (March): 65–69. doi:10.1016/j.scriptamat.2015.12.003.

J. J. Lewandowski, W. H. Wang, and A. L. Greer. 2005. “Intrinsic Plasticity or Brittleness of Metallic Glasses.” *Philosophical Magazine Letters* 85 (2): 77–87. doi:10.1080/09500830500080474.

Jang, Dongchan, and Julia R. Greer. 2010. “Transition from a Strong-yet-Brittle to a Stronger-and-Ductile State by Size Reduction of Metallic Glasses.” *Nature Materials* 9 (3): 215–19. doi:10.1038/nmat2622.

Kacher, Josh, I. M. Robertson, Matt Nowell, J. Knapp, and Khalid Hattar. 2011. “Study of Rapid Grain Boundary Migration in a Nanocrystalline Ni Thin Film.” *Materials Science and Engineering: A* 528 (3): 1628–35. doi:10.1016/j.msea.2010.10.109.

Klement, W., R. H. Willens, and Pol Duwez. 1960. “Non-Crystalline Structure in Solidified Gold–Silicon Alloys.” *Nature* 187 (4740): 869–70. doi:10.1038/187869b0.

Koch, C. C. 2013. "Top-Down Synthesis Of Nanostructured Materials: Mechanical And Thermal Processing Methods." *Reviews on Advanced Materials Science* 5, no. 2 (2003): 91-99.

Kou, Hongning, Jian Lu, and Ying Li. 2014. “High-Strength and High-Ductility Nanostructured and Amorphous Metallic Materials.” *Advanced Materials* 26 (31): 5518–24. doi:10.1002/adma.201401595.

Kumar, K. S., S. Suresh, M. F. Chisholm, J. A. Horton, and P. Wang. 2003. “Deformation of Electrodeposited Nanocrystalline Nickel.” *Acta Materialia* 51 (2): 387–405. doi:10.1016/S1359-6454(02)00421-4.

Kumar, K. S, H Van Swygenhoven, and S Suresh. 2003. “Mechanical Behavior of Nanocrystalline Metals and alloys1.” *Acta Materialia*, The Golden Jubilee Issue. Selected topics in Materials Science and Engineering: Past, Present and Future, 51 (19): 5743–74. doi:10.1016/j.actamat.2003.08.032.

Kwok, Chi Kong, and Seshu B. Desu. 1993. “Low Temperature Perovskite Formation of Lead Zirconate Titanate Thin Films by a Seeding Process.” *Journal of Materials Research* 8 (02): 339–344. doi:10.1557/JMR.1993.0339.

Lee, Dongwoo, Bingge Zhao, Eric Perim, Haitao Zhang, Pan Gong, Yulai Gao, Yanhui Liu, et al. 2016. “Crystallization Behavior upon Heating and Cooling in Cu50Zr50 Metallic Glass Thin Films.” *Acta Materialia* 121 (December): 68–77. doi:10.1016/j.actamat.2016.08.076.

Löffler, Jörg F. 2003. “Bulk Metallic Glasses.” *Intermetallics* 11 (6): 529–40. doi:10.1016/S0966-9795(03)00046-3.

Lu, L., M. L. Sui, and K. Lu. 2000. “Superplastic Extensibility of Nanocrystalline Copper at Room Temperature.” *Science* 287 (5457): 1463–66. doi:10.1126/science.287.5457.1463.

Ma, D., A. D. Stoica, X.-L. Wang, Z. P. Lu, B. Clausen, and D. W. Brown. 2012. “Elastic Moduli Inheritance and the Weakest Link in Bulk Metallic Glasses.” *Physical Review Letters* 108 (8): 085501. doi:10.1103/PhysRevLett.108.085501.

Mahr, Christoph, Knut Müller-Caspary, Tim Grieb, Marco Schowalter, Thorsten Mehrtens, Florian F. Krause, Dennis Zillmann, and Andreas Rosenauer. 2015. “Theoretical Study of Precision and Accuracy of Strain Analysis by Nano-Beam Electron Diffraction.” *Ultramicroscopy* 158 (November): 38–48. doi:10.1016/j.ultramic.2015.06.011.

Masui, K, S Maruno, S Sakakibara, and T Kawaguchi. 1985. “Formation of Amorphous Al-Transition Metal (TM: Fe, Co, Ni) Binary Alloy Films by RF-Sputtering.” *Journal of Non-Crystalline Solids* 74 (2): 271–84. doi:10.1016/0022-3093(85)90074-2.

Masumura, R. A., P. M. Hazzledine, and C. S. Pande. 1998. “Yield Stress of Fine Grained Materials.” *Acta Materialia* 46 (13): 4527–34. doi:10.1016/S1359-6454(98)00150-5.

Mattern, N., J. Bednarčik, S. Pauly, G. Wang, J. Das, and J. Eckert. 2009. “Structural Evolution of Cu–Zr Metallic Glasses under Tension.” *Acta Materialia* 57 (14): 4133–39. doi:10.1016/j.actamat.2009.05.011.

Meyers, M. A., A. Mishra, and D. J. Benson. 2006. “Mechanical Properties of Nanocrystalline Materials.” *Progress in Materials Science* 51 (4): 427–556. doi:10.1016/j.pmatsci.2005.08.003.

Miller, K.t., and F.f. Lange. 1991. “Highly Oriented Thin Films of Cubic Zirconia on Sapphire through Grain Growth Seeding.” *Journal of Materials Research* 6 (11): 2387–2392. doi:10.1557/JMR.1991.2387.

Mingler, Bernhard, and H. Peter Karnthaler. 2006. “Radiation Damage during HRTEM Studies in Pure Al and Al Alloys.” *International Journal of Materials Research* 97 (7): 1041–45. doi:10.3139/146.101336.

Miracle, Daniel B. 2004. “A Structural Model for Metallic Glasses.” *Nature Materials* 3 (10): 697–702. doi:10.1038/nmat1219.

Moffat, T. P. 1994. “Electrodeposition of Al-Cr Metallic Glass.” *Journal of The Electrochemical Society* 141 (9): L115–17. doi:10.1149/1.2055172.

Nagendra, N, U Ramamurty, T. T Goh, and Y Li. 2000. “Effect of Crystallinity on the Impact Toughness of a La-Based Bulk Metallic Glass.” *Acta Materialia* 48 (10): 2603–15. doi:10.1016/S1359-6454(00)00052-5.

Otsuka, K., and X. Ren. 2005. “Physical Metallurgy of Ti–Ni-Based Shape Memory Alloys.” *Progress in Materials Science* 50 (5): 511–678. doi:10.1016/j.pmatsci.2004.10.001.

Pekarskaya, E., C. P. Kim, and W. L. Johnson. 2001. “In Situ Transmission Electron Microscopy Studies of Shear Bands in a Bulk Metallic Glass Based Composite.” *Journal of Materials Research* 16 (09): 2513–2518. doi:10.1557/JMR.2001.0344.

Petrov, I., P. B. Barna, L. Hultman, and J. E. Greene. 2003. “Microstructural Evolution during Film Growth.” *Journal of Vacuum Science & Technology A* 21 (5): S117–28. doi:10.1116/1.1601610.

Poulsen, Henning F., John A. Wert, Jörg Neuefeind, Veijo Honkimäki, and Mark Daymond. 2005. “Measuring Strain Distributions in Amorphous Materials.” *Nature Materials* 4 (1): 33–36. doi:10.1038/nmat1266.

Rajagopalan, Jagannathan, Jong H. Han, and M. Taher A. Saif. 2007. “Plastic Deformation Recovery in Freestanding Nanocrystalline Aluminum and Gold Thin Films.” *Science* 315 (5820): 1831–34. doi:10.1126/science.1137580.

Rincón, C, J Romero, J Esteve, E Martínez, and A Lousa. 2003. “Effects of Carbon Incorporation in Tungsten Carbide Films Deposited by R.f. Magnetron Sputtering: Single Layers and Multilayers.” *Surface and Coatings Technology*, Proceedings of the 29th International conference on Metallurgical Coatings and Thin Films, 163–164 (January): 386–91. doi:10.1016/S0257-8972(02)00635-7.

Sanders, P. G., J. A. Eastman, and J. R. Weertman. 1997. “Elastic and Tensile Behavior of Nanocrystalline Copper and Palladium.” *Acta Materialia* 45 (10): 4019–25. doi:10.1016/S1359-6454(97)00092-X.

Sarkar, Rohit, Christian Rentenberger, and Jagannathan Rajagopalan. 2015. “Electron Beam Induced Artifacts During in Situ TEM Deformation of Nanostructured Metals.” *Scientific Reports* 5 (November). doi:10.1038/srep16345.

Schleip, E, D. M Herlach, and B Feuerbacher. 1990. “External Seeding of a Metastable Metallic Phase.” *Europhysics Letters (EPL)* 11 (8): 751–55. doi:10.1209/0295-5075/11/8/010.

Schuh, Christopher A., Todd C. Hufnagel, and Upadrasta Ramamurty. 2007. “Mechanical Behavior of Amorphous Alloys.” *Acta Materialia* 55 (12): 4067–4109. doi:10.1016/j.actamat.2007.01.052.

Scudino, S., H. Shakur Shahabi, M. Stoica, I. Kaban, B. Escher, U. Kühn, G. B. M. Vaughan, and J. Eckert. 2015. “Structural Features of Plastic Deformation in Bulk Metallic Glasses.” *Applied Physics Letters* 106 (3): 031903.doi:10.1063/1.4906305.

Sprecher, A. F., S. L. Mannan, and H. Conrad. 1986. “Overview No. 49: On the Mechanisms for the Electroplastic Effect in Metals.” *Acta Metallurgica* 34 (7): 1145–62. doi:10.1016/0001-6160(86)90001-5.

Stoner, B. R., G.-H. M. Ma, S. D. Wolter, and J. T. Glass. 1992. “Characterization of Bias-Enhanced Nucleation of Diamond on Silicon by \textit{invacuo} Surface Analysis and Transmission Electron Microscopy.” *Physical Review B* 45 (19): 11067–84. doi:10.1103/PhysRevB.45.11067.

Szlufarska, Izabela, Aiichiro Nakano, and Priya Vashishta. 2005. “A Crossover in the Mechanical Response of Nanocrystalline Ceramics.” *Science* 309 (5736): 911–14. doi:10.1126/science.1114411.

Telford, Mark. 2004. “The Case for Bulk Metallic Glass.” *Materials Today* 7 (3): 36–43. doi:10.1016/S1369-7021(04)00124-5.

Thompson, C. V. 2000. “Structure Evolution During Processing of Polycrystalline Films.” *Annual Review of Materials Science* 30 (1): 159–90. doi:10.1146/annurev.matsci.30.1.159.

Tian, Lin, Xiao-Lei Wang, and Zhi-Wei Shan. 2016. “Mechanical Behavior of Micronanoscaled Metallic Glasses.” *Materials Research Letters* 4 (2): 63–74. doi:10.1080/21663831.2015.1124298.

Tong, Y., T. Iwashita, W. Dmowski, H. Bei, Y. Yokoyama, and T. Egami. 2015. “Structural Rejuvenation in Bulk Metallic Glasses.” *Acta Materialia* 86 (March): 240–46. doi:10.1016/j.actamat.2014.12.020.

Trelewicz, Jason R., and Christopher A. Schuh. 2007. “The Hall–Petch Breakdown in Nanocrystalline Metals: A Crossover to Glass-like Deformation.” *Acta Materialia* 55 (17): 5948–58. doi:10.1016/j.actamat.2007.07.020.

Troeger, L. P., and E. A. Starke Jr. 2000. “Particle-Stimulated Nucleation of Recrystallization for Grain-Size Control and Superplasticity in an Al–Mg–Si–Cu Alloy.” *Materials Science and Engineering: A* 293 (1–2): 19–29. doi:10.1016/S0921-5093(00)01235-1.

Usuda, Koji, Toshinori Numata, Toshifumi Irisawa, Norio Hirashita, and Shinichi Takagi. 2005. “Strain Characterization in SOI and Strained-Si on SGOI MOSFET Channel Using Nano-Beam Electron Diffraction (NBD).” *Materials Science and Engineering: B*, EMRS 2005, Symposium DMaterials Science and Device Issues

for Future Technologies, 124–125 (December): 143–47. doi:10.1016/j.mseb.2005.08.062.

Valiev, Ruslan Z., Yuri Estrin, Zenji Horita, Terence G. Langdon, Michael J. Zechetbauer, and Yuntian T. Zhu. 2006. “Producing Bulk Ultrafine-Grained Materials by Severe Plastic Deformation.” *JOM* 58 (4): 33–39. doi:10.1007/s11837-006-0213-7.

Van Swygenhoven, H., D. Farkas, and A. Caro. 2000. “Grain-Boundary Structures in Polycrystalline Metals at the Nanoscale.” *Physical Review B* 62 (2): 831–38. doi:10.1103/PhysRevB.62.831.

Vempati, U. K., P. K. Valavala, M. L. Falk, J. Almer, and T. C. Hufnagel. 2012. “Length-Scale Dependence of Elastic Strain from Scattering Measurements in Metallic Glasses.” *Physical Review B* 85 (21): 214201. doi:10.1103/PhysRevB.85.214201.

Venables, J. A., G. D. T. Spiller, and M. Hanbucken. 1984. “Nucleation and Growth of Thin Films.” *Reports on Progress in Physics* 47 (4): 399. doi:10.1088/0034-4885/47/4/002.

Vitos, L., A. V. Ruban, H. L. Skriver, and J. Kollár. 1998. “The Surface Energy of Metals.” *Surface Science* 411 (1–2): 186–202. doi:10.1016/S0039-6028(98)00363-X.

Volkert, C. A., A. Donohue, and F Spaepen. 2008. “Effect of Sample Size on Deformation in Amorphous Metals.” *Journal of Applied Physics* 103 (8): 083539. doi:10.1063/1.2884584.

Vopsaroiu, M., M.J. Thwaites, S. Rand, P.J. Grundy, and K. O’Grady. 2004. “Novel Sputtering Technology for Grain-Size Control.” *IEEE Transactions on Magnetics* 40 (4): 2443–45. doi:10.1109/TMAG.2004.828971.

Waitz, T., T. Antretter, F. D. Fischer, N. K. Simha, and H. P. Karnthaler. 2007. “Size Effects on the Martensitic Phase Transformation of NiTi Nanograins.” *Journal of the Mechanics and Physics of Solids* 55 (2): 419–44. doi:10.1016/j.jmps.2006.06.006.

Waitz, T., V. Kazykhanov, and H.P. Karnthaler. 2004. “Martensitic Phase Transformations in Nanocrystalline NiTi Studied by TEM.” *Acta Materialia* 52 (1): 137–47. doi:10.1016/j.actamat.2003.08.036.

Wang, C. -C., J. Ding, Y. -Q. Cheng, J. -C. Wan, L. Tian, J. Sun, Z. -W. Shan, Ju Li, and E. Ma. 2012. “Sample Size Matters for Al88Fe7Gd5 Metallic Glass: Smaller Is Stronger.” *Acta Materialia* 60 (13–14): 5370–79. doi:10.1016/j.actamat.2012.06.019.

Wang, W. H., C. Dong, and C. H. Shek. 2004. “Bulk Metallic Glasses.” *Materials Science and Engineering: R: Reports* 44 (2–3): 45–89. doi:10.1016/j.mser.2004.03.001.

Wang, X. D., J. Bednarcik, K. Saksl, H. Franz, Q. P. Cao, and J. Z. Jiang. 2007. “Tensile Behavior of Bulk Metallic Glasses by in Situ X-Ray Diffraction.” *Applied Physics Letters* 91 (8): 081913. doi:10.1063/1.2773945.

Wang, Z. T., J. Pan, Y. Li, and C. A. Schuh. 2013. “Densification and Strain Hardening of a Metallic Glass under Tension at Room Temperature.” *Physical Review Letters* 111 (13): 135504. doi:10.1103/PhysRevLett.111.135504.

Wang, Z., P. Wen, L. S. Huo, H. Y. Bai, and W. H. Wang. 2012. “Signature of Viscous Flow Units in Apparent Elastic Regime of Metallic Glasses.” *Applied Physics Letters* 101 (12): 121906. doi:10.1063/1.4753813.

Wang, Zhong-lin. 2013. *Elastic and Inelastic Scattering in Electron Diffraction and Imaging*. Springer Science & Business Media.

Westbrook, J. H. n.d. *Intermetallic Compounds. Structural Applications of Intermetallic Compounds*. Wiley.

Williams, David B., and C. Barry Carter. 2009a. “The Transmission Electron Microscope.” In *Transmission Electron Microscopy*, 3–22. Springer US. http://link.springer.com/chapter/10.1007/978-0-387-76501-3_1.

Wu, B. Y. C., C. A. Schuh, and P. J. Ferreira. n.d. “Nanostructured Ni-Co Alloys with Tailorable Grain Size and Twin Density.” *Metallurgical and Materials Transactions A* 36 (7): 1927–36. doi:10.1007/s11661-005-0056-9.

Wu, XiaoLei, Ping Jiang, Liu Chen, Fuping Yuan, and Yuntian T. Zhu. 2014. “Extraordinary Strain Hardening by Gradient Structure.” *Proceedings of the National Academy of Sciences* 111 (20): 7197–7201. doi:10.1073/pnas.1324069111.

Xu, Lifen, Yi Guo, Qing Liao, Jianping Zhang, and Dongsheng Xu. 2005. “Morphological Control of ZnO Nanostructures by Electrodeposition.” *The Journal of Physical Chemistry B* 109 (28): 13519–22. doi:10.1021/jp051007b.

Yang, L., N. R. Tao, K. Lu, and L. Lu. 2013. “Enhanced Fatigue Resistance of Cu with a Gradient Nanograined Surface Layer.” *Scripta Materialia* 68 (10): 801–4. doi:10.1016/j.scriptamat.2013.01.031.

Ye, J. C., J. Lu, C. T. Liu, Q. Wang, and Y. Yang. 2010. “Atomistic Free-Volume Zones and Inelastic Deformation of Metallic Glasses.” *Nature Materials* 9 (8): 619–23. doi:10.1038/nmat2802.

Ye, Jia, Raja K. Mishra, Alan R. Pelton, and Andrew M. Minor. 2010. “Direct Observation of the NiTi Martensitic Phase Transformation in Nanoscale Volumes.” *Acta Materialia* 58 (2): 490–98. doi:10.1016/j.actamat.2009.09.027.

Yong, Ken-Tye, Yudhisthira Sahoo, Kaushik Roy Choudhury, Mark T. Swihart, John R. Minter, and Paras N. Prasad. 2006. “Shape Control of PbSe Nanocrystals Using Noble Metal Seed Particles.” *Nano Letters* 6 (4): 709–14. doi:10.1021/nl052472n.

Zheng, Kun, Chengcai Wang, Yong-Qiang Cheng, Yonghai Yue, Xiaodong Han, Ze Zhang, Zhiwei Shan, et al. 2010a. “Electron-Beam-Assisted Superplastic Shaping of Nanoscale Amorphous Silica.” *Nature Communications* 1 (June): 24. doi:10.1038/ncomms1021.

Zhong, C., H. Zhang, Q. P. Cao, X. D. Wang, D. X. Zhang, U. Ramamurty, and J. Z. Jiang. 2016. “On the Critical Thickness for Non-Localized to Localized Plastic Flow Transition in Metallic Glasses: A Molecular Dynamics Study.” *Scripta Materialia* 114 (March): 93–97. doi:10.1016/j.scriptamat.2015.12.012.

Zhu, X., R. Birringer, U. Herr, and H. Gleiter. 1987. “X-Ray Diffraction Studies of the Structure of Nanometer-Sized Crystalline Materials.” *Physical Review B* 35 (17): 9085–90. doi:10.1103/PhysRevB.35.9085.

APPENDIX A

SUPPLEMENTARY VIDEOS SHOWING EFFECT OF E-BEAM

Consult Attached Files

Supplementary video S1 was taken during the cyclic straining of the Al 225 film. This video was taken during loading in the 3rd cycle. Dislocation activity can be observed in this video. Supplementary video S2 was also taken during the cyclic straining of the Al 225 film. This video was taken during un-loading in the 6rd cycle. Even during unloading dislocation activity can be observed. Supplementary video S3 was taken during the stress relaxation test of the Al 225 film. In this video increased dislocation activity can be observed when the electron beam is move to a region of the sample that was previously unexposed.